Title
Advancing targeting radiopharmaceuticals for theranostic applications

Author
Bailey, Tyler Allan

Publication Date
2022

Peer reviewed|Thesis/dissertation

Advancing targeting radiopharmaceuticals for theranostic applications

By

Tyler Allan Bailey

A dissertation submitted in partial satisfaction of the

requirements for the degree of

Doctor of Philosophy

in

Engineering – Nuclear Engineering

in the

Graduate Division

of the

University of California, Berkeley

Committee in charge:

Professor Rebecca J. Abergel, Chair

Professor Moriel Vandsburger

Professor Lee Bernstein

Professor Kai Vetter

Spring 2022

Advancing targeting radiopharmaceuticals for theranostic applications

Abstract

Advancing targeting radiopharmaceuticals for theranostic applications

by

Tyler Allan Bailey

Doctor of Philosophy in Engineering - Nuclear Engineering

University of California, Berkeley

Professor Rebecca J. Abergel, Chair

In the past few decades, targeted radionuclide therapy has emerged as a potential strategy for combatting cancer. Through the delivery of alpha, beta-minus, or Auger electron emitting radionuclides to diseased tissue via targeting vectors, targeting radiopharmaceuticals can deal cytotoxic damage to cancerous cells while minimizing damage to healthy tissue. Furthermore, applying the theranostic approach, where a diagnostic radionuclide is delivered using the same targeting vector, allows targeted radionuclide therapy to become more personalized, potentially making these treatments more effective. This strategy allows for using the same targeting radiopharmaceutical for both diagnostics and therapy. This enables patient-specific dosimetry, the ability to predict the response for a given therapy, improved treatment planning, and monitoring of the ongoing treatment. Unfortunately, widespread use of the theranostic approach faces a variety of challenges in order to make theranostics more obtainable.

This dissertation seeks to advance targeting radiopharmaceuticals for theranostic applications by investigating a novel companion diagnostic radionuclide, ^{134}Ce, as a companion diagnostic for both ^{225}Ac and ^{227}Th. In addition, the use of the chelator 3,4,3-LI(1,2-HOPO) (HOPO) was investigated with ^{134}Ce, the ^{90}Y/^{86}Y theranostic pair, and ^{225}Ac. HOPO has the potential to be a “theranostic chelator” due to its affinity for a variety of strategic trivalent and tetravalent radiometals. Furthermore, a novel elution strategy for ^{224}Ra/^{212}Pb generators was benchmarked which could facilitate the use of the ^{212}Pb/^{203} Pb theranostics in clinical settings. Lastly, the use of Siderocalin fusion proteins, which could pave the doorway for the development of antibody-based “cold-kits” thereby allowing for the rapid, room temperature labeling of monoclonal antibodies for targeted radionuclide therapy, was explored.

The actinide radionuclides ^{225}Ac and ^{227}Th have recently shown great clinical and preclinical success for targeted radionuclide therapy due to their long decay chain which emits 4 or 5 α particles and their lack of a long-lived decay product. Unfortunately, neither of these radionuclides can be suitably imaged by contemporary molecular imaging modalities including positron emission tomography (PET) or single photon emission computed tomography (SPECT). Furthermore, there is not an actinium or thorium isotope that allows for PET or SPECT imaging. To address this need a surrogate diagnostic radionuclide with chemically similar properties using the *in vivo* generator system ^{134}Ce/^{134}La was investigated since it can be imaged by PET and has an unique redox chemistry that allows ^{134}Ce to be stabilized as $^{134}Ce^{III}$ to mimic $^{225}Ac^{III}$ or as $^{134}Ce^{IV}$ to mimic $^{227}Th^{IV}$. The surrogacy of ^{134}Ce/^{134}La is investigated by assaying

the biodistribution and *in vivo* stability of ^{134}Ce complexes ($^{134}Ce^{III}$-DTPA, $^{134}Ce^{III}$-DOTA, and $^{134}Ce^{IV}$-HOPO) through microPET imaging of a murine model. All of these complexes displayed high *in vivo* stability and rapid pharmacokinetics, and they all had negligible residual activity 24 hours after administration. Furthermore, the long half-life of ^{134}Ce (3.2 days) allows for it to be compatible with antibody drug conjugates. This compatibility is investigated through microPET imaging $^{134}Ce^{III}$-DOTA-Trastuzumab in a SK-OV-3 tumor-bearing murine model. Because of the high *in vivo* stability of ^{134}Ce-DOTA and long half-life of ^{134}Ce, ^{134}Ce-DOTA-Trastuzumab displayed elevated tumor uptake for up to 9 days after administration and has a similar biodistribution to ^{225}Ac -DOTA -Trastuzumab. These proof of concept studies open the doorway for the development of targeting radiopharmaceuticals incorporating ^{134}Ce.

$^{86}Y^{III}$ (a positron emitter) and $^{90}Y^{III}$ (a β- emitter) are rare earth metal theranostic pairs that facilitate the implementation of the theranostic approach due to both the therapeutic and diagnostic radionuclides having identical chemistry. Due to HOPO's affinity for trivalent radiometals, HOPO can rapidly form highly stable yttrium complexes at room temperature, unlike DTPA or DOTA which are commonly used for $^{90}Y/^{86}Y$ theranostics. Through *in vivo* microPET imaging, the biodistribution and *in vivo* stability of ^{86}Y-HOPO are assayed in a murine model. ^{86}Y-HOPO displayed high *in vivo* stability and rapid pharmacokinetics, and it had negligible residual activity 24 hours after administration which is valuable for future work investigating yttrium-based targeting radiopharmaceuticals.

^{212}Pb, another promising α emitting radionuclide, is available in a convenient $^{224}Ra/^{212}Pb$ generator and has a diagnostic matched pair available, ^{203}Pb, which allows for SPECT imaging. A new elution strategy that directly yields ^{212}Pb in a more favorable electrolytic solution (1.0 M sodium acetate) for radiolabeling, circumventing the need for long evaporation and redissolution processes, is benchmarked by a series of radiolabeling experiments comparing this new strategy to the conventional one. Through two weeks of labeling experiments, this elution strategy minimized the time needed to elute the $^{225}Ra/^{212}Pb$, and it maintained a high radiochemical yield and radiochemical purity while labeling ^{212}Pb to TCMC-Trastuzumab conjugates. This novel elution strategy can facilitate the use of $^{224}Ra/^{212}Pb$ generators in clinical settings allowing a more widespread implementation of $^{212}Pb/^{203}Pb$ theranostics.

Siderocalin fusion proteins allow for a novel way to deliver therapeutic radionuclides to diseased sites. Because of Siderocalin's ability to non-covalently bind to highly stable, negatively charged metal-HOPO complexes, these fusion proteins can allow for rapid, room temperature radiolabeling compared to DOTA which requires high temperatures in order for quantitative radiolabeling. In order to investigate their tumor targeting and tumor control properties, *ex vivo* biodistribution and tumor control experiments are performed with ^{225}Ac and ^{90}Y labeled fusion proteins in a SK-OV-3 tumor-bearing murine model. While ^{225}Ac labeled fusion proteins were not able to display elevated uptake in tumors due to the low *in vivo* stability of ^{225}Ac-HOPO, the ^{90}Y fusion proteins were able to display tumor uptake within 50 hours. With further development, these Siderocalin fusion proteins can potentially become the blueprint for antibody-based "cold-kits".

CONTENTS

LIST OF FIGURES

LIST OF TABLES

ACKNOWLEDGEMENTS

First and foremost, I would like to thank Professor Rebecca Abergel for supporting me as a graduate student throughout the years, especially for her mentorship in manuscript writing and conference presentations, and for tolerating my eccentricities and various shenanigans throughout the years. I would also like to thank Professor Kai Vetter, Professor Lee Bernstein, and Professor Moriel Vandsburger for being on my quals and dissertation committee and for all their support.

I would like to thank Dr. Korey Carter, Dr. Katherine Shield, Dr. Jennifer Wacker, and Dr. Andrew Lakes for collaborating on the various ^{134}Ce and ^{86}Y experiments. I would also like to thank Dr. Jennifer Wacker, Dr. Korey Carter, and Dr. Alyssa Gaiser for working with me on the ^{212}Pb and Siderocalin Work. I learned way more about actinide chemistry and inorganic chemistry than I ever thought I would want to know through you all.

I owe a special debt to Dahlia An who mentored me throughout my years as a graduate student and for teaching me about biology and preclinical experimental design. I would further like to thank Dahlia An, Stacey Gauny, and her undergraduates, Joshua Chen, Elizabeth Wang, Pariswi Tewari, Zirui Jiang, Vicky Kang, Fion Chang, and Jesus Rios, for assisting with these experiments and other experiments that were not included in this dissertation. None of this would be possible without any of you.

I also would like to thank Dr. Yufei Wang, Dr. David Faulkner, Carla McKinley, Matthew Verlie, and Dahlia An for appreciating my sense of humor and giving me plenty of ideas for jokes.

I would personally like to thank my mom and dad, my two dogs, Gracie and Sophie, and my tortoise, Mudkip, for supporting me over the years. I would not have been able to get this without all of you.

I would like to personally thank collaborators from other labs for playing instrumental roles in all of this work. For the ^{134}Ce experiments, I would like to thank Dr. Stosh Kozimor and Dr. Veronika Mocko from Los Alamos National Laboratory for producing and shipping ^{134}Ce to Lawrence Berkeley National Laboratory and working with us on manuscripts. For the ^{224}Ra/^{212}Pb generator, I would to thank Matthew O'Hara and Dr. Lucas Boron-Brenner at Pacific Northwest National Lab for shipping us the ^{224}Ra/^{212}Pb generator and working with us on implementing the sodium acetate elution strategy. I would like to thank Dr. Roland Strong, Dr. Peter Rupert, and Matthew Buerger at Fred Hutchinson Cancer Research Center for producing the Siderocalin Fusion Proteins and shipping them to us at Lawrence Berkeley National Laboratory.

I would like to acknowledge that the ^{134}Ce work was supported by the Director, Office of Science, Office of Nuclear Physics, Isotope Production program of the U.S. Department of Energy under Contract Number DE-AC02-05CH11231 at LBNL.

CHAPTER 1: Introduction

1.1 Overview

Targeted radionuclide therapy has emerged as an effective option for treating cancer. While traditional radiotherapy directs radiation through the careful delivery of a collimated x-ray beam to the specific disease site (external beam therapy) or the placement of a seed containing a radiation source near the specific disease (brachytherapy), targeted radionuclide therapy relies on the administration of molecular agent with a radionuclide payload that has a high affinity for a specific receptor or antigen on the diseased site[1]. This molecular agent, acting as a "Zauberkugel" or "Magic Bullet" in the words of the German Nobel Laureate Paul Ehrlich, delivers its radionuclide payload to its target where the radionuclide emits ionizing radiation to disable or destroy the target[2]. These molecular agents (herein referred to as targeting radiopharmaceuticals) have taken a variety of forms over the years.

Starting in the 1940s, radioactive iodine isotopes (particularly ^{131}I and ^{128}I which are both β- emitters) were administered in patients with thyroid carcinomas without the aid of a molecular targeting vector (this radioactive iodine is administered as NaI which dissociates *in vivo*)[1]. These therapies were effective due to iodine's natural propensity for uptaking in the thyroid due to its role in producing thyroid hormones. ^{131}I soon was the dominant radioiodine to be in use for medical applications due to its longer half-life and its emission of a gamma photon. This photon allows ^{131}I to be imaged by an external device which allows for the same molecule to be used for diagnostics and therapy (*vide infra*). This idea of using the radionuclide's natural biodistribution as the targeting vector has been extended to recent times in the form of $^{223}RaCl_2$, which was FDA-approved in 2013 for treating patients with castration-resistant prostate cancer that has spread to the bone[3].

While relying on the natural biodistribution of the radionuclide is effective in some cases, more complex targeting vectors are required when the diseased tissue is not located on a "convenient" organ. One particular example is ^{131}I-meta-iodobenzylguanidine or ^{131}I-MIBG, an analogue of a catecholamine, which is a small molecule that is recognized by a receptor on adrenergic tissue. This targeted radiopharmaceutical has been used to treat unresectable (can't be surgically removed) or metastatic adrenergic tissue tumors since the 1990s and has recently been FDA-approved in 2018[4].

Another potential avenue for targeted radionuclide therapy is radioimmunotherapy where the radionuclide is labeled to a monoclonal antibody that targets a specific antigen on the diseased tissue[5]. The first two FDA-approved radiopharmaceuticals for radioimmunotherapy were ^{90}Y-tiuxetan-Ibritumomab (approved in 2002) and ^{131}I-Tositumomab (approved in 2003). Both of these targeting radiopharmaceuticals were used to treat CD20+ (the antigen) Non-Hodgkin's lymphoma. While the procedure for labeling ^{131}I to Tositumomab was simpler (^{131}I is just covalently bonded to the antibody itself), the preparation of ^{90}Y-tiuxetan-Ibritumomab is more involved since ^{90}Y is a metal and not a gas unlike ^{131}I and requires the use of a bifunctional chelator (tiuxetan) which binds to the ^{90}Y and antibody. In addition, ^{90}Y does not emit a gamma photon (it is a pure β- emitter); therefore imaging targeting

radiopharmaceuticals incorporating ^{90}Y requires swapping out ^{90}Y for a radionuclide that can be imaged. ^{111}In has commonly been used for this application even though it has different chemical properties than ^{90}Y[6]. Despite these complications, ^{90}Y-tiuxetan-Ibritumomab has some advantages and is still in use today since its more energetic β-particle allows for the more effective treatment of larger tumors because of the cross-fire effect. Moreover, ^{131}I-Tositumomab was removed from the market in 2014 due to limited use.

Another potential subset of targeted radionuclide therapy is through peptide receptor radionuclide therapy where peptides are instead used as the targeting vector. A popular application for peptide receptor radionuclide therapy has been for the treatment of neuroendocrine tumors[1]. A common feature of these types of tumors is that they are metastatic at the time of presentation, so resection of the primary tumor is not curative. It was discovered that these tumors expressed somatostatin receptors which could be inhibited by peptides. Early attempts at developing targeting radiopharmaceuticals to combat this type of cancer were to incorporate ^{90}Y (as a therapeutic agent) and ^{111}In (as a diagnostic agent) into peptides such as DOTA-TATE, DOTA-TOC, and DOTA-LAN (DOTA is a bifunctional chelator while the peptides TATE, TOC, and LAN are short for octreotate, octreotide, and lanreotide respectively). While these ^{90}Y labeled peptides yielded promising results, it was found that ^{177}Lu was more effective. ^{177}Lu has a lower β- energy than ^{90}Y which made it more effective at delivering high dose to micrometastases and smaller lesion sizes; in addition, ^{177}Lu also emits a gamma which also allows for imaging by single photon emission computed tomography. Because of this ^{177}Lu-DOTA-TATE was FDA approved in 2018[7].

While the vast majority of targeting radiopharmaceuticals have incorporated β-emitters, in the past couple of decades targeted radionuclide therapy with α emitters, or targeted alpha therapy, has been steadily expanding. This is because α particles deposit large amounts of energy in short distances (50-230 keV/um) compared to β-particles (0.1-1.0 keV/um) which makes α emitters rather effective against small tumor volumes, micrometastases, and circulating cells[8]. Alpha particles only travel 50-100 μm (5-10 cell diameters) in soft tissue, which minimizes energy deposition in nearby healthy cells, especially in comparison to beta particles which can travel 2,000-10,000 μm (200-1000 cell diameters). In addition, alpha particles efficiently produce double-stranded breaks in DNA, the dominant cause of cell death from radiation interactions, through direct ionization, which, unlike beta particles, is independent of tissue oxygenation[9,10]. Moreover, alpha emitters are effective at breaking chemotherapy-resistant, photon irradiation-resistant, and castration-resistant lesions[11,12].

While many alpha-emitting radionuclides have potential or are approved for medical use (^{223}Ra for instance), ^{225}Ac, ^{227}Th, and ^{212}Pb are the preeminent candidates for targeted alpha therapy[3,13,14]. This is due to ^{225}Ac and ^{227}Th having long decay chains including 4 or 5 alpha-emitting daughters, long half-lives granting adequate time for transportation, labeling, and compatibility with both peptides and monoclonal antibodies, and the lack of long-lived decay products that would deliver unnecessary dose to the patient. Moreover, there exists bifunctional chelators that allow for the sequestering of ^{225}Ac, ^{227}Th, and ^{212}Pb and the conjugation to targeting vectors. This is unlike ^{223}Ra, which lacks strong chelators, thereby limiting its oncological application due to its affinity to the bone mineral hydroxyapatite[15]. This non-specific uptake can lead to a large

uptake in both the metastases and healthy, actively growing bone, which contains hydroxyapatite as well. Coupling ^{225}Ac, ^{227}Th, or ^{212}Pb to targeting vectors circumnavigates this non-specific uptake and expands the use of alpha-emitters to other cancer types.

Auger electron-emitting radionuclides are another avenue that targeted radionuclide therapy can turn to. The low-energy electrons that these radionuclides emit in cascades deposit their energy in short ranges (1-23 keV/μm) with the highest energy auger electrons only going several microns in soft tissue[16]. While these electrons further minimize the chance of the cross-fire effect occurring and are considered more precise than even α particles, it is often thought that auger electron emitters require to be internalized inside the nuclear membrane (as close as possible to the DNA) to yield efficacious results. There has been some *in vitro* and *in vivo* evidence that demonstrated cytotoxic effects can be realized without nuclear internalization due to the bystander effect, but these studies are in the minority[17–19]. Because of these complications, clinical trials with auger electrons have been limited and have involved mainly ^{111}In and ^{125}I.

One reason for the prominence of ^{131}I in early targeted radionuclide therapy treatments was that ^{131}I also emitted a gamma photon which allowed for the imaging of its biodistribution. The emission of both of these particles allows targeting radiopharmaceuticals that incorporate ^{131}I to be used for therapy and diagnostics. Theranostics, the portmanteau of therapy and diagnostics, allows for patient-specific dosimetry to be determined and the preparation of a treatment plan for each individual patient[20]. This approach could determine whether a particular targeted radiopharmaceutical will benefit a particular patient and estimate whether it will lead to toxic side effects. While this idea isn't new, the widespread adoption of theranostics has been limited in targeted radionuclide therapy. The primary purpose of this dissertation is to discuss novel ways of advancing targeting radiopharmaceuticals to further facilitate the use of theranostics. While the radionuclides used can be radiometals (as is the case for ^{90}Y) or radioactive gases (as is the case for ^{131}I), this dissertation focuses on the use of radiometals as it allows for greater modularity (if an appropriate chelator is chosen, one radiometal can potentially be swapped for another while keeping everything else the same).

1.2 Targeting Radiopharmaceuticals

To facilitate the discussion of targeting radiopharmaceuticals throughout the rest of this dissertation, a discussion of a generalized model and all its individual components is warranted. Figure 1.1 illustrates the beforementioned model which is comprised of a therapeutic and/or diagnostic radiometal, a chelator, a targeting vector, and a linker that attaches the chelator to the targeting vector.

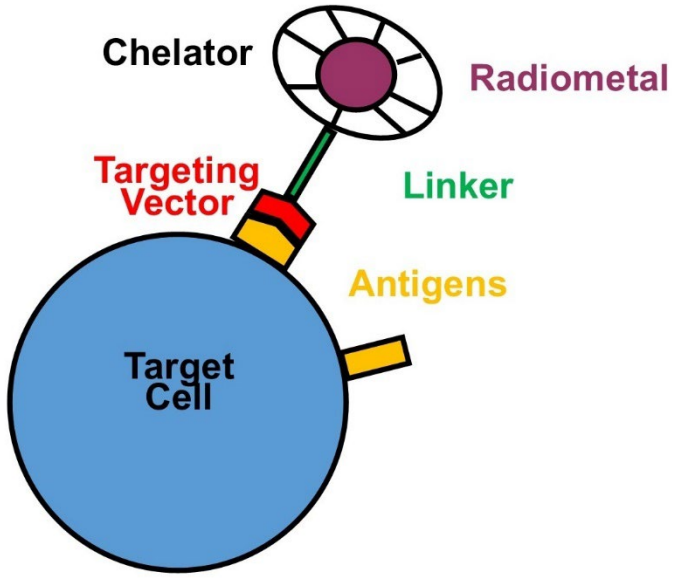

Figure 1.1: Generalized model of a targeted radiopharmaceutical.

1.2.1 Radiometals

In a targeted radiopharmaceutical, the radiometal can either be used for therapy, diagnostics, or both. If a different radiometal is used for therapy and diagnostics, both the radiometals must either have the same or similar chemistry for the theranostic approach to provide accurate dosimetry. This is because of the potential demetallation (or disassociation) of the radiometal from the chelator *in vivo* (*vide infra*). If this occurs, it is ideal for the therapeutic and diagnostic radiometal to have the same or similar chemistry because then they will have the same natural biodistribution. The therapeutic radiometals (and their companion diagnostics) that are discussed in this dissertation can be categorized into one of three different categories: theranostic radiometal, theranostic pair, and theranostic matched pair[13].

A theranostic radiometal allows for the same radiometal to be used for therapy and imaging. In addition to emitting an α particle, β- particle, or auger electron(s), the radiometal also emits a gamma photon or a positron with sufficient intensity that can be imaged by SPECT or positron emission tomography (PET), respectively. One common example is ^{177}Lu which emits a β- particle and 2 gamma photons (112.95 keV (6.23%) and 208.37 keV (10.41%))[7]. A more novel example that has received attention recently is ^{149}Tb which can either decay by α emission approximately 16.7% of the time or by positron emission followed by a cascade of gamma photons allowing for the ability to directly image this α emitter via PET or SPECT[21].

A theranostic pair is when the therapeutic radiometal and the diagnostic radiometal are of the same element. Because the two radiometals' chemistry is identical, their *in vivo* behavior is identical so the diagnostic targeted radiopharmaceutical can be used to accurately trace the biodistribution of the therapeutic targeted radiopharmaceutical. Two theranostic pairs that will be discussed

in detail in this dissertation include ^{90}Y (β- emitter) / ^{86}Y (positron emitter) and ^{212}Pb (α emitter) / ^{203}Pb (gamma emitter)[22,23]. Some other theranostic pairs that have also received interest in the past few years are ^{47}Sc (β- emitter) / ^{44}Sc (positron emitter) and ^{149}Tb (alpha and positron emitter) / ^{152}Tb (positron emitter) / ^{155}Tb (auger electron and gamma emitter) / ^{161}Tb (β- emitter)[24].

A theranostic matched pair is required when the therapeutic radiometal does not emit a gamma photon or positron with sufficient intensity. Because of this, a diagnostic radiometal with similar chemistry is required to allow for similar *in vivo* behavior. Due to limitations of contemporary clinical SPECT and PET scanners, theranostic matched pairs are required for ^{225}Ac and ^{227}Th, two alpha emitters that have displayed promising preclinical and clinical results, to perform accurate dosimetry and treatment planning. ^{68}Ga and ^{89}Zr (both positron emitters) have commonly been used as theranostic matched pairs for ^{225}Ac and ^{227}Th, respectively[11,25]. As will be discussed throughout this dissertation, both ^{68}Ga and ^{89}Zr unfortunately do not have similar chemistry to both ^{225}Ac and ^{227}Th.

1.2.2 Chelators

Chelators are organic molecules responsible for binding the therapeutic or diagnostic radiometal with high *in vivo* stability in targeting radiopharmaceuticals. If the chelator releases the radiometal *in vivo*, the radiometal may redistribute to its natural biodistribution and unnecessarily dose healthy organs, potentially leading to radiotoxicity and second cancers (Fig. 1.2)[26,27]. While using targeting vectors that rapidly internalize in diseased cells or administering the targeted radiopharmaceutical directly into the diseased tissue can mitigate this redistribution, for general applications it is ideal to use chelators that display high *in vivo* stability for the radiometal of interest. Moreover, it is beneficial for the chelator to display higher selectivity for the corresponding radiometal compared to endogenous metals (such as calcium, zinc, and copper) as this will prevent transmetallation which leads to the release of the radiometal. Throughout the experiments discussed in this dissertation, the following chelators were used: diethylenetriamine pentaacetic acid (DTPA), 1,4,7,10-Tetraazacyclododecane-1,4,7,10-tetraacetic acid (DOTA), 1,4,7,10-tetraaza-1,4,7,10-tetra(2-carbamoylmethyl)cyclododecane (TCMC), and 3,4,3-LI(1,2-hydroxypyridinone) (HOPO).

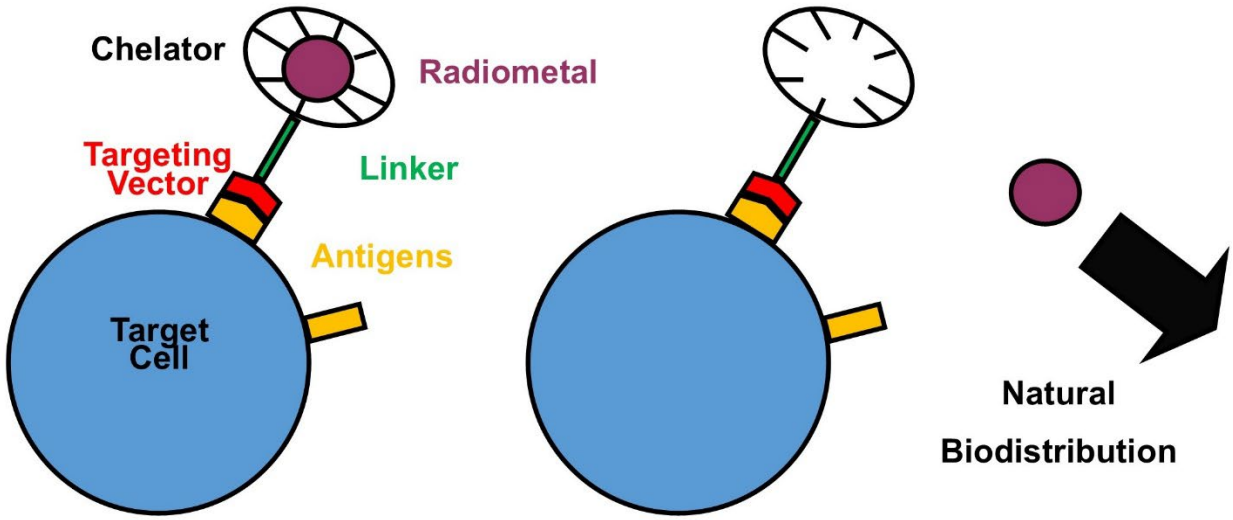

Figure 1.2: Diagram of the release of the radiometal from its chelator in targeting radiopharmaceuticals due to low *in vivo* stability of the metal-chelator complex.

DTPA (Fig. 1.3) and DOTA (Fig. 1.4) are both octadentate (capable of forming 8 coordinate bonds) chelators that have been used frequently with a variety of rare-earth (^{90}Y, ^{86}Y, ^{44}Sc, ^{47}Sc, and ^{177}Lu) and group 3 (^{68}Ga and ^{111}In) radiometals[28]. In addition, DOTA has been the most common chelator used for ^{225}Ac. DTPA is an acyclic (linear) chelator and allows for fast radiolabeling (5 to 15 minutes) at room temperatures. This fast radiolabeling is due to a low energetic barrier which unfortunately can cause DTPA complexes to have a low kinetic inertness, leading to the release of metals *in vivo*. DOTA, being a macrocycle, has a much higher energetic barrier towards dissociation which causes DOTA complexes to have a much higher *in vivo* stability than DTPA complexes. Unfortunately, this enhanced stability comes at a cost and requires elevated heating (50-95 °C) for longer periods of time (1 hour) to afford efficient radiolabeling, which is not always feasible when the radiometal has a short half-life or when the targeting vector is heat sensitive such as monoclonal antibodies.

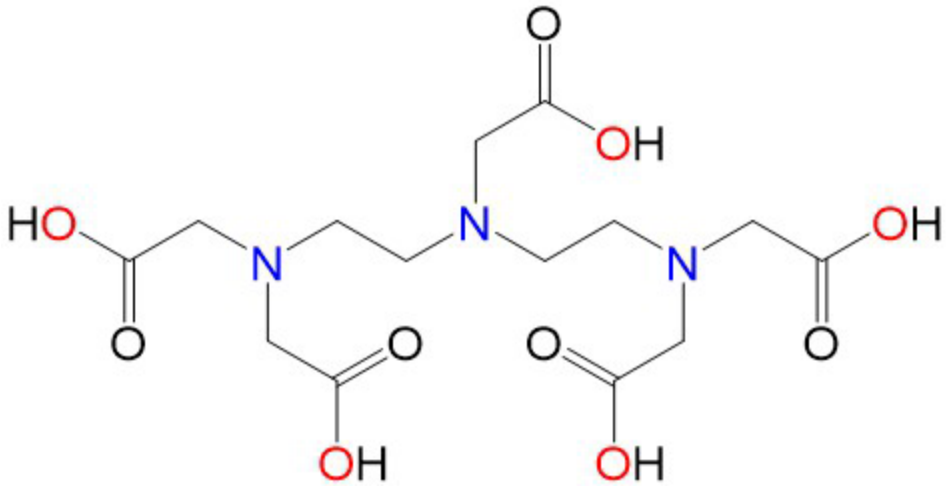

Figure 1.3: The chemical structure of DTPA. The red oxygens and the blue nitrogens are the coordinating atoms that bind to the metal when the oxygens are deprotonated.

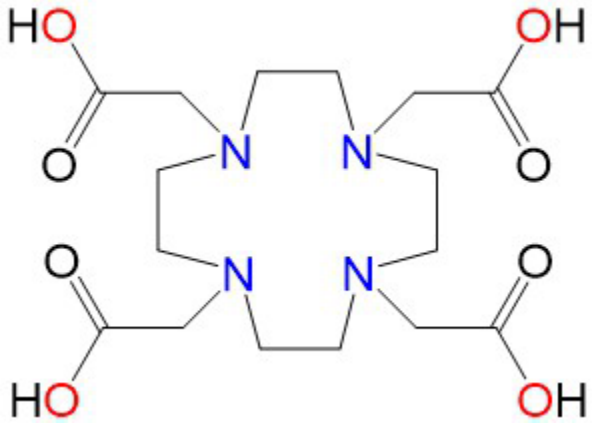

Figure 1.4: The chemical structure of DOTA. The red oxygens and the blue nitrogens are the coordinating atoms that bind to the metal when the oxygens are deprotonated.

In terms of chelators for $^{212}Pb/^{203}Pb$ theranostics, early preclinical studies used DOTA, but this leads to the high uptake of radiometal in the femurs which is indicative of ^{212}Pb release[13]. The macrocycle TCMC (Fig. 1.5), which has a cyclen ring like DOTA but uses amides to coordinate to metal instead of carboxylates, leads to more stable Pb complexes and is currently the gold standard for Pb-based targeting radiopharmaceuticals.

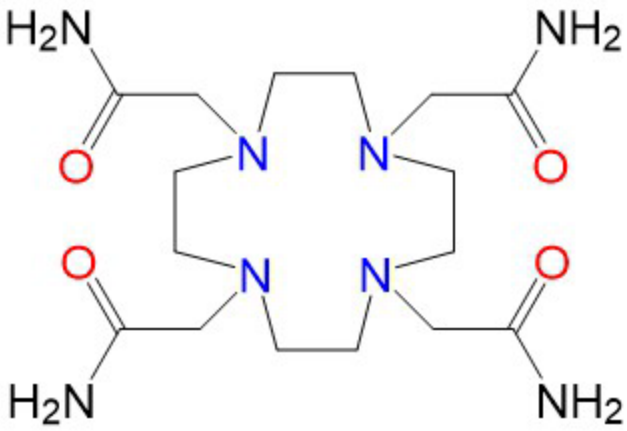

Figure 1.5: The chemical structure of TCMC. The red oxygens and the blue nitrogens are the coordinating atoms that bind to the metal when the oxygens are deprotonated.

While both ^{225}Ac and ^{227}Th fare better than ^{223}Ra in terms of compatible chelator availability, most chelators in medical use are optimized for transition and/or main group metals and not for rare earth elements or actinides[29]. While DOTA and DTPA have had some success, complexes formed with these chelators have low kinetic stability and unfavorable labeling conditions, which is detrimental to the development of targeting radiopharmaceuticals incorporating these strategic radiometals and demonstrating the need for developing new chelators[30]. In the past, the development of chelators for actinides has mainly been for the application of decorporation[31]. This development has mainly been focused on siderophore derivatives, which are a class of molecules that are typically produced by bacteria or fungi and used to traffic Fe^{III} to them. One of these chelators incorporates hydroxypyridinone moieties on a spermine base, 3,4,3-LI(1,2-HOPO) (Fig. 1.6), and has been shown to rapidly bind both trivalent and tetravalent actinides and rare earth metals with higher selectivity compared to divalent endogenous metals[32,33]. Furthermore, 3,4,3-LI(1,2-HOPO) allows for rapid, room temperature radiolabeling, which can facilitate its use as a chelator for targeting radiopharmaceuticals.

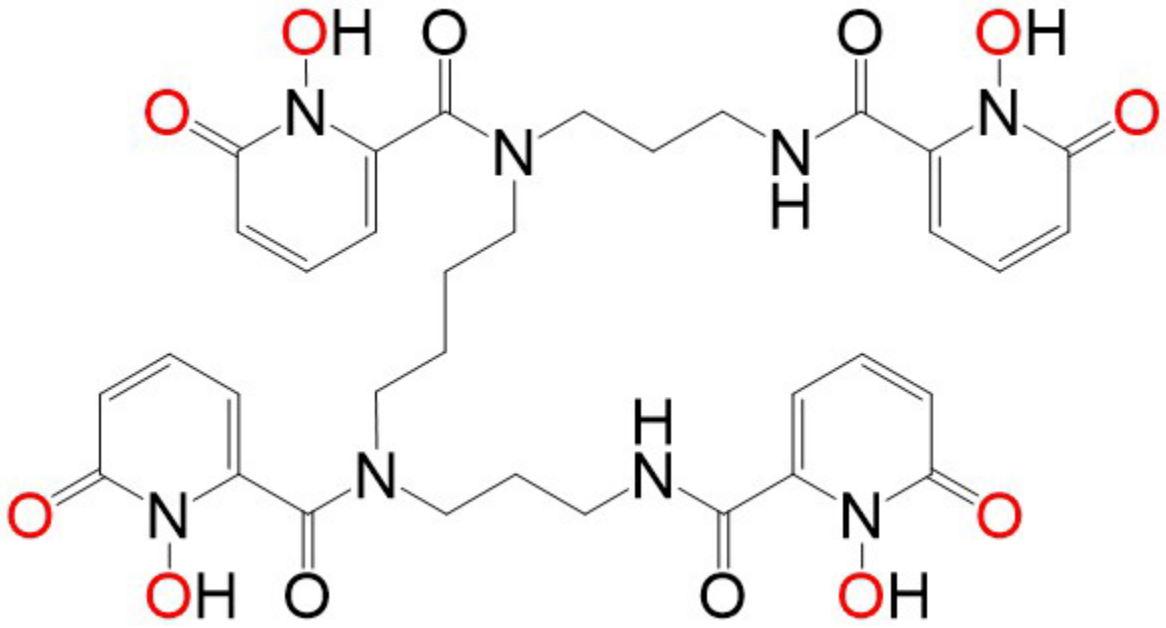

Figure 1.6: The chemical structure of 3,4,3-LI(1,2-HOPO). The red oxygens are the coordinating atoms that bind to the metal when the oxygens are deprotonated.

1.2.3 Targeting Vectors

The purpose of the targeting vector is to ferry the radioactive payload to the diseased tissue. Ideally, the targeting vector only binds to one type of receptor or antigen that is located on this diseased tissue, however there has been some exceptions where targeting occurs through the use of the radiometal's natural biodistribution (such as ^{131}I and ^{223}Ra)[1,3].

When using α emitters with long decay chains (such as ^{225}Ac, ^{227}Th, and ^{212}Pb), the emission of an α particle can cause the radioactive daughter nuclei to recoil which will release it from the chelator. This recoil effect can cause the daughter nuclei to redistribute away from the diseased site which decreases the therapeutic to toxicity ratio. One potential way to mitigate this effect is to utilize targeting vectors that internalize in the target cell[34].

Throughout this dissertation, the monoclonal antibody, Trastuzumab, will be employed as the targeting vector. Trastuzumab specifically targets the Human epidermal growth factor receptor 2 antigen (HER2), which can be overly expressed on breast cancers, ovarian cancers, and stomach cancers[35]. While Trastuzumab is primarily used as an FDA-approved immunotherapy drug, it has been used in targeting radiopharmaceuticals in previous preclinical and clinical experiments[36–38]. Because of this, the biodistribution of Trastuzumab is well known, allowing it to act as a platform for testing new strategies for targeting radiopharmaceuticals.

One of the disadvantages of using monoclonal antibodies in full Immunoglobulin G (IgG) form as a targeting vector is that they can take a few days to lead to elevated uptake in the lesion, which is disadvantageous if the radiometal has a short half-life[39]. The fragment antigen-binding (Fab) region of these antibodies can be isolated, which

allows for faster tumor uptake and can accommodate shorter-lived radiometals with the caveat that these fragments are eliminated from the body through the kidneys.

1.2.4 Linkers

The purpose of a linker is to attach the chelator to the targeting vector. This is typically done through the use of bifunctional chelators. These are chelators that have an organic molecule that is covalently attached to their structure that can be conjugated to the targeting vector and can also maintain their metal-binding functionality[40]. In this dissertation, this is done through the formation of thiourea bonds with isothiocyanatobenzyl (p-SCN-Bn) (which is the linker on the chelator) and the primary amine of lysine residues on the antibody. Figure 1.7 and Figure 1.8 display the chemical structures of ^{134}Ce-p-SCN-Bn-DOTA-Trastuzumab (or ^{134}Ce-DOTA-Trastuzumab) and ^{212}Pb-p-SCN-Bn-TCMC-Trastuzumab (or ^{212}Pb-TCMC-Trastuzumab), respectively as examples.

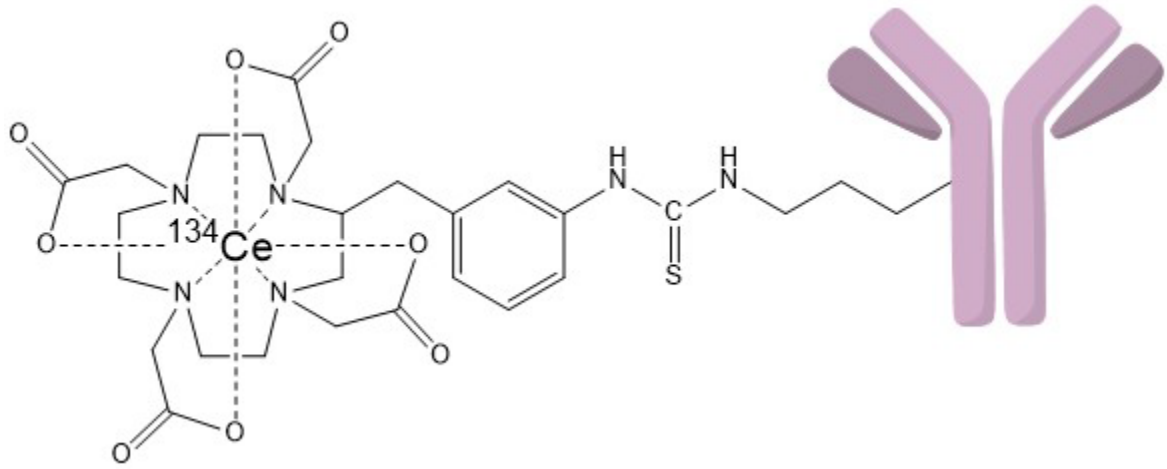

Figure 1.7: The chemical structure of ^{134}Ce-p-SCN-Bn-DOTA-Trastuzumab. The Y-shaped structure is Trastuzumab.

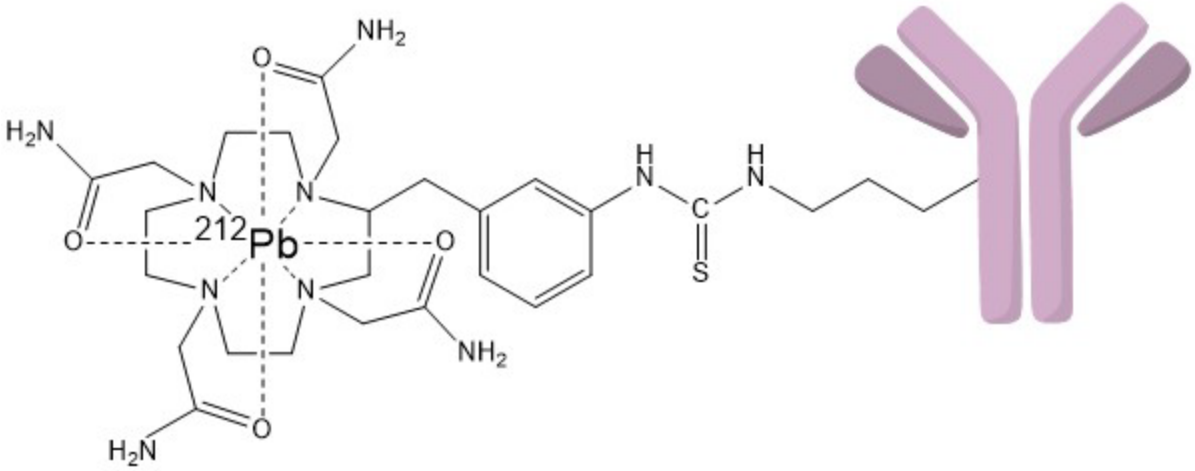

Figure 1.8: The chemical structure of ^{212}Pb-p-SCN-Bn-TCMC-Trastuzumab. The Y-shaped structure is Trastuzumab.

One of the disadvantages of 3,4,3-LI(1,2-HOPO) (HOPO) is that bifunctionalizing it has been challenging. While there has been a previously reported successful attempt to attach p-SCN-Bn to HOPO, this is a rather challenging synthesis process and has low yield, revealing the need to come up with other ways to link HOPO to targeting vectors[36]. One potential way that will be discussed in this dissertation is related to siderophore's biological function. Two rather common bacterial species, *Escherichia coli* and *Salmonella typhimurium*, emit the siderophore, enterobactin, which is a hexadentate chelator with a high affinity for iron[41]. Enterobactin will bind to this iron, forming a negatively charged complex, and bring the iron back to the bacteria. To prevent this iron acquisition, mammals have evolved to produce a protein called Siderocalin that will bind to these negatively charged complexes through non-covalent bonds and prevent the iron acquisition. Furthermore, if the iron is swapped with an actinide or rare earth metal, the strong electrostatic binding still occurs between Siderocalin and the negatively charged complex[42]. Interestingly, this mechanism also applies if enterobactin is swapped with HOPO and HOPO binds to a trivalent rare earth metal or actinide (since the HOPO complex is negatively charged). This non-covalent binding from the Siderocalin can potentially be used as a linker if the Siderocalin is attached to a targeting vector. Unfortunately this non-covalent binding doesn't occur with tetravalent metals and HOPO, which limits the utility of this mechanism.

1.3 Molecular Imaging

Through the theranostic approach, the same targeted radiopharmaceutical can be used for therapy as well as molecular imaging. Assaying the biodistribution of the targeted radiopharmaceutical can allow for the prediction of patient-specific efficacy, determination of patient-specific dosimetry, preparation of an appropriate treatment plan, and allow for the monitoring of treatment. This molecular imaging is typically done through SPECT and PET, which both allow for assaying the three-dimensional *in vivo* biodistribution of the targeted radiopharmaceutical.

Image formation with SPECT has traditionally relied on absorptive collimators (lead or tungsten septa), which has limited the sensitivity of this modality in comparison to PET. Luckily, recent advances in reconstruction algorithms and CT-based attenuation and scatter compensation techniques have made quantitative SPECT/CT possible, which allows for accurate dosimetry putting the modality on more equal footing with PET[43–45]. Unfortunately, limited sensitivity coupled with the limited amount of activity of ^{225}Ac and ^{227}Th that can safely be administered and the relatively weak gamma photon emissions from ^{225}Ac and ^{227}Th leads to images of the beforementioned radiometals to have low signal-to-noise ratios demonstrating the need for theranostic matched pairs[11,46]. One of the downsides of the use of theranostic matched pairs is that they are unable to trace the daughters of ^{225}Ac or ^{227}Th if they are not internalized in the target cell. Future SPECT scanners that incorporate CZT detectors, which enhance the energy resolution of the system, allowing for multi-radionuclide images, could allow for the imaging of daughters[47]. This coupled with the development of gamma cameras that do not require the use of collimators would be groundbreaking for the use of targeting radiopharmaceuticals incorporating ^{225}Ac and ^{227}Th[48,49].

Image formation with PET has been through electronic collimation, which leverages the approximate collinearity of high energy photons from positron annihilation removing the need for absorptive collimators. This approach has led to PET having much higher sensitivity than SPECT. This sensitivity has been increased 40-fold with the introduction of the EXPLORER total-body PET system[50]. This increased sensitivity allows for smaller amounts of activity required for imaging (reducing the radiation dose), shorter frame durations as small as 1 second which could allow for kinetic modeling (making dosimetry even more accurate), and allow for imaging extremely long timepoints such as imaging antibodies labeled with ^{89}Zr through 30 days after administration.

While PET offers increased sensitivity, certain positron emitters like ^{134}La and ^{68}Ga have high positron energies that can degrade the spatial resolution[51]. This is particularly troublesome for preclinical microPET systems (Appendix B). However, the development and implementation of faster and brighter scintillators (such as LSO(Ce), LYSO(Ce), and $LaBr_3$(Ce)) and silicon photomultiplier detectors have allowed for PET scanners to incorporate time-of-flight capabilities which can improve this spatial resolution[52,53]. In addition, these silicon photomultiplier detectors allow for multi-modality PET/MRI which offers excellent soft tissue contrast overlaid on PET images (compared to PET/CT) and further improvement of spatial resolution[54,55].

1.4 Organization of this dissertation

This dissertation presents the results of 5 targeting radiopharmaceutical research efforts organized in separate chapters

Chapter 2 discusses the therapeutic radiometals and their companion diagnostics that are prevalent in this dissertation. These therapeutic radiometals include the ^{90}Y (and its theranostic pair ^{86}Y), ^{212}Pb (and its theranostic pair ^{203}Pb), ^{225}Ac, and ^{227}Th with their potential theranostic matched pairs and their chemical similarities. Other aspects of these radiometals that are discussed include decay properties, natural biodistribution, potential chelators, preclinical and clinical applications, and production.

Chapter 3 describes experiments investigating the *in vivo* stability of novel complexes using microPET imaging. The two positron-emitting radionuclides discussed in this chapter include the novel ^{134}Ce/^{134}La *in vivo* generator system, which is a potential theranostic matched pair for both ^{225}Ac and ^{227}Th and ^{86}Y, which is a theranostic pair for ^{90}Y. These experiments elucidate which chelators have a high affinity for both of these radiometals and pave the way for targeting radiopharmaceuticals to incorporate these complexes.

Chapter 4 describes an experiment that demonstrates the ability of ^{134}Ce/^{134}La to allow for long tumor imaging through antibody-based targeting radiopharmaceuticals due to the long half-life of ^{134}Ce. This is tested by administering ^{134}Ce-DOTA-Trastuzumab in a SK-OV-3 tumor-bearing murine model and imaging the biodistribution over 9 days via a microPET scanner. This proof of concept also demonstrates that ^{134}Ce can be used as a theranostic matched pair for ^{225}Ac in antibody-based targeting radiopharmaceuticals.

Chapter 5 describes an experiment that benchmarks a novel elution strategy of ^{224}Ra/^{212}Pb generators. This elution strategy is benchmarked through labeling TCMC-conjugated Trastuzumab and using radiochemical yield and radiochemical purity as metrics to compare this new strategy with the currently used strategies. This experiment shows that this new strategy can optimize the production of targeting radiopharmaceuticals incorporating ^{212}Pb by allowing for more activity to be labeled, which potentially allows for more patients to be treated.

Chapter 6 describes experiments that test the tumor control capabilities and biodistribution of siderocalin fusion proteins with ^{225}Ac and ^{90}Y. Instead of utilizing covalent bonds, these fusion proteins allow for labeling targeting vectors with non-covalent interactions. These experiments allow for the incorporation of highly stable 3,4,3-LI(1,2-HOPO) complexes in targeting radiopharmaceuticals and potentially open the doorway for antibody-based cold-kits.

Appendix A discusses the spatial resolution of the microPET scanner used for this dissertation. Appendix B discusses the definitions of radiochemical yield and radiochemical purity when producing targeting radiopharmaceuticals.

CHAPTER 2: Radionuclides of theranostic interest

2.1 Introduction

This dissertation discusses the advancement of targeting radiopharmaceuticals incorporating the following therapeutic radionuclides: ^{225}Ac, ^{227}Th, ^{212}Pb, and ^{90}Y. While β- emitters such as ^{90}Y have seen the most clinical use, the application of α emitters (^{225}Ac, ^{227}Th, and ^{212}Pb) in targeting radiopharmaceuticals has been increasing due to their effectiveness against smaller lesions and their ability to break chemotherapy-resistant, photon irradiation-resistant, and castration-resistant lesions[8,11,12]. In particular, ^{225}Ac-PSMA-617 and Targeted Thorium-227 Conjugates have shown promising preclinical and clinical results[11,25].

While ^{90}Y and ^{212}Pb have theranostic pairs, ^{86}Y and ^{203}Pb, that share the same chemical properties and can be imaged by PET or SPECT facilitating the theranostic approach, ^{225}Ac and ^{227}Th lack theranostic pairs or suitable decay characteristics for direct imaging with contemporary molecular imaging modalities. Because of this, theranostic matched pairs that have similar chemical properties and can be imaged need to be developed. Potential theranostic matched pairs for these promising radionuclides are discussed here. Other metrics include decay properties, natural biodistribution, potential chelators, preclinical and clinical applications, and production.

2.2 Actinium-225 and its theranostic matched pairs

2.2.1 Actinium-225

^{225}Ac ($T_{1/2}$ =9.9 days) decays via a series of 4 alpha emissions to essentially stable ^{209}Bi (^{209}Bi has a half-life of 2 x 10^{19} years) (Fig. 2.1). Like other large trivalent actinides (ionic radius: 112 pm (coordination number = 6)), ^{225}Ac predominately accumulates in the liver in rodents, with much of the rest accumulating in the skeletal system[56–58]. If ^{225}Ac is not internalized, two of its longer-lived daughters, ^{213}Bi ($T_{1/2}$=45.6 minutes) and ^{221}Fr ($T_{1/2}$=4.8 minutes), have been shown to accumulate in the kidneys[34]. There has been some preclinical evidence that this uptake can lead to long-term renal toxicity[59]. This long-term renal toxicity can translate to the clinical setting with three patients developing chronic kidney disease after treatment with the targeting radiopharmaceutical ^{225}Ac-PSMA-617 for metastatic, castration-resistant prostate cancer[26]. While the incidence of ^{225}Ac therapy-associated kidney disease is rather rare (in this study, 3 patients developed kidney disease out of 33 patients treated with ^{225}Ac-PSMA-617), it is necessary to develop strategies for both the targeted internalization in diseased cells and the determination of accurate dosimetry for ^{225}Ac-based targeting radiopharmaceuticals.

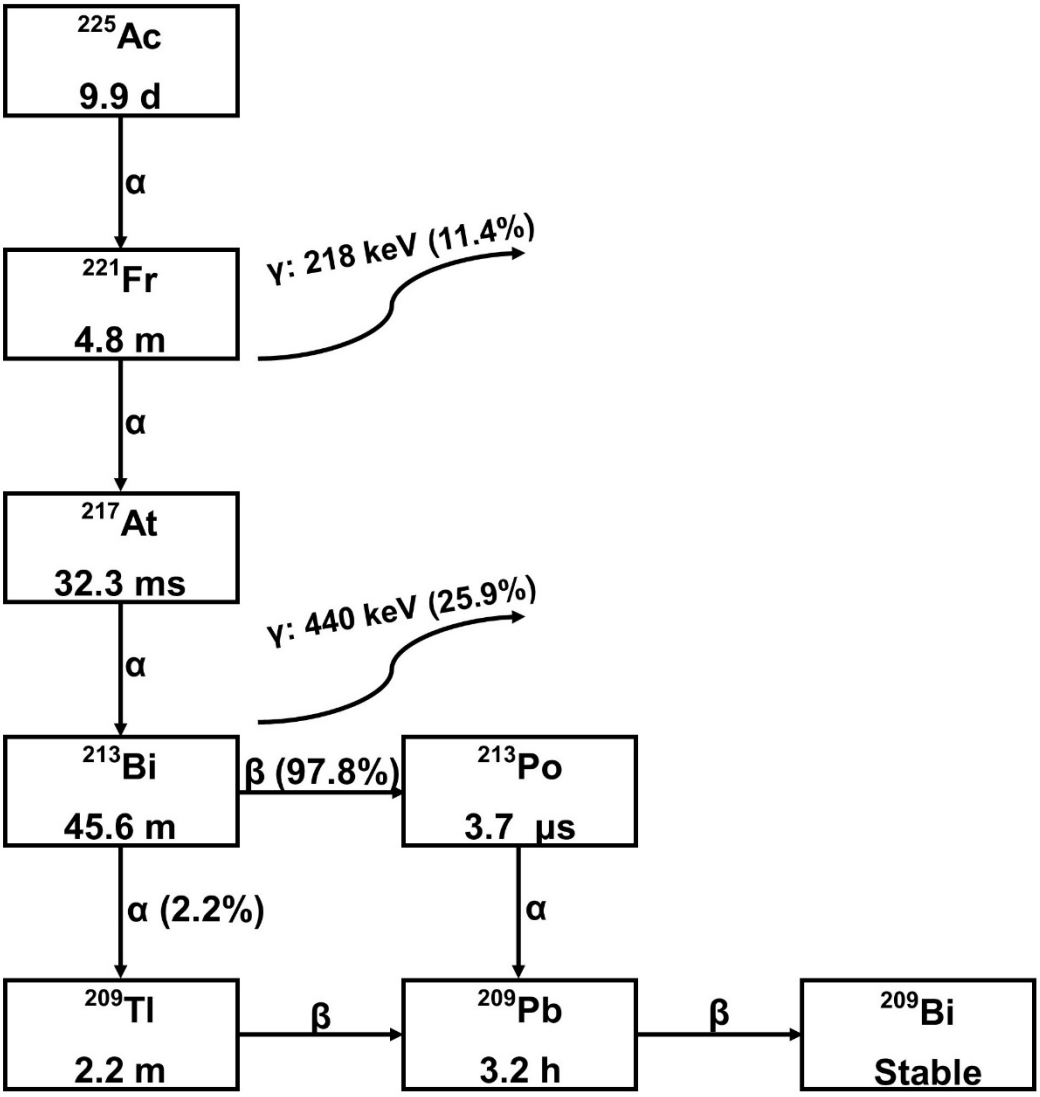

Figure 2.1: ^{225}Ac decay chain with the imageable radiation emitted by ^{225}Ac and its daughters included.

The large ionic radius of ^{225}Ac and the lack of long-lived actinium isotopes has made the development of chelators challenging. An early study evaluated the biodistribution of a few ligands in healthy female BALB/c mice (a mouse model that allows for the implantation of human xenograft tumors since they are immunodeficient). These ligands include ethylenediaminetetraacetic acid (EDTA), N-[(R)-2-amino-3-(4-nitrophenyl)propyl]-trans- (S,S)-cyclohexane-1,2-diamine-N,N,N′,N″,N″-pentaacetic acid (CHX-A" DTPA), 1,4,7,10-tetraazacyclododecaneN,N′,N″,N‴-tetraacetic acid (DOTA), 1,4,7,10,13- pentaazacyclopentadecane-N,N′,N″,N‴,N⁗-pentaacetic acid (PEPA), and 1,4,7,10,13,16- hexaazacyclohexadecane-N,N′,N″,N‴,N⁗,N⁗′-hexaacetic acid (HEHA)[57]. Both acyclic ligands (EDTA and CHX-A" DTPA) led to increased skeletal and liver uptake with the liver uptake increasing over time, indicating low *in vivo* stability of the complex. The macrocyclic ligands (DOTA, PEPA, and HEHA) fared better even

though DOTA and PEPA still led to accumulation over time in the liver. At the time of this study, this led to the belief that macrocyclics with larger atom ring sizes were necessary to saturate the coordination sphere of ^{225}Ac in order to form stable complexes (HEHA has an 18 atom ring while PEPA and DOTA only have a 15 atom ring and a 12 atom ring, respectively). However upon testing serum stability with an ^{225}Ac-labeled antibody drug conjugate (CC49) incorporating HEHA (2-(4-isothiocyanatobenzyl)-1,4,7,10,13,16-hexaazacyclohexadecane-1,4,7,10,13, 16-hexaacetic acid), approximately only two-thirds of the antibody drug conjugate was intact by 5 hours[60]. More recently, the use of a 1-step labeling procedure involving ^{225}Ac-labeled antibody drug conjugate (Lintuzumab) was investigated with both S-2-(4-Isothiocyanatobenzyl)-1,4,7,10-tetraazacyclododecane tetraacetic acid (p-SCN-Bn-DOTA) and 1,4,7,10-Tetraazacyclododecane-1,4,7,10-tetraacetic acid mono-N-hydroxysuccinimide (NHS-DOTA), with the former differing from the latter with an extra carboxylate group for binding[61]. The p-SCN-Bn-DOTA conjugate in comparison to the NHS-DOTA conjugate, which only has 7 donor atoms compared to p-SCN-Bn-DOTA having 8 donor atoms, was shown to have both higher radiochemical yield (52.2% versus 10.5%) and higher radiochemical purity (98.3% versus 69.1%), demonstrating the need for a higher coordination number for ^{225}Ac. In addition, the biodistribution in healthy BALB/c mice indicated a lack of time-dependent liver accumulation, which is indicative of high *in vivo* stability. Recently, the 18 atom ring macrocyclic macropa was rapidly labeled at room temperature in an antibody format with ^{225}Ac with a radiochemical yield of greater than 99% and exceptionally high stability[62]. While DOTA-based chelators are currently the most commonly used for ^{225}Ac, they require elevated temperatures to ensure quantitative labeling. Rapid room-temperature binding from macropa could be game-changing.

While the majority of ^{225}Ac-based radiopharmaceutical development has used DOTA and other macrocyclic chelators, there has been some evidence that acyclic ligands with picolinic acid moieties have a high affinity for ^{225}Ac as well. As an example, at 1 micromolar Py4pa was able to achieve 97% radiochemical yield when labeling ^{225}Ac at room temperature for 30 minutes[63]. In comparison, at 100 micromolar and under the same conditions, DOTA was only able to achieve 75% radiochemical yield. Furthermore, a biodistribution study of ^{225}Ac-Py4pa-Trastuzumab in SK-OV-3 tumor-bearing NOD.Cg-Rag1tm1Mom Il2rgtm1Wjl/SzJ (NRG) mouse model (a mouse model that allows for the implantation of human xenograft tumors since they are immunodeficient) showed excellent tumor targeting over 10 days with similar liver uptake compared to ^{225}Ac-DOTA-Trastuzumab. Other acyclic chelators with picolinic acid moieties, such as Bispa^2, CHXoctapa, and noneunpa, have also demonstrated high radiochemical yields (98% at 100 μM concentration, 94% at 1 μM, and 95% at 1 μM respectively) at room temperature labeling conditions[64–66].

While still on the trend of acyclic chelators, hydroxypyridinone-based chelators may show a high affinity for ^{225}Ac as well. In particular, 3,4,3-LI(1,2-HOPO) has been shown to offer fast binding kinetics at room temperature and high *in vivo* for both trivalent and tetravalent *f*-elements[67,68]. To test this hypothesis, Chapter 6 discusses an experiment that investigated the biodistribution of ^{225}Ac-3,4,3-LI(1,2-HOPO) non-covalently bound to Siderocalin-Trastuzumab fusion proteins in SK-OV-3 tumor-bearing

NOD SCID mice (an immunocompromised mouse model that is used predominately in the Bioactinide Chemistry Group for tumor imaging and tumor control studies).

One of the challenges that plagues ^{225}Ac is its lack of availability. In the US, the ^{225}Ac that is used for clinical trials is supplied through the elution of ^{229}Th generators at Oak Ridge National Laboratory, which can produce approximately 2.2 GBq per month[69]. To provide perspective, one of the patients with castration-resistant, metastatic prostate cancer in the Kratochwil, *et al*. study received fractions of 6.5 MBq of ^{225}Ac-PSMA-617[11]. This would only allow 338 patients per month to receive this exact fraction dose, and this number is neglecting decay and loss of activity during transport and radiolabeling procedures. While this is rather low, the production method does produce ^{225}Ac clean of radioactive impurities.

As an alternative to generator produced ^{225}Ac, Oak Ridge National Laboratory, Brookhaven National Laboratory, and Los Alamos National Laboratory have teamed up to produce ^{225}Ac through the ^{232}Th(p, x)^{225}Ac reaction[70]. This endeavor has been projected to be able to produce approximately 3120 GBq per month (about 1418 times more activity than the US supply from ^{229}Th generators[69]. Unfortunately, this method coproduces the long-lived radioisotope ^{227}Ac ($T_{1/2}$ =21.8 years) at an ^{227}Ac to ^{225}Ac activity ratio of up to 0.2%. In terms of atoms, this leads to approximately 1.6 atoms of ^{227}Ac to 1 atom of ^{225}Ac. While it is currently unclear what the long term impact of this ^{227}Ac impurity especially if it is released from its targeting vector *in vivo* and whether it is safe for clinical use, accelerator-produced ^{225}Ac provides a challenge from the radiolabeling front, since a high excess of chelator to metal is often needed for high radiochemical yields even just for generator produced ^{225}Ac[71].

From an imaging standpoint, ^{225}Ac does not directly emit high intensity photons that can be imaged by SPECT. In addition, the decay chain does not emit positrons, which forgoes the option of using PET as well. Attempts have been made to image gammas from the ^{221}Fr and ^{213}Bi daughters, which have 218 keV (11.44%) and 440.45 keV (25.94%) respectively[11,72,73]. Unfortunately, this does not image ^{225}Ac directly but instead images the distribution of the daughters, and they may have different distributions due to redistribution. Moreover, due to the potency of alpha emitters, the activity of ^{225}Ac that can safely be injected is rather low in comparison to more traditional SPECT isotopes. As a result, the number of photons emitted by ^{225}Ac is inadequate for contemporary clinical SPECT scanners. This leads to images with low signal-to-noise ratios and contrast which minimizes the amount of useful information that can be gathered. As an example, Figure 2.2 shows posttherapeutic planar scans of ^{68}Ga-PSMA-11, ^{177}Lu-PSMA-617, and ^{225}Ac-PSMA-617[11]. The ^{225}Ac-PSMA-617 images (Fig. 2.2e and 2.2f) where the dose administered was 100 kBq/kg have a significantly lower signal-to-noise ratio than the ^{177}Lu-PSMA-617 images (Fig. 2.2b and 2.2c) where the dose administered was 114 MBq/kg. Because of this, the co-development of theranostic matched pairs of ^{225}Ac is warranted. Table 2.1 summarizes ^{225}Ac and its theranostic matched pairs including half-life, imageable radiation, chelators, and targeting vectors.

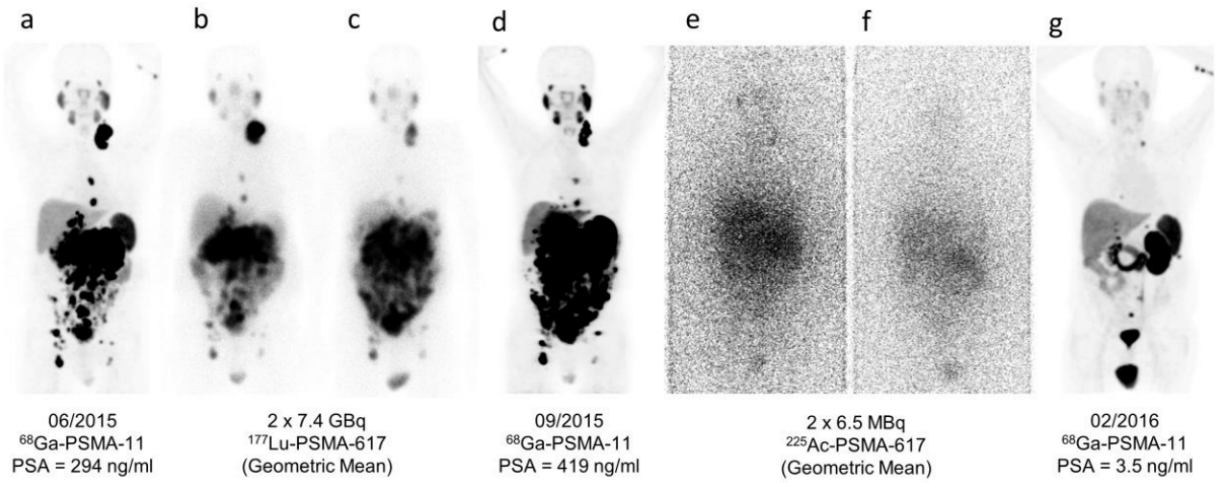

Figure 2.2: Postherapeutic planar scans of (a and g) ^{68}Ga-PSMA-11, (b and c) ^{177}Lu-PSMA-617, and (e and f) ^{225}Ac-PSMA-617. This research was originally published by Kratochwil C, Bruchertseifer F, Giesel FL, et al. in the Journal of Nuclear Medicine[11].

Table 2.1: Summary of ^{225}Ac and its theranostic matched pairs.

Radionuclide	Half-Life	Ionic Radius[56,a]	Imageable Radiation	Chelators	Targeting Vectors
^{225}Ac	9.9 d	112 pm	^{221}Fr γ: 218 keV (11.44%); ^{213}Bi γ: 440.45 keV (25.94%)	EDTA[57], CHX-A" DTPA[57] PEPA[57] DOTA[38,57,61–63,74–78] HEHA[57,60] Macropa[62] Py4pa[63] Bispa2[64] CHXoctapa[65] Noneunpa[66] 3,4,3-LI(1,2-HOPO)[d]	CC49[60] Lintuzumab[61] Trastuzumab[38,62,63,d] single-chain variable fragment[74] hTAB004[75] PP-F11N[76] Cixutumumab[77] PSMA617[11,26] NM600[78]
^{68}Ga	67.7 m	62 pm	β+: E(β+)=829.5 keV (88.91%)	DOTA[73,79–82] HBED-CC[11,82]	DOTATATE[73] Neurotensin[81] PSMA11[11]
^{132}La	4.8 h	116 pm	β+: E(β+)=1.29 MeV (42.10%)	DOTA[78] Macropa[83]	NM600[78] DUPA[83]
^{133}La	3.9 h	116 pm	β+: E(β+)=460 keV (7.20%)	DOTA[84] Macropa[84]	PSMA-I&T[84]
^{111}In	2.8 d	92 pm	γ: 171.28 keV (90.7%); γ: 245.35 keV (94.1%)	DOTA[38,74–77] Bispa2 [64] Noneunpa[66]	Trastuzumab[38] Single-chain variable fragment[74] hTAB004[75] PP-F11N[76] Cixutumumab[77]
^{134}Ce^{III}/^{134}La	3.2 d / 6.5 m	114 pm	^{134}La β+: E(β+)=1.22 MeV (63.6%)	DTPA[85,b] DOTA[b]	Trastuzumab[c]

[a]For ^{225}Ac and ^{68}Ga, the ionic radius is given for a coordination number of 6. For every other element, the ionic radius is given for a coordination number of 8
[b]Chapter 3
[c]Chapter 4
[d]Chapter 6

2.2.2 Gallium-68

^{68}Ga ($T_{1/2}$ = 67.7 minutes) is one of the more popular theranostic matched pair in the clinical setting for ^{225}Ac and is predominately used as an analogue for ^{225}Ac-

PSMA617 as ^{68}Ga-PSMA11[11,26]. This is due in part to it being a PET isotope with a high branching ratio (88.9%) and its availability in a ^{68}Ge ($T_{1/2}$=270.9 days)/^{68}Ga generator system, foregoing the need for on-site production[86]. The utility of ^{68}Ga being a surrogate for ^{225}Ac ends there, however. Although gallium is a trivalent cation in physiological conditions, gallium has an ionic radius that is almost half the size of actinium's ionic radius (62 pm versus 112 pm at coordination number = 6) and behaves more like an iron surrogate than an actinium surrogate in vivo[56]. In fact, gallium-citrate accumulates predominately in the kidneys, heart, blood, and lungs instead of in the liver and skeleton in rodents[87,88]. This is due to transferrin, a plasma glycoprotein in vertebrates that is responsible for transporting iron, and its high affinity for gallium[89].

Gallium's small size limits its stability with DOTA due to Ga-DOTA complexes having 2 free carboxylate groups[79,80]. In addition, the need for heating to facilitate labeling DOTA, which can take up to an hour, is another constraint due to the short half-life of ^{68}Ga. Despite this, DOTA has seen some use for gallium-actinium theranostics with DOTATE in the clinical setting and DOTA-Neurotensin analogs in the preclinical setting[73,81].

Another commonly used chelator for gallium-actinium theranostics is the hexadentate acyclic ligand bis(2- hydroxybenzyl)ethylenediaminediacetic acid (HBED); its derivative, HBED-CC, is most commonly used in ^{68}Ga-PSMA11[11]. HBED offers both higher stability for gallium and allows for higher radiochemical yield (>80%) at room temperature[82]. While certainly advantageous compared to radiolabeling with DOTA, the high stability of ^{68}Ga-HBED does not "match" well to ^{225}Ac-DOTA found in ^{225}Ac-PSMA-617, which can demetallate *in vivo* due to the lower *in vivo* stability of ^{225}Ac-DOTA[57]. Because of this, pretreatment dosimetry using ^{68}Ga-PSMA-11 may not account for the impact of this demetallation and may be inaccurate.

One of the other downsides of utilizing ^{68}Ga as a theranostic matched pair for ^{225}Ac is the difference in half-life (67.7 minutes versus 9.9 days). While the short half-life of ^{68}Ga is optimal for small, rapidly uptaking peptides due to the diminished radiation dose imparted on the patient, ^{68}Ga can only mirror the acute biodistribution of the radiopharmaceutical incorporating ^{225}Ac. In addition, the short half-life of ^{68}Ga is incompatible when treatment planning for ^{225}Ac labeled antibody drug conjugates due to antibodies having both a longer biological life time and uptaking much slower in diseased tissue compared to peptides. This long-term compatibility versus radiation dose should be taken into account when choosing a theranostic matched pair, especially due to recent reports of long-term chronic kidney disease in some patients after being treated with ^{225}Ac-PSMA617 as mentioned previously[26].

2.2.3 Radiolanthanums: Lanthanum-132 and Lanthanum-135

^{132}La ($T_{1/2}$=4.8 hours) and ^{133}La ($T_{1/2}$=3.9 hours) are two relatively new PET radionuclides that can act as theranostic matched pairs for ^{225}Ac. Lanthanum (ionic radius: 116 pm (coordination number = 8)) in particular is well matched to actinium because they are trivalent in physiological conditions and have similar ionic radii[56]. ^{132}La was shown to mirror ^{225}Ac's natural biodistribution by accumulating predominately in the liver with much of the rest in the bone[90]. In addition, the DOTA-based small molecule alkylphosphocholine (NM600) was used to verify this surrogacy of ^{225}Ac and ^{132}La in a murine mammary adenocarcinoma 4T1 model through 24 hours[78]. Promising

radiolabeling and *in vivo* tumor targeting results were shown as well with ^{133}La-PSMA-I&T (a DOTA-based peptide) in LNCaP tumor-bearing NU/NU Nude mice (a mouse model that allows for the implantation of human xenograft tumors since they are immunodeficient)[84]. While DOTA has been shown to form suitably stable complexes with the radiolanthanums, the 18 atom ring macrocycle macropa has been shown to be labeled with ^{132}La rapidly at room temperature with a high yield in comparison to DOTA[83]. This compatibility with radiolanthanums and ^{225}Ac may make macropa a cornerstone in actinium-lanthanum theranostics. Unfortunately, like ^{68}Ga, both radiolanthanum's short half-lives do not allow for the imaging of long timepoints, which makes its potential long-term accumulation in the liver more difficult to image. This relegates radiolanthums to only small molecule applications.

While both ^{132}La and ^{133}La can be produced using natural barium targets, only ^{132}La can be produced using on-site low energy cyclotrons (11.9 MeV proton beam)[90,91]. ^{135}La requires a higher proton energy of 22 MeV which is out of reach of most medical cyclotrons which may limit availability. Despite this, ^{133}La grants a better spatial resolution compared to ^{132}La since it has a lower average positron energy (0.46 MeV versus 1.29 MeV) and is more dosimetrically favorable since it emits fewer gammas. Unfortunately, the longer-lived, Auger electron emitting ^{135}La ($T_{1/2}$=19.5 hours) is also coproduced with both isotopes. While ^{135}La minimally impacts the image formation (it has 1 gamma at 480.51 keV with an intensity of 1.52% that can lead to a small number of false coincidences), it does impart unnecessary dose. For ^{133}La, the amount of ^{133}La produced is much smaller than for ^{132}La. The ratio of ^{135}La to ^{133}La (at 22 MeV) shortly after the end of bombardment is only 0.72 while the ratio of ^{135}La to ^{132}La (at 11.9 MeV) is 18[91]. Using enriched ^{132}Ba targets and increasing the proton energy could decrease the ^{135}La to ^{132}La ratio; however, there are currently no published results that support this[90]. Despite this, the use of the Auger electrons from ^{135} La could potentially be used for added therapeutic effect in actinium-lanthanum theranostics or could be leveraged for radiopharmaceuticals only incorporating ^{132}La/^{133}La and ^{135}La as matched pairs.

2.2.4 Indium-111

^{111}In ($T_{1/2}$=2.8 days) is a SPECT radionuclide (it has two intense gammas at 171.28 keV and 245.35 keV with intensities of 90.7% and 94.1% respectively) that has been commonly been used as a theranostic matched pair for ^{225}Ac due to its widespread availability and prevalence in clinical settings[92]. Moreover, its long half-life allows for compatibility with larger macromolecules such as antibodies and opens the gateway for acting as a surrogate for ^{225}Ac for longer timepoints. Even though the trivalent ^{111}In matches ^{225}Ac better than ^{68}Ga matches ^{225}Ac due to its larger ionic radius (ionic radius: 92 pm (coordination number = 8)), ^{111}In has more in common with ^{68}Ga *in vivo* since transferrin has a high affinity for both ^{111}In and ^{68}Ga[56,89,93]. This difference in natural biodistribution when compared to ^{225}Ac may limit the ability of ^{111}In to see time-dependent liver accumulation, which is common with ^{225}Ac-based radiopharmaceuticals.

Unlike ^{68}Ga, ^{111}In forms stable, non-deformed complexes with DOTA since the larger indium cation allows for octadentate coordination[79]. Because of DOTA's compatibility with both actinium and indium, virtually all of the investigations utilizing indium-actinium theranostics use DOTA[38,74–77]. As mentioned previously, ^{225}Ac-DOTA complexes are not stable in the long term and the requirement for heating is detrimental

for labeling larger macromolecules like antibodies. Luckily, the 18 atom ring chelator macropa may also display a high affinity for ^{111}In since actinium and indium have similar ionic radii[62]. In addition, the acyclic ligands with picolinic acid moieties bispa^2 and noneunpa have shown high radiochemical yields (>99% at 100 nM and 91% at 1 μM, respectively) when labeling with ^{111}In at room temperature which are comparable to the yields achieved with ^{225}Ac[64,66].

Cheal, et al. directly compared the biodistribution of single chain variable fragments incorporating ^{225}Ac and ^{111}In in colorectal SW1222 tumor-bearing athymic nude mice (a mouse model that allows for the implantation of human xenograft tumors since they are immunodeficient)[74]. Both of the radionuclides had a similar tumor uptake and follow a similar biodistribution with the exception of the ^{225}Ac accumulating more in the bone and the liver in comparison to indium at 24 hours. Borchardt, et al. also directly compared the biodistribution of ^{225}Ac-DOTA-Trastuzumab and ^{111}In-DOTA-Trastuzumab in ovarian SKOV3-NMP2 tumor-bearing nude mice[38]. Interestingly, no difference was found for ^{225}Ac and ^{111}In in bone and liver uptake in this study. Because of the longer half-life of ^{111}In, actinium-indium theranostics can be applied both to small rapidly uptaking targeting vectors such as single chain variable fragments and larger, slower uptaking targeting vectors such as antibodies.

2.2.5 Cerium(III)-134/Lanthanum-134

^{134}Ce ($T_{1/2}$=3.2 days)/^{134}La ($T_{1/2}$=6.5 minutes) is an *in vivo* generator system in which ^{134}Ce is incorporated in the radiopharmaceutical and then decays *in vivo* to ^{134}La, which can be imaged with PET since it decays via positron emission[94]. The long half-life of the parent allows for the imaging of both fast and slow uptaking targeting vectors unlike the radiolanthanums. However, the high average positron energy of ^{134}La (1.22 MeV) leads to a worse spatial resolution which can be problematic for preclinical imaging or accurate quantification of small structures.

Another unique feature of this *in vivo* generator system is cerium's easily accessible 4+ oxidation state. The Ce(III)/Ce(IV) redox couple can be leveraged for both purification purposes after production and to allow this system to serve as a theranostic pair for both ^{225}Ac and ^{227}Th[85]. The rest of this section will discuss the production of ^{134}Ce and $^{134}Ce^{III}$/^{134}La as a theranostic matched pair for ^{225}Ac. Section 2.3.2 will discuss $^{134}Ce^{IV}$/^{134}La as a theranostic matched pair for ^{227}Th.

The state-of-the-art production/purification method for producing ^{134}Ce occurs at the Isotope Production Facility at Los Alamos National Laboratory where a natural Lanthanum target is bombarded by a 100 MeV proton beam (99 μA) for 30 hours through a ^{139}La(p,6n)^{134}Ce reaction[85]. The irradiated target is allowed to cool for 6 days, it is then dissolved using 8 M HNO_3. After dissolution, separation of ^{134}Ce from the rest of the lanthanum is achieved through the oxidation of cerium from +3 to +4 using $NaBrO_3$, and Ce^{IV} was separated from La^{III} using anion-exchange chromatography. At 7.8 days after irradiation, the cerium radioisotopes, activity, and half-life were reported as follows: ^{134}Ce (18.3 GBq), ^{137m}Ce (1.6 GBq; $T_{1/2}$=34.4 hours), ^{137}Ce (activity dependent on ^{137m}Ce; $T_{1/2}$=9.0 hours), ^{135}Ce (148.0 MBq; $T_{1/2}$=17.7 hours) and ^{139}Ce (207.2 MBqi; $T_{1/2}$=137.6 days). The high activity of the short-lived impurities necessitates that the ^{134}Ce be allowed to cool before preclinical or clinical studies. By the time shipments of ^{134}Ce reach Lawrence Berkeley National Laboratory, the only

impurity in non-negligible amounts was ^{139}Ce which emits an intense gamma (165.9 keV at an intensity of 80%). This impurity is not ideal from a radiation dose perspective, but it does offer the capability for multimodality PET/SPECT imaging. While the SPECT images which are generated from the ^{139}Ce gamma display the biodistribution of the radiopharmaceutical containing cerium, the PET images which are generated from the ^{134}La's annihilation photons display the distribution of the ^{134}La radionuclides. This can elucidate whether redistribution of ^{134}La and internalization of radiopharmaceuticals are occurring.

Cerium's 3+ ionic radius at 114 pm (at coordination number = 8) allows $^{134}Ce^{III}$ to act as a theranostic matched pair for ^{225}Ac (Fig. 2.3)[56]. Based on an *in vivo* biodistribution study of ^{134}Ce-citrate (citrate complexes dissociate *in vivo* allowing for the determination of the biodistribution of free ^{134}Ce), free ^{134}Ce behaves more like free ^{225}Ac *in vivo* since it uptakes primarily in the liver and the skeletal system (Chapter 3). Using L_3-edge x-ray absorption spectroscopy, it was confirmed that Ce-DTPA is in a 3+ oxidation state[85]. The acute biodistribution and *in vivo* stability were investigated in Swiss Webster mice (an immunocompetent mouse model where the biodistribution of a variety of metal-chelator complexes has been extensively assayed by the Bioactinide Chemistry Group) which confirmed $^{134}Ce^{III}$-DTPA surrogacy to ^{225}Ac-DTPA (Chapter 3)[57]. A similar study also demonstrated ^{134}Ce-DOTA surrogacy to ^{225}Ac-DOTA (Chapter 3). A proof of concept study further showed DOTA's compatibility for ^{134}Ce through an *in vivo* PET imaging study of ^{134}Ce-DOTA-Trastuzumab in SK-OV-3 tumor-bearing NOD SCID mice demonstrating elevated tumor uptake over 9 days and limited skeletal and liver uptake (Chapter 4). Due to the similar sizes of $^{134}Ce^{III}$ and ^{225}Ac, it is also anticipated that other novel chelators such as macropa, Py4pa, Bispa^2, CHXoctapa, and noneunpa will also show an exceptional affinity for $^{134}Ce^{III}$ as well[62–66].

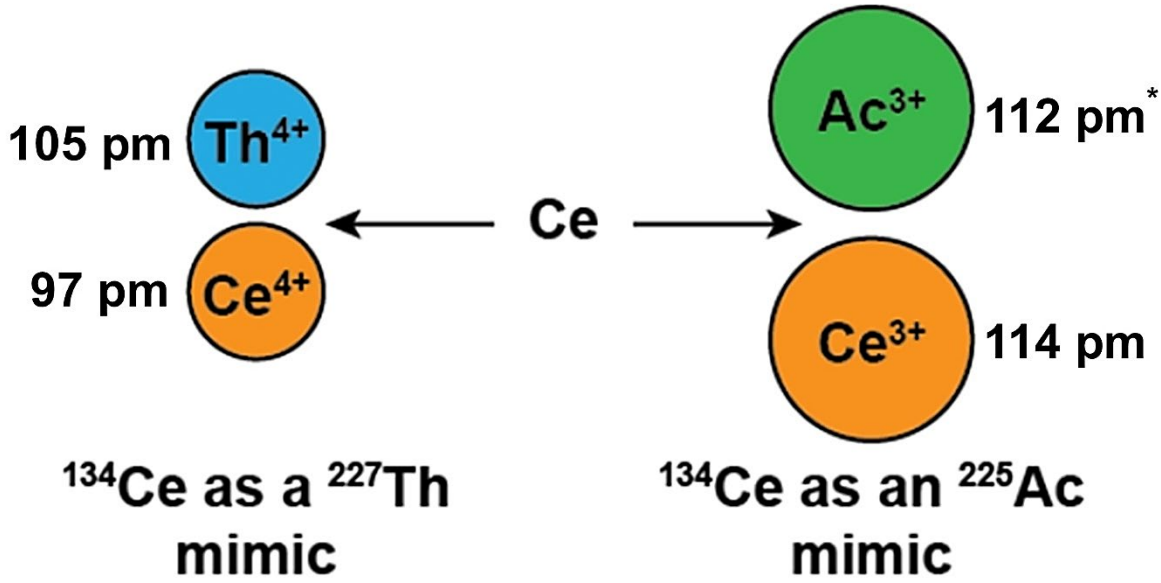

Figure 2.3: A drawing depicting how cerium can have a similar ionic radius to either ^{225}Ac or ^{227}Th based on its oxidation state.
*The only known ionic radius for ^{225}Ac is at coordination number 6[56]. For the chelators discussed in this dissertation, its ionic radius and coordination number are most likely larger.

2.3 Thorium-227 and its theranostic matched pairs

2.3.1 Thorium-227

^{227}Th ($T_{1/2}$=18.7 days) decays via a series of 5 alpha emissions to stable ^{207}Pb (Fig. 2.4). Like other large tetravalent actinides (ionic radius: 105 pm (coordination number = 8)), the vast majority of ^{227}Th accumulates in the bone with limited uptake in the liver[56,58]. Its rather long-lived daughter, ^{223}Ra ($T_{1/2}$=11.4 days), can redistribute to the bone and the small intestine[95–97]. Long term toxicity has not been reported, and the clinical experience with $^{223}RaCl_2$ has shown that ^{223}Ra is well tolerated[3].

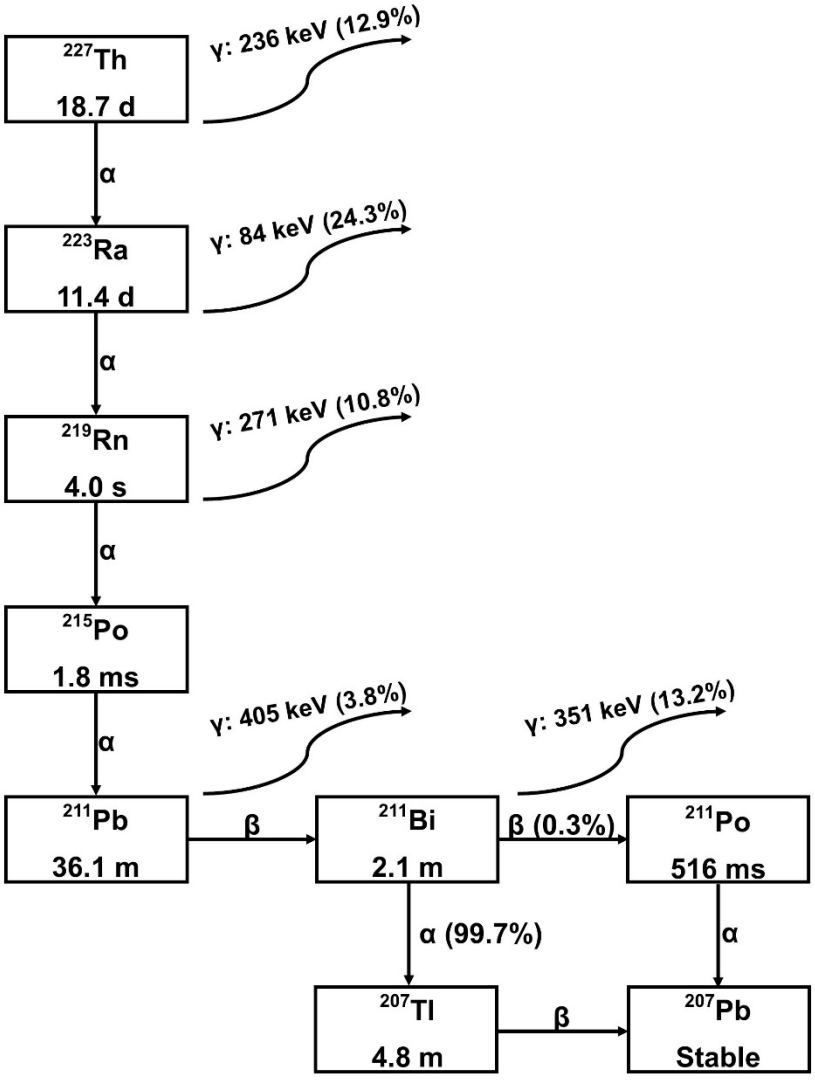

Figure 2.4: ^{227}Th decay chain with the imageable radiation emitted by ^{227}Th and its daughters included. The photons included have the highest intensity for the given isotope.

Both DTPA and DOTA complexes with ^{227}Th have been studied to some extent. While ^{227}Th-DTPA complexes may be effective for labeling rapidly uptaking targeting vectors such as peptides and antibody fragments, ^{227}Th-DTPA will decomplex in the long term due to competition with endogenous divalent cations (similarly to ^{225}Ac-CHX-A" DTPA)[98]. p-SCN-Bn-DOTA was utilized to label ^{227}Th to both trastuzumab and rituximab in a 2-step labeling procedure (labeling the ligand first then conjugating)[99]. The results were lackluster, however, and only led to a radiochemical yield of 6%-17%. While the 1-step labeling procedure improves the yield for DOTA conjugates (70-85%), interest has recently shifted to acyclic, oxygen-rich hydroxypyridinone ligands[68,100]. More specifically, the octadentate bifunctional p-SCN-Bn-(Me-3,2-HOPO) has been shown to have a 96% radiochemical yield with much faster binding kinetics than DOTA-based chelators (30 minutes at room temperature versus 40 minutes to 2 hours at elevated temperatures)[101]. This development has led to *in vitro* and preclinical studies on a variety of antibodies incorporating p-SCN-BN-(Me-3,2-HOPO) and ^{227}Th (aptly termed Targeted Thorium Conjugates)[25].

An advantage of ^{227}Th compared to ^{225}Ac is that it can be produced in clinically relevant amounts[102]. Through the thermal neutron irradiation of ^{226}Ra ($T_{1/2}$ =1600 years) in a reactor, ^{227}Ra ($T_{1/2}$ =42.2 minutes) is produced which β- decays into ^{227}Ac ($T_{1/2}$ =21.8 years). This long-lived isotope (which subsequently β- decays into ^{227}Th) provides the basis for a generator that can produce both ^{227}Th and ^{223}Ra for FDA approved $^{223}RaCl_2$ through anion exchange chromatography (^{227}Th β- decays into ^{223}Ra). This availability of ^{227}Th may help streamline the FDA approval process for Targeted Thorium Conjugates in the future.

Unlike ^{225}Ac, ^{227}Th does directly emit imageable gammas, which allows for assaying the distribution of the radiopharmaceutical incorporating ^{227}Th. Moreover, ^{223}Ra and a few of the shorter-lived daughters also emit some imageable photons. Utilizing different energy windows in a SPECT scanner allows for simultaneous imaging of both the candidate molecule and the redistribution of ^{227}Th's daughters[46,103]. While this has great potential for applying the theranostic approach for ^{227}Th radiopharmaceuticals, current SPECT technology incorporating collimators does not offer enough sensitivity for low activity imaging, leading to low signal-to-noise images. In the future, collimatorless gamma cameras would be groundbreaking for this field[48,49]. However, in the meantime, the codevelopment of theranostic matched pairs of ^{227}Th is warranted in order to facilitate the use of ^{227}Th. Table 2.2 summarizes ^{227}Th and its theranostic matched pairs including half-life, imageable radiation, chelators, and targeting vectors.

Table 2.2: Summary of ^{227}Th and its theranostic matched pairs.

Radionuclide	Half-Life	Ionic Radius[56]	Imageable Radiation[a]	Chelators	Targeting Vectors
^{227}Th	18.7 d	105 pm	^{227}Th: 88 keV (2.2%), 236 keV (12.9%), 256 keV (7.0%) ^{223}Ra: 81 keV (14.7%), 84 keV (24.3%), 95 keV[b] (10.8%)[b], 144 keV (3.5%), 154 keV (6.0%), 270 keV (13.3%), 324 keV (3.6%), 338 keV (2.6%) ^{219}Rn: 271 keV (10.8%), 402 keV (6.6%) ^{211}Pb: 405 keV (3.8%), 832 keV (3.5%) ^{211}Bi: 351 keV (13.2%)	DTPA[98] DOTA[99,100,102] Me-3,2-HOPO[25,68,101,104]	Trastuzumab[99,102] Rituximab[99] CD22[25] CD33[25] MSLN[25] PSMA[25] CD70[25] FGFR2[25]
^{134}Ce^{IV}/^{134}La	3.2 d / 6.5 m	97 pm	^{134}La β+: E(β+)=1.22 MeV (63.6%)	3,4,3-LI(1,2-HOPO)[85,c]	N/A
^{89}Zr	3.3 d	84 pm	β+: E(β+)=396 keV (22.74%)	DFO[105] Me-3,2-HOPO[25,104] 3,4,3-LI(1,2-HOPO)[36,106]	MSLN[104] PSMA[25] Trastuzumab[36]

[a]Imageable radiation from ^{227}Th is taken from Larsson, *et al*[46]. The gamma energies are given in units of keV, and their respective intensities are given in the corresponding parentheses as a percentage.
[b]Weighted mean energy and summed intensity from photons between 94 keV and 98 keV.
[c]Chapter 3

2.3.2 Cerium(IV)-134/Lanthanum-134

As discussed previously, due to the Ce^{III}/Ce^{IV} redox couple, the oxidation state of cerium can be stabilized to 4+ with appropriate chelator selection. When ^{134}Ce is tuned to 4+, it has an ionic radius of 97 pm (coordination number = 8) allowing it to act as a theranostic matched pair for ^{227}Th (Fig. 2.3)[56]. To test this hypothesis, an L_3-edge x-ray absorption spectroscopy measurement was done on Ce-3,4,3-LI(1,2-HOPO), confirming that the chelator stabilizes the oxidation state to 4+[85]. Furthermore, the acute biodistribution and *in vivo* stability were investigated in Swiss Webster mice which confirmed $^{134}Ce^{IV}$-3,4,3-LI(1,2-HOPO) surrogacy to ^{227}Th HOPO-based complexes (Chapter 3). It is currently unclear what the oxidation state of other HOPO-based (such as Me-3,2-HOPO) cerium complexes is, and future work investigating the chemical properties of these complexes is warranted.

2.3.3 Zirconium-89

^{89}Zr ($T_{1/2}$=3.3 days) has several advantages as a PET radioisotope. It can be produced through the $^{89}Y(p,n)^{89}Zr$ with a proton energy of 14 MeV, allowing for local production using a low energy cyclotron[105]. In addition, ^{89}Y has 100% natural abundance which minimizes the cost for targetry. Moreover because of its long half-life and great spatial resolution (its average positron energy is 396 keV), ^{89}Zr has seen widespread clinical and preclinical use in the realm of ImmunoPET, where monoclonal antibodies and other immune agents are labeled with PET isotopes and subsequently administered and imaged for treatment planning. On top of this, ^{89}Zr shares similar chemical properties and *in vivo* behavior to ^{227}Th. For one, ^{89}Zr is a tetravalent cation in physiological conditions and has a similar ionic radius to ^{227}Th (84 pm (coordination number = 8))[56]. In addition, ^{89}Zr-chloride has been shown to accumulate predominantly in the skeleton of healthy, female NIH Swiss mice (an immunocompetent mouse model that is used commonly for general-purpose research), which is similar to ^{227}Th biodistribution[107].

Most radiopharmaceuticals incorporating ^{89}Zr have utilized the hexadentate siderophore desferrioxamine (DFO)[105]. Unfortunately, due to ^{89}Zr preference for octadentate coordination, ^{89}Zr-DFO complexes have the propensity of demetallating in vivo and ^{89}Zr uptakes in the skeleton. This can lead to an unnecessary radiation dose to the radiosensitive bone marrow. Fortunately, like ^{227}Th, HOPO-based ligands have shown great affinity for ^{89}Zr and form complexes with incredibly high in vivo stability, leading to limited uptake of ^{89}Zr in the skeleton that is similar to ^{227}Th[68,101,106]. In particular, a PSMA-targeting monoclonal antibody and a MSLN-targeting monoclonal antibody using p-SCN-BN-(Me-3,2-HOPO) were leveraged to display the surrogacy of ^{227}Th and ^{89}Zr[25,104]. It is anticipated that p-SCN-BN-3,4,3-LI(1,2-HOPO) and other bifunctional variants of 3,4,3-LI(1,2-HOPO) will show great utility with thorium-zirconium theranostics[36].

2.4 Yttrium-90 and yttrium-86

^{90}Y ($T_{1/2}$=2.7 days) and ^{86}Y ($T_{1/2}$=14.7 hours) are a theranostic pair where ^{90}Y can be used for β- therapy (E(β-)=932 keV (100%)) and ^{86}Y can be used for PET imaging (E(β+)=660 keV (31.9%)). This is certainly advantageous compared to theranostic match pairs since both ^{90}Y and ^{86}Y have identical chemical properties. Yttrium, although

technically a trivalent transition metal due to its positioning in the periodic table, is considered a rare earth element due to it having a rather large ionic radius and preference for higher coordination numbers (ionic radius: 102 pm (coordination number = 8))[56]. Because of this chemical similarity and more widespread availability, it can often be used as a testbed for novel chelating strategies designed for *f*-elements. However unlike other trivalent *f*-elements (such as lanthanum, cerium, and actinium), free yttrium accumulates primarily in the kidneys and bones instead of the liver and bones[108].

^{90}Y is widely available from ^{90}Sr ($T_{1/2}$=28.9 years) generators[79]. ^{90}Sr is a ^{235}U fission product available in concentrations 74−740 GBq/L from high-level liquid waste. Because of the long-lived nature of ^{90}Sr and the use of ^{235}U nuclear reactors, ^{90}Y is an attractive therapeutic radiometal for targeting radiopharmaceuticals. In fact, an antibody drug conjugate, ^{90}Y-tiuxetan-Ibritumomab (tiuxetan is a bifunctional version of DTPA with a methyl group and an isothiocyanatobenzyl linker), was approved for radioimmunotherapy of non-Hodgkin lymphomas by the United States FDA in 2002[109]. Because ^{90}Y is a pure β- (it emits no gamma photons), ^{111}In-tiuxeta-Ibritumomab was originally used to determine if any altered biodistribution occurred in a specific patient that may cause unintended organ damage[6]. In 2011, the US FDA declared this procedure no longer necessary since it was determined that the ^{111}In scan had poor discriminating power in determining altered biodistribution[110].

One reason that ^{111}In was used previously as a surrogate of ^{90}Y instead of ^{86}Y is the more limited availability of ^{86}Y. Currently, the most attractive method is through the ^{86}Sr(p,n)^{86}Y reaction using 14 MeV protons from a low energy cyclotron onto a $^{86}SrCO_3$ target[22,79]. The challenging aspect of this production route is the need for a highly enriched ^{86}Sr target (^{86}Sr has only a 9.86% natural abundance) in order to minimize the coproduction of the impurity ^{87m}Y ($T_{1/2}$=13.4 hours) which decays into the long-lived ^{87}Y ($T_{1/2}$=3.3 days). Target enrichment of 95.6%-97% ^{86}Y is required to minimize the ^{87m}Y impurity to less than 3%[22].

The majority of yttrium-based targeting radiopharmaceuticals use either DTPA or DOTA-based chelators. Both of these chelators have shown the capability of labeling yttrium at low concentrations and demonstrate high kinetic inertness against endogenous metals (iron, copper, zinc, and calcium) and serum proetins[111,112]. Because of this, these chelators have been used in a few preclinical experiments demonstrating ^{86}Y/^{90}Y theranostics in a variety of diseased models[113–117]. However, a recent study showed that in a murine model both ^{86}Y-DTPA and ^{86}Y-DOTA releases retained elevated levels of ^{86}Y in the kidneys 48 hours after administration[27]. This suggests the need for the development of chelators with a higher affinity for yttrium. One potential alternative is acyclic chelators with picolinic acid moieties such as octapa[118,119]. While conjugated to Trastuzumab, octapa allowed for rapid (15 minutes), room temperature labeling with ^{90}Y granting a radiochemical yield of >95%. In addition, a 96 hour serum stability showed that ^{90}Y-octapa-Trastuzumab retained more ^{90}Y than ^{90}Y-CHX-A''-Trastuzumab (94.8% versus 87.1%). Another alternative is hydroxypyridinone-based chelators such as 3,4,3-LI(1,2-HOPO). Because of 3,4,3-LI(1,2-HOPO) affinity for trivalent rare earth elements and its capability for rapid, room temperature radiolabeling, an *in vivo* biodistribution was performed to demonstrate the high *in vivo* stability of ^{86}Y-3,4,3-LI(1,2-HOPO) complexes in Swiss Webster mice[120]. This work is discussed in detail in Chapter 3. Furthermore, the biodistribution and tumor control efficacy of ^{90}Y-

3,4,3-LI(1,2-HOPO) complexes non-covalently bound to Siderocalin-Trastuzumab fusion proteins was investigated in SK-OV-3 tumor-bearing NOD SCID mice. This study is discussed in Chapter 6. Table 2.3 summarizes ^{90}Y and ^{86}Y as theranostic pairs including half-life, imageable radiation, chelators, and targeting vectors.

While the ^{86}Y positron energy does not degrade the spatial resolution of PET images as bad as some of the other positron emitters discussed in this Chapter, ^{86}Y emits a myriad of gammas that range from 187.87 keV to 2610.11 keV. While some of these gammas are out of the energy window range of PET scanners (typically 350 keV to 650 keV), the ones that are in the range or the higher energy ones that Compton scatter inside the patient into the range can lead to false coincidences (recorded events that are not actually attributed to a positron annihilation)[22]. These false coincidences can lead to a low frequency background which can overestimate organ uptake. While these false coincidences can be minimized in 2-D mode PET through projection tail fitting, global tail fitting, or longitudinal collimators, there has been no correction mechanism validated for 3-D mode PET[22,121]. This overestimation problem is more apparent in clinical PET however where Compton scattering in a human is more common compared to a small rodent.

Table 2.3: Summary of the theranostic pairs $^{90}Y/^{86}Y$ and $^{212}Pb/^{203}Pb$.

Theranostic Pair	Half-Life	Ionic Radius[5] [6]	Imageable Radiation	Chelators	Targeting Vectors
^{90}Y / ^{86}Y	18.7 d / 14.7 h	102 pm	^{86}Y β+: E(β+)=660 keV (31.9%)	DTPA[6,27,109,110,112–115,117,119] DOTA[27,111,112,116] Octapa[118,119] 3,4,3-LI(1,2-HOPO)[120,a]	Ibritumomab[6,109,110] DOTATOC[111] DOTATATE[111] Trastuzumab[113,119,c] TRC105[114,115] ALT836[117] Ultrasmall Mesoporous Silica Nanoparticles[116]
^{212}Pb / ^{203}Pb	2.2 d / 10.6 m	129 pm	^{203}Pb: 279 keV (81.0%) ^{212}Pb: 239 keV (43.6%), 300 keV (3.3%)	DOTA[122–127] TCMC[122,123,125,128–130,b]	Trastuzumab[128,b] PSMA[122,129,130] CC49[123] PEG4-VMT-MCR1[124] Biotin[126] GGNle-CycMSH$_{hex}$[127]

[a]Chapter 3
[b]Chapter 5
[c]Chapter 6

2.5 Lead-212 and lead-203

The final theranostic pair that will be discussed in this Chapter are ^{212}Pb ($T_{1/2}$ = 10.6 hours) and ^{203}Pb ($T_{1/2}$=2.2 days). ^{212}Pb own low energy β- decay (E(β-)=101.3 keV) is not why this pair is attractive; ^{212}Pb's short-lived daughter, ^{212}Bi ($T_{1/2}$=1.01 hours) decays either by alpha emission (with a 35.9% branching ratio) or it β- decays into ^{212}Po ($T_{1/2}$=300 ns) which decays instantaneously via alpha emission (Fig. 2.5). This allows ^{212}Pb to act as an *in vivo* generator system (like $^{134}Ce/^{134}La$) where ^{212}Pb is labeled to a targeting vector, administered to the patient, and then decays into ^{212}Bi *in vivo* which emits the potent alpha particle[128]. In addition, lead, being a divalent group 4 metal (ionic radius: 129 pm (coordination number = 8)), behaves differently *in vivo* compared to rare

earth elements and actinides discussed in this chapter[56]. Free lead has been shown to uptake in the liver, kidneys, bone, and the brain[23,131].

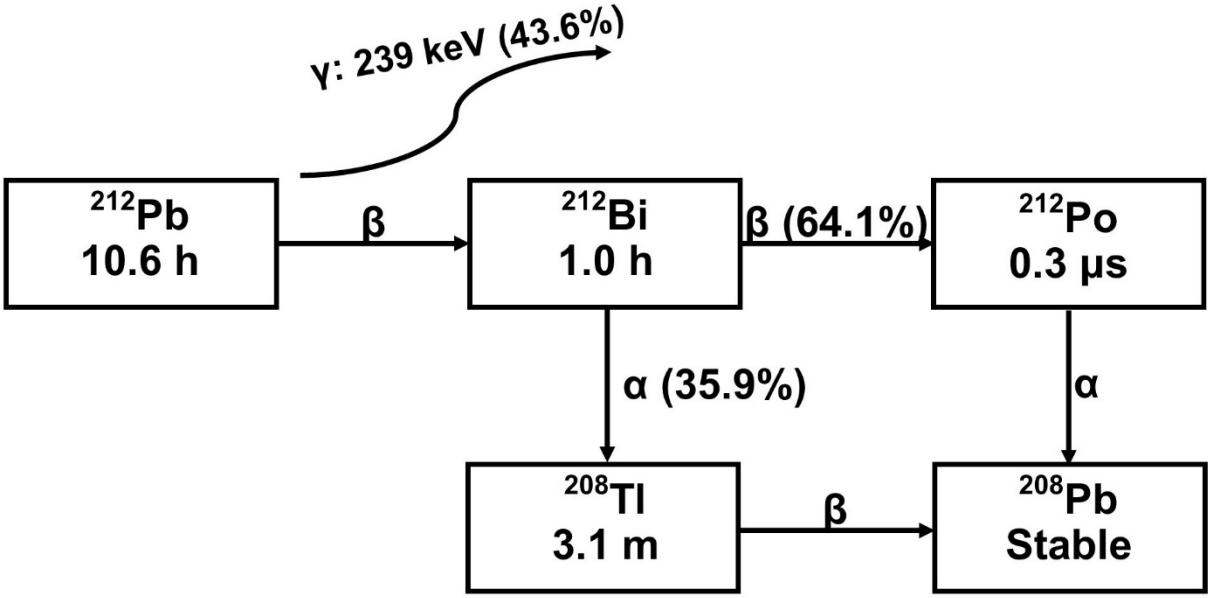

Figure 2.5: ^{212}Pb decay chain with the imageable radiation emitted by ^{212}Pb.The photon included has the highest intensity emitted by ^{212}Pb.

Similarly to ^{227}Th, ^{212}Pb emits gamma photons that could potentially allow for direct SPECT imaging of ^{212}Pb-labeled targeting radiopharmaceuticals[132]. Unfortunately, like ^{225}Ac and ^{227}Th, the activity of administered ^{212}Pb is low compared to typical radionuclides and this can lead to images with low signal-to-noise ratios. Unlike ^{225}Ac and ^{227}Th, the electron capture isotope ^{203}Pb, which can be imaged through SPECT due to the emission of a 279.2 keV (81%) gamma, leads to high quality images for preclinical and clinical lead theranostic studies[23,122,127,129,130].

In the US, ^{212}Pb is generally available through the elution ^{224}Ra/^{212}Pb generators[14]. ^{224}Ra ($T_{1/2}$=3.6 days) is generally separated from its ^{228}Th parent ($T_{1/2}$=1.9 years) which decays and is separated from ^{232}U ($T_{1/2}$=68.9 years) stockpiles[125]. From there, ^{224}Ra is loaded onto a cation exchange column which is either eluted with hydrochloric or hydroiodic acid yielding ^{212}Pb with limited impurities (breakthrough of ^{224}Ra is less than 1 ppm)[128,133]. Unfortunately, this method leads to large volumes of ^{212}Pb in ab unfavorable electrolytic solution which is unideal for radiolabeling. Because of this, the ^{212}Pb solution has to be evaporated down to a residue and then redissolved into a more appropriate electrolytic solution. This is problematic because these steps can add a few more hours to an already time intensive procedure (which leads to a smaller activity of ^{212}Pb from decay and process losses). In Chapter 5, a series of radiolabeling experiments with the goal of benchmarking the elution of these generators with 1.0 M sodium acetate is discussed. This novel elution strategy allows the direct radiolabeling of targeting vectors without the need for evaporation and redissolution.

^{203}Pb can be produced using low energy cyclotrons through the ^{203}Tl(p,n)^{203}Pb reaction using protons on a natural thallium target[23]. The target is then dissolved and pushed through either an anion exchange column or a Pb-selective column[124].

Afterwards, either nitric acid or hydrochloric acid is pushed through to remove the ^{203}Pb from the column. This process leads to a very pure solution of ^{203}Pb where no radio-impurities were detected through gamma spectroscopy[23].

Early studies evaluated DOTA as a potential chelator of lead isotopes. In a SW122 tumor-bearing murine model, the biodistribution ^{212}Pb-DOTA-biotin and ^{203}Pb-DOTA-biotin were compared[126]. ^{203}Pb and ^{212}Pb had similar biodistributions in all organs besides the kidney, spleen, and femur. The kidneys in particular had an excess amount of ^{212}Bi which primarily may be from the recoil effect where the alpha emission from ^{212}Pb causes ^{212}Bi to recoil and release from its chelator, resulting in the redistribution to the kidneys. The excess femur uptake is particularly from the *in vivo* release of ^{212}Pb from the chelator which can redistribute to the bone. The macrocyclic TCMC was found to be more stable *in vivo* and led to ^{212}Pb-TCMC-Trastuzumab being the first lead-based targeted radiopharmaceutical to be administered in humans with no toxicity noted up to 1 year[123,125,134,135]. TCMC has continued to be touted as the gold standard of lead theranostics and has demonstrated to have superior radiolabeling yield and higher *in vivo* stability with both ^{212}Pb and ^{203}Pb than DOTA in PSMA models as well[122]. Table 2.3 summarizes ^{212}Pb and ^{203}Pb as theranostic pairs including half-life, imageable radiation, chelators, and targeting vectors.

2.6 Conclusion

For targeted radionuclide therapy, no single therapeutic radionuclide is the best choice for every situation. While ^{225}Ac and ^{227}Th with their long series of alpha emissions have shown promising preclinical and clinical results for metastatic cancers and small tumor volumes, they both suffer from a lack of theranostic pairs and require the development of chemically similar theranostic matched pairs in order to perform accurate dosimetry and treatment planning[11,25]. In addition, if not handled correctly, the recoiling daughters can lead to radiotoxicity and potentially second cancers[26]. Moreover, the lack of fundamental understanding of actinium has made the development of effective chelators rather challenging, and the lack of availability of ^{225}Ac has inhibited its development in targeting radiopharmaceuticals[69,136].

^{212}Pb is another alpha emitter that solves a lot of problems that ^{225}Ac and ^{227}Th pose. For instance, ^{212}Pb has a theranostic pair, ^{203}Pb, that can be imaged via SPECT[130]. In addition, ^{212}Pb is available in ^{224}Ra/^{212}Pb generators which are rather convenient for hospitals as they act as a self-renewing source of ^{212}Pb for a couple weeks[128]. The main disadvantage of ^{212}Pb is the current elution strategy (which involves time consuming evaporation and redissolution steps) is rather time consuming which can lead to the loss of activity due to the processes that are involved and to decay. The development of methodologies that can shorten this elution time can greatly facilitate the development of targeting radiopharmaceuticals incorporating ^{212}Pb.

Finally, ^{90}Y is a tried and true therapeutic radionuclide with experience in FDA-approved drugs unlike the other therapeutic radionuclides discussed in this chapter[109]. While not as effective against smaller tumor volumes and metastatic cancers as alpha emitters, beta emitters such as ^{90}Y are rather effective at larger tumor volumes. In addition, ^{90}Y is much easier to control *in vivo* since it lacks recoiling radioactive daughters unlike ^{225}Ac, ^{227}Th, and ^{212}Pb. Furthermore, the use of ^{86}Y as a theranostic

pair can allow for accurate dosimetry and treatment planning of yttrium-based targeted radiopharamceuticals[22].

CHAPTER 3: Investigating the *in vivo* stability of novel complexes using positron emission tomography

3.1 Introduction

Targeted radiopharmaceuticals are an advantageous weapon against cancer because it allows for the systematic treatment of the disease without having to know the exact location of the diseased tissue (unlike in external beam therapy); only the tumor biology needs to be known (which dictates the specific targeting vector that needs to be used)[137]. This therapy is rather versatile where for a specific targeting vector the payload can be swapped to fit the needs of the patient. For larger tumor volumes, a β-emitter can be used while for smaller tumor volumes, an α-emitter can be used. ^{90}Y, a β- emitter that has been FDA approved as an antibody drug conjugate (^{90}Y-tiuxetan-Ibritumomab) for approximately 2 decades, and ^{225}Ac and ^{227}Th, both of which have recently demonstrated astonishing preclinical and clinical results due to their long decay series which results in a series of α emissions, are all attractive candidates[11,25,109]. The theranostic approach can improve this therapy by using a molecular imaging modality (such as PET or SPECT imaging) to do treatment planning and dosimetry. While it is ideal for the diagnostic radionuclide to be either the same isotope or the same element (like the ^{90}Y/^{86}Y theranostic pair) as the therapeutic radionuclide, some radionuclides (like ^{225}Ac and ^{227}Th) don't have a suitable theranostic pair nor emit enough photons to yield high quality SPECT images with the typical administered activity for alpha emitters. It has been hypothesized that the ^{134}Ce/^{134}La *in vivo* generator system can act as a chemically analogous companion diagnostic for both ^{225}Ac and ^{227}Th.

In addition, it has recently been reported that DOTA and DTPA (both commonly used chelators in targeted radiopharmaceuticals incorporating ^{90}Y and ^{86}Y) lead to the release of yttrium *in vivo*[27,114–117]. This release could potentially lead to the unnecessary dosing of healthy organs and potentially lead to radiotoxicity and second cancers[26,138]. Developing chelators that form complexes with high kinetic inertness is imperative in ensuring the safety and efficacy of these targeted radiopharmaceuticals.

Herein, the *in vivo* stability of novel ^{134}Ce (a potential theranostic matched pair for ^{225}Ac and ^{227}Th) complexes and the novel ^{86}Y-3,4,3-LI(1,2-HOPO) complex are investigated. Some of the data and methods in this Chapter have been previously published in peer-reviewed journals with the permission of all authors. All of the figures have been altered from how they were published for stylistic purposes.

Relevant Publications:

Bailey TA, Mocko V, Shield KM, et al. Developing the 134Ce and 134La pair as companion positron emission tomography diagnostic isotopes for 225Ac and 227Th radiotherapeutics. *Nat Chem.* 2021;13(3):284-289. doi:10.1038/s41557-020-00598-7

Carter KP, Deblonde GJP, Lohrey TD, **Bailey TA**, An DD, Shield KM, Lukens Jr. WW, and Abergel RJ. Developing scandium and yttrium coordination chemistry to advance theranostic radiopharmaceuticals. *Commun Chem.* 2020;3(1):1-7. doi:10.1038/s42004-020-0307-0

3.1.1 ^{134}Ce as a theranostic matched pair for ^{225}Ac and ^{227}Th

For ^{225}Ac (ionic radius: 112 pm (coordination number = 6)), the PET radiometal, ^{68}Ga (ionic radius: 62 pm (coordination number = 6) and the SPECT radiometal, ^{111}In (ionic radius: 92 pm (coordination number = 8), have commonly been used as theranostic matched pairs; while for ^{227}Th (ionic radius: 105 pm (coordination number = 8), the PET radiometal, ^{89}Zr (ionic radius: 84 pm (coordination number =8), has commonly been used as a theranostic matched pair[11,25,38,56,74–77,104]. These main group and transition diagnostic radionuclides poorly represent the chemical properties of ^{225}Ac and ^{227}Th (being actinides) due to having much smaller ionic radii which leads to vast differences in the *in vivo* biodistribution.

The ^{134}Ce ($T_{1/2}$=3.2 days) / ^{134}La ($T_{1/2}$=6.5 minutes) *in vivo* generator system (where the longer-lived ^{134}Ce is labeled to a targeting vector and then decays to ^{134}La *in vivo* which can then be imaged by PET) is in a unique position due to the Ce^{III}/Ce^{IV} redox couple. When its oxidation state is stabilized to 3+ with appropriate chelator selection, $^{134}Ce^{III}$ (ionic radius: 114 pm (coordination number = 8)) can mimic $^{225}Ac^{III}$ due to similar ionic radii[56]. When its oxidation state is stabilized to 4+ with appropriate chelator selection, $^{134}Ce^{IV}$ (ionic radius: 97 pm (coordination number = 8)) can mimic $^{227}Th^{IV}$ due to similar ionic radii[56]. This allows ^{134}Ce to serve as a companion diagnostic for targeted radiopharmaceuticals incorporating either ^{225}Ac or ^{227}Th.

Before incorporating ^{134}Ce into targeted radiopharmaceuticals, investigating its compatibility and *in vivo* stability with commonly used chelators for ^{225}Ac and ^{227}Th is paramount. Both DTPA and DOTA have been used with ^{225}Ac (with DOTA being the most commonly used chelator for ^{225}Ac) while the hydroxypyridinone-based chelators have become a mainstay in Targeted Thorium Conjugated (particularly Me-3,2-HOPO). Herein, the $^{134}Ce^{III}$-DTPA and $^{134}Ce^{III}$-DOTA complexes are investigated as surrogates of $^{225}Ac^{III}$-DTPA and $^{225}Ac^{III}$-DOTA while the $^{134}Ce^{IV}$-3,4,3-LI(1,2-HOPO) (another hydroxypyridinone-based chelator) complex is investigated as a surrogate of $^{227}Th^{IV}$-3,4,3-LI(1,2-HOPO). The radiochemical yield through radio-instant thin layer chromatography (see Appendix A) and the *in vivo* stability through microPET imaging are determined for all three complexes. In addition, an *ex vivo* biodistribution experiment was performed for both the $^{134}Ce^{III}$-DTPA and $^{134}Ce^{IV}$-3,4,3-LI(1,2-HOPO) complexes.

3.1.2 *In vivo* stability of ^{86}Y-3,4,3-LI(1,2-HOPO)

Despite the frequent use of DTPA and DOTA in targeted radiopharmaceuticals incorporating ^{90}Y and ^{86}Y (and other radionuclides), both of these chelators have a number of limitations. DOTA in particular has poor binding kinetics which requires the need for incubating at elevated temperatures for long period of time which is disadvantageous for short-lived radionuclides and labeling antibodies[111]. While the acyclic DTPA allows for faster binding kinetics, DTPA complexes often suffer from low *in vivo* stability when complexed to radionuclides of interest[27,57].

An ideal chelator in targeted radiopharmaceuticals would allow for fast, room temperature binding and high *in vivo* stability. Chelators with hydroxypyridinone moieties are known to meet these criteria[67,68]. 3,4,3-LI(1,2-HOPO) (referred to as HOPO from now on) is a particularly attractive option as it is known to form highly stable complexes with a variety of trivalent and tetravalent metals, including rare earth elements and the actinides[139,140]. Furthermore, density functional theory calculations

have shown structural deformities for HOPO complexes with endogenous metals, which minimizes *in vivo* competition with radiometals of interest[141]. Applied to $^{90}Y/^{86}Y$, this could potentially negate the release of these radiometals *in vivo.* Herein, the *in vivo* stability of ^{86}Y-HOPO in a murine model is investigated through microPET imaging.

3.2 Materials and methods

All procedures and protocols used in these studies were reviewed and approved by the Institutional Animal Care and Use Committee of LBNL and were performed in AAALAC-accredited facilities, according to prescribed guidelines and regulations. Intravenous injections into a warmed lateral tail vein and euthanasia by cervical dislocation were performed under isoflurane anesthesia.

3.2.1 Materials

The following chemicals were used as received from chemical suppliers: Yttrium-86 (^{86}Y; Eckert & Ziegler), 1,4,7,10-tetraazacylododecane tetraacetic acid (DOTA; Macrocyclics), Diethylenetriaminepentaacetic acid (DTPA; Sigma Aldrich), 3,4,3-LI(1,2-HOPO) (HOPO; Ash Stevens), sodium citrate dihydrate (citrate; Mallinckrodt), 10x sterile phosphate buffered saline (10X PBS, VWR), ammonium acetate (NH_4OAc; Fluka), 0.9% sterile saline (saline; APP Pharmaceuticals), Ethylenediaminetetraacetic acid disodium salt dihydrate (EDTA; VWR), Dimethyl sulfoxide (DMSO; Amresco). All solutions were prepared with deionized water purified by a Millipore Milli-Q water purification system.

3.2.2 ^{134}Ce production and radiolabeling

^{134}Ce was produced at the Isotope Production Facility (IPF) of Los Alamos National Laboratory (LANL)[85]. In brief, ^{134}Ce was obtained through a $^{139}La(p,6n)^{134}Ce$ reaction by the 100 MeV proton bombardment of a natural lanthanum target. After dissolving the target, separation of ^{134}Ce from the rest of the lanthanum was achieved through the oxidation of Ce from +3 to +4 using $NaBrO_3$, and Ce^{IV} was separated from La^{III} using anion-exchange chromatography. At 7.8 days after end of irradiation, the purified product contained 18.3 GBq of ^{134}Ce ($T_{1/2}$ = 3.16 days), 1.59 GBq of ^{137m}Ce ($T_{1/2}$ = 34.4 hours), 148 MBq of ^{135}Ce ($T_{1/2}$ = 17.7 hours), and 207.2 MBq of ^{139}Ce ($T_{1/2}$ = 137.6 days). 370 MBq samples of ^{134}Ce were then shipped to Lawrence Berkeley National Laboratory with a specific activity ranging from 16.4 kBq/ng (activity of ^{134}Ce to the total mass of cerium) to 96.2 of ^{134}Ce kBq/ng.

The ^{134}Ce-DOTA solution was prepared by adding DOTA to ^{134}Ce (25:1 chelator to cerium nuclide molar ratio) in 0.165 M NH_4OAc, followed by an incubation period of 60 min at 60°C. This ^{134}Ce- DOTA solution was then diluted into saline for animal injection. The ^{134}Ce-citrate solution was prepared by the addition of ^{134}Ce to a solution of 0.008 M citrate and 0.14 M NaCl in MilliQ water.

For labeling HOPO and DTPA for live-animal microPET imaging, aliquots of ^{134}Ce in a 0.05 N HCl solution were added to pre-prepared 10X PBS solutions containing either HOPO or DTPA to form solutions with a 25:1 chelator to cerium nuclides molar ratio. Both solutions were incubated at 60 °C for 1 hour and then diluted with saline for animal injection.

For labeling HOPO and DTPA for postmortem microPET imaging and *ex vivo* biodistribution, aliquots of ^{134}Ce in a 0.05 N HCl solution were added to pre-prepared 10X PBS solutions containing either HOPO or DTPA to form solutions with a 10,000:1 chelator to ^{134}Ce ratio (this ratio is approximately on the same order of magnitude to the 25:1 ligand to cerium nuclides ratio that was used for the live animal microPET imaging solutions). Both solutions were incubated at 45 °C for 2 hours and then diluted with saline for animal injection.

Activities of the ^{134}Ce-DOTA, ^{134}Ce-citrate, live-animal ^{134}Ce-HOPO, and live-animal ^{134}Ce-DTPA injection solutions were determined by gamma spectroscopy via a P-Type High Purity Germanium gamma spectrometer using the 511.00 and 604.72 keV lines of ^{134}La. Activities of the postmortem ^{134}Ce-HOPO and postmortem ^{134}Ce-DTPA injection solutions were measured by Liquid Scintillation Counting (Packard Tri-Carb model B4430, Perkin Elmer), using a 20 – 2000 keV window and Ultima Gold LLT. For both methods, samples were allowed to sit at rest for more than 1 hour prior to measurements to allow ^{134}La to reach secular equilibrium with ^{134}Ce before counting, allowing the ^{134}La activity to be equivalent to ^{134}Ce. The radiochemical yields of these radiolabeled small molecule solutions were determined by radio-instant thin layer chromatography (Bioscan System 200 Imaging Scanner), using Varian ITLC-SA strips (Agilent Technologies) and 50 mM EDTA at pH 10.5 as the mobile phase. Radiochemical yields were determined by drawing two regions of interest (using Bioscan System 200 Imaging Scanner software) over the prominent gaussian peak (which contains the labeled chelators) and the region to the left of the prominent peak (which constitutes unlabeled radiometal). The radiochemical purity is then calculated by the ratio of labeled radiometal to the total amount of radiometal on the plate.

3.2.3 ^{86}Y radiolabeling

A 2.86 mL 10X PBS solution containing 5 µL of HOPO (34.9 µM) in DMSO was added to the ^{86}Y stock solution in 0.1 M HCl in order to form a 10,000 to 1 ligand to ^{86}Y ratio. The reaction was incubated at room temperature for 10 minutes. In order to confirm ^{86}Y-HOPO binding, an aliquot of the solution was combined with a wild-type Siderocalin protein solution, and upon Siderocalin recognition, separation from free ^{86}Y was done via spin filtration using 0.5 mL 10 kDa Amicon Ultra centrifugal filter units (see Chapter 6 for a discussion on Siderocalin proteins)[142]. Free ^{86}Y goes through the filter, and a Ludlum 2224-1 Alpha-Beta Scaler-Ratemeter was used to determine the proportion of activity that remained in the filter versus the activity that went through the filter. The solution was then diluted with saline for animal injection. The activity of the solution was determined by gamma spectroscopy via a P-Type High Purity Germanium gamma spectrometer using the 307.00, 443.13, 580.57, and 777.37 keV lines of ^{86}Y.

3.2.4 Live animal ^{134}Ce PET imaging and *in vivo* biodistribution

Biodistribution studies were performed to evaluate the *in vivo* stability of ^{134}Ce-DOTA, ^{134}Ce-HOPO, and ^{134}Ce-DTPA in adult female Swiss Webster mice (12-19 weeks; 31.9 ± 2.8 g; Simonsen Laboratories, CA). ^{134}Ce-citrate was also administered since it would be representative of free ^{134}Ce *in vivo.* Groups of four mice were injected intravenously with a single 0.2 mL dose of either ^{134}Ce-DOTA (6.90 ± 0.03 MBq, 22.6 nM), ^{134}Ce-HOPO (4.49 ± 0.02 MBq, 14.7 nM), ^{134}Ce-DTPA (7.72 ± 0.03 MBq, 25.3

nM), or ^{134}Ce-citrate (5.05 ± 0.02 MBq, 16.5 nM). Molarities of the ligands and the metals in each injection dose are included in Table 3.1. The mice were anesthetized at 20 minutes, 5 hours, and 25 hours and subsequently imaged with a Concorde microPET R4 in the head first prone position. After the 25 hour timepoint, mice were euthanized by cervical dislocation.

3.2.5 *Ex vivo* biodistribution and postmortem ^{134}Ce PET imaging

A separate *ex vivo* biodistribution study was also performed to evaluate the *in vivo* stability of ^{134}Ce-HOPO and ^{134}Ce-DTPA in adult female Swiss Webster mice (14-15 weeks old; 32.4 ± 1.6 g; Simonsen Laboratories, CA). Groups of three mice were injected intravenously with a single 0.2 mL dose of either ^{134}Ce-HOPO (3.19 ± 0.01 MBq, 10.4 nM) or ^{134}Ce-DTPA (6.27 ± 0.01 MBq, 20.5 nM). Molarities of the ligands and the metals in each injection dose are included in Table 3.1. Each group was euthanized by cervical dislocation at 10 minutes, 4 hours, and 24 hours after injection. After at least 1 hour after euthanasia (to ensure ^{134}Ce and ^{134}La are in secular equilibrium), the euthanized mice were subsequently imaged with a Concorde MicroPET R4 in the head first supine position. For each mouse, the liver, kidneys, spleen, lungs, and the abdominal remaining tissue (ART, which includes the (GI) tract, reproductive organs, urinary bladder, and abdominal fat) were dissected and counted by a gamma counter (Packard A5530 gamma spectrometer) with the results being reported in terms of percent recovered activity per gram of tissue (%RA/g).

3.2.6 Live animal ^{86}Y PET imaging and *in vivo* biodistribution

Biodistribution studies were performed to evaluate the *in vivo* stability of ^{86}Y-HOPO in adult female Swiss Webster mice (11-12 weeks; 32.6 ± 1.5 g; Simonsen Laboratories, CA). Groups of three mice were injected intravenously with a single 0.2 mL dose of ^{86}Y-HOPO (3.44 ± 0.11 MBq, 2.18 nM). Molarities of the ligands and the metals in each injection dose are included in Table 3.1. The mice were anesthetized at 15 minutes, 2 hours, 24 hours, and 48 hours after injection on a Concorde microPET R4 in the head first prone position. After the 48 hour timepoint, mice were euthanized by cervical dislocation.

Table 3.1: Ligand molarity, radiometal molarity, and ligand to radiometal ratio for every complex injection dose discussed in Chapter 3.

Complexes[a]	Ligand Molarity	Radiometal Molarity	Ligand to radiometal ratio
^{134}Ce-DOTA	241.0 μM	22.6 nM	10,664
^{134}Ce-HOPO premortem	255.0 μM	14.7 nM	17,347
^{134}Ce-DTPA premortem	439.0 μM	25.3 nM	17,352
^{134}Ce-citrate	8.0 mM	16.5 nM	484,484
^{134}Ce-HOPO postmortem	104.0 μM	10.4 nM	10,000
^{134}Ce-DTPA postmortem	205.0 μM	20.5 nM	10,000
^{86}Y-HOPO	21.8 μM	2.18 nM	10,000

[a]Injection dose was 0.2 mL injected intravenously for all complexes

3.2.7 MicroPET scanner and reconstruction parameters

The Concorde microPET R4 supports a transaxial resolution of 1.66 mm FWHM, an energy window of 350-650 keV, and a coincidence timing window of 6 ns were used during image acquisition. Images were reconstructed using 3D ordered subset expectation maximum followed by maximum a posteriori onto a 128 x 128 x 63 (0.85 x 0.85 x 1.2 mm^3) matrix. Image data underwent normalization, dead-time count losses, positron branching ratio, and decay corrections. The counting rates in the processed images were converted to the percentage of injected activity per gram of tissue (%IA/g) using a system calibration factor obtained by imaging a cylinder filled with a known concentration and volume of the injection solutions. The reported images are coronal maximum intensity projection (MIP) images. Quantitative imaging analysis on organs of interest was done by hand-drawing three-dimensional regions of interest (ROI) using AMIDE v1.0.5 with the results being reported in terms of percent injected activity per gram of tissue (%IA/g)[143].

3.3 Results

3.3.1 ^{134}Ce *in vivo* stability

Figure 3.1 shows representative coronal (MIP) PET images of ^{134}Ce-citrate biodistribution through 25 h in healthy female Swiss Webster mice. All three timepoints display high uptake in both the liver and the skeletal system (the knee bones are used as a surrogate for the skeletal system reference, for ROI purposes) (Fig. 6A). The liver uptake was initially high (18.18 ± 2.08 %IA/g at 20 minutes) and then increased and plateaued at the two latter timepoints (30.04 ± 2.54 %IA/g at 5 hours and 29.87 ±1.75 %IA/g at 25 hours). Isotope burden in the knee bones gradually increased over time from 1.54 +/- 0.54 %IA/g at 20 minutes to 2.54 ± 0.49 %IA/g at 25 hours. Minimal uptake was apparent in the rest of the mice besides minute accumulation in the bladder at 20 minutes indicating a minor renal elimination pathway.

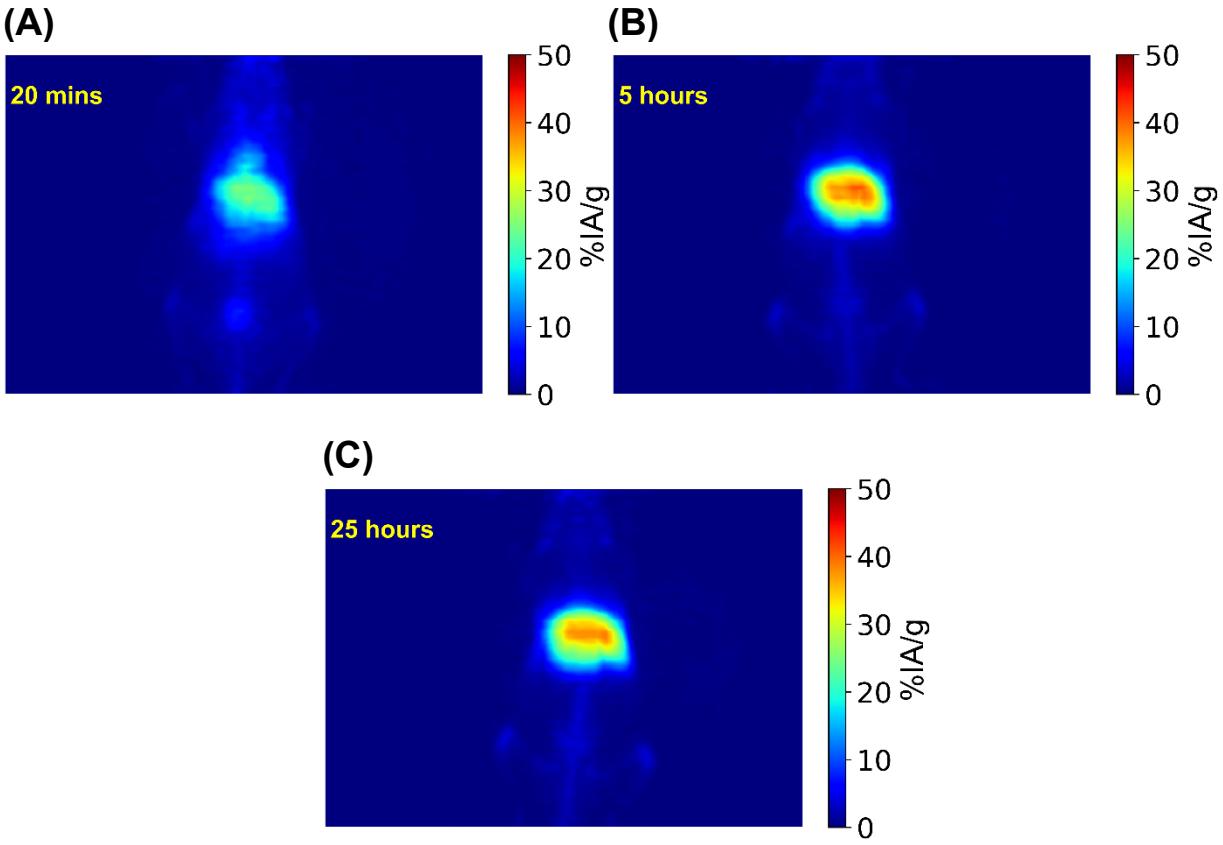

Figure 3.1: Maximum intensity projection (MIP) PET images of a Swiss Webster mouse injected intravenously with 5.05 MBq of ^{134}Ce-citrate at (a) 20 minutes, (b) 5 hours, and (c) 25 hours after administration.

Radio-instant thin layer chromatography (radio-ITLC) allows for the separation of unlabeled or "free" ^{134}Ce from labeled ^{134}Ce. This proportion of labeled to unlabeled ^{134}Ce is then quantified through the use of a position-sensitive proportional counter. When the ^{134}Ce solution is spotted at the origin of the silica gel plate (the stationary phase), free ^{134}Ce is complexed by the EDTA in the mobile phase (50 mM of EDTA at pH 10.5). Through these investigations, it was discovered that the ^{134}Ce-EDTA complex moved much further up the plate than the experimental ^{134}Ce complexes (DOTA, HOPO, and DTPA) since ^{134}Ce-EDTA has a much higher polarity than the other complexes.

^{134}Ce-DOTA exhibited a high radiochemical yield (93.9%) measured by radio-ITLC where free ^{134}Ce moved up the plate with the solvent front while the prominent ^{134}Ce-DOTA peak lagged behind the solvent front (Fig. 3.2A and 3.2B). This high stability was also apparent *in vivo* with the majority of activity located in the bladder at 20 minutes, which indicates rapid renal elimination (Fig. 3.3). High *in vivo* stability is further demonstrated by virtually all activity being eliminated by 5 hours (notice the low signal to noise of the 5 hours and 25 hours images), no apparent bone uptake, and minimal liver and kidney uptake at 25 hours (Fig. 3.6B). Both liver and kidney uptakes decreased rapidly between 20 minutes and 5 hours, with liver uptake reduced from 2.65 ± 0.47 %IA/g to 0.04 ± 0.01 %IA/g and kidney uptake from 1.49 ± 0.42 to 0.20 ± 0.03 %IA/g.

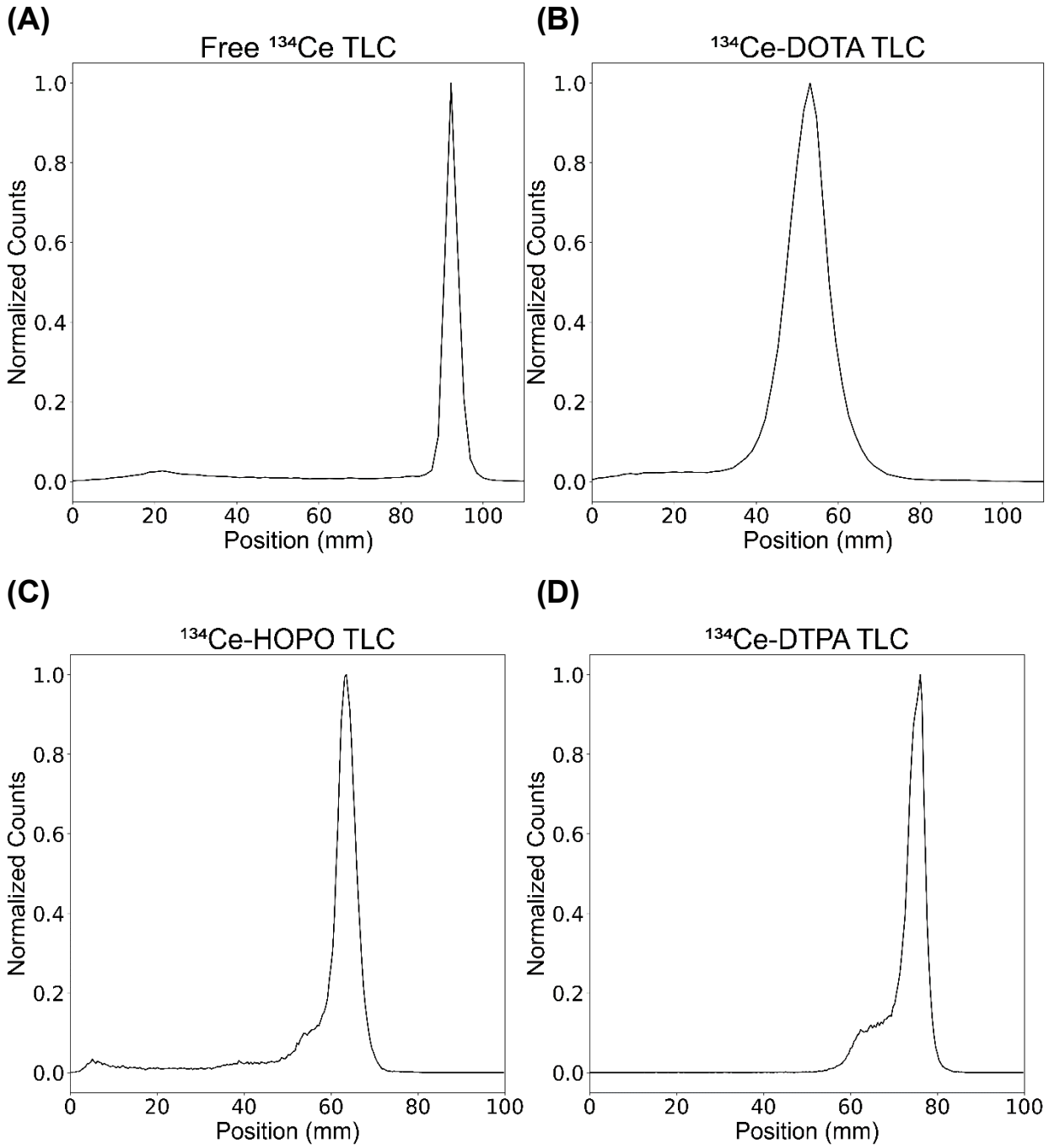

Figure 3.2: Radio-ITLC traces of (A) free ^{134}Ce, (B) ^{134}Ce-DOTA, (C) ^{134}Ce-HOPO, and (D) ^{134}Ce-DTPA. The origin is located at 0 mm. For the experimental complexes, counts outside the prominent peak correspond to unlabeled ^{134}Ce.

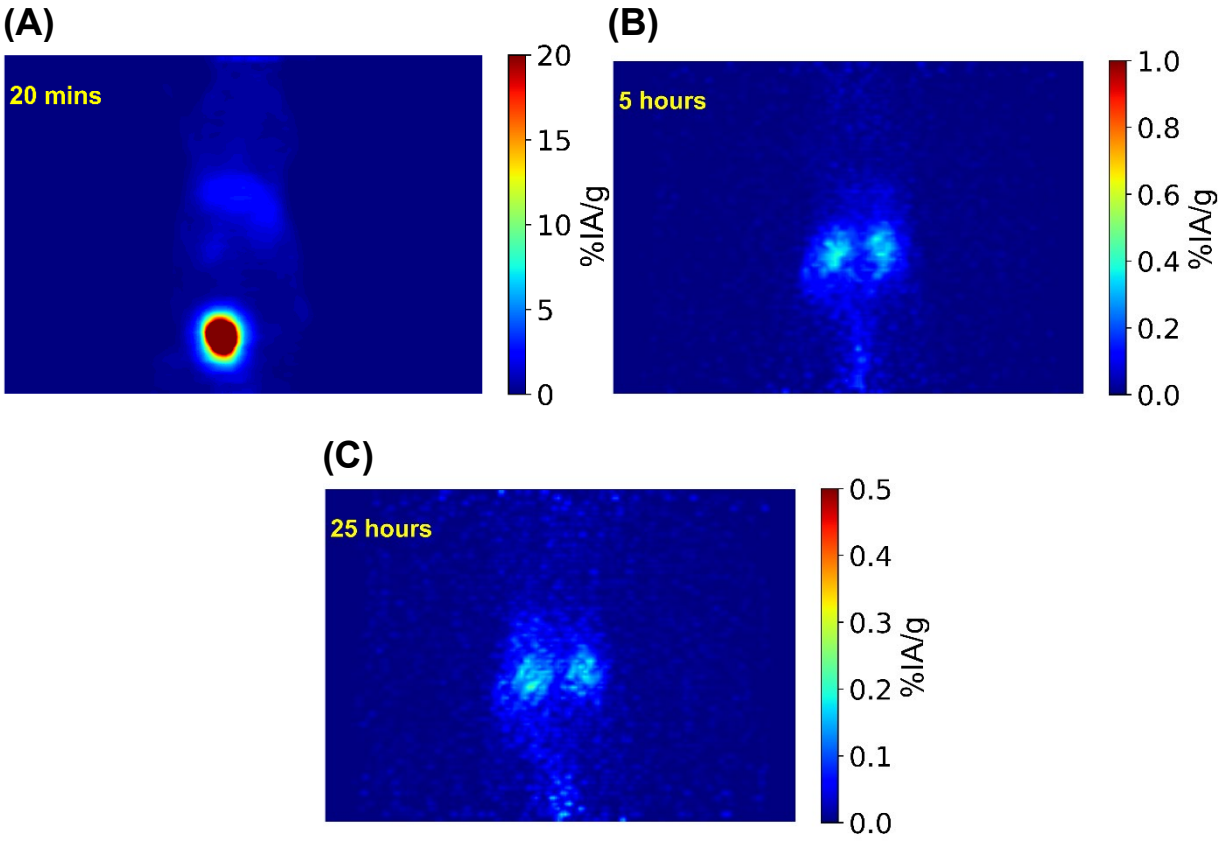

Figure 3.3: MIP PET images of a Swiss Webster mouse injected intravenously with 6.90 MBq of ^{134}Ce-DOTA at (a) 20 minutes, (b) 5 hours, and (c) 25 hours after administration. At 20 minutes, the majority of activity is located in the bladder indicating rapid, renal elimination of ^{134}Ce-DOTA.

^{134}Ce-HOPO displayed a radiochemical yield (83.6%) measured by radio-ITLC where the prominent ^{134}Ce-HOPO lagged behind the solvent front (Fig. 3.2C). ^{134}Ce-HOPO is unique compared to all of the cerium complexes discussed in this chapter because it is eliminated through the hepatobiliary pathway as shown in figure 3.4. At 20 minutes and 5 hours, activity is shown accumulated in the liver and traversing the gastrointestinal tract. At 25 hours, minimal activity remains in the liver and the abdominal remaining tissue (notice the high signal-to-noise in Fig. 3.4C) with no apparent bone uptake indicating high *in vivo* stability. Due to the slower nature of the hepatobiliary pathway in comparison to the renal pathway, the initial liver and abdominal remaining tissue start out high (liver is 3.92 ± 0.69 %IA/g and ART is 60.37 ± 7.44 at 20 minutes) but decrease to minimal levels by 25 hours (liver is 0.31 ± 0.05 %IA/g and ART is 0.40 ± 0.11 %IA/g at 25 hours) (Fig. 3.6C).

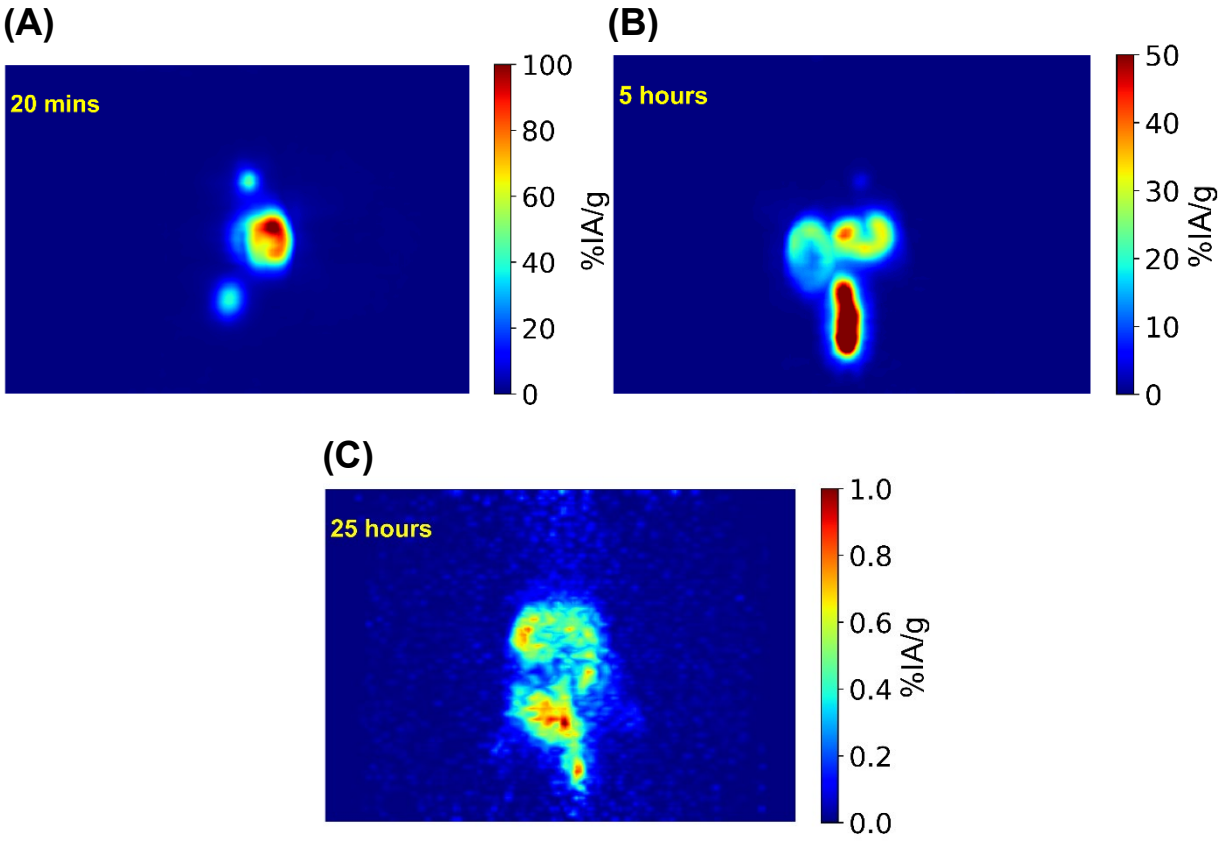

Figure 3.4: MIP PET images of a Swiss Webster mouse injected intravenously with 4.49 MBq of ^{134}Ce-HOPO at (a) 20 minutes, (b) 5 hours, and (c) 25 hours after administration. At 5 hours, the high concentration of activity is located in the gastrointestinal tract indicating hepatobiliary elimination of ^{134}Ce-HOPO.

^{134}Ce-DTPA displayed a radiochemical yield (83%) measured by radio-ITLC where the prominent ^{134}Ce-DTPA peak lagged behind the solvent front. Like ^{134}Ce-DOTA, ^{134}Ce-DTPA is eliminated through the rapid renal pathway with the majority of activity located in the bladder at 20 minutes. High *in vivo* stability is confirmed at 5 hours and 25 hours with minimal activity located in the kidneys (0.31 ± 0.24 %IA/g at 5 hours and 0.29 ± 0.05 at 25 hours) and liver (0.49 ± 0.30 %IA/g at 5 hours and 0.25 ± 0.03 %IA/g at 25 hours) and no apparent uptake in the knee bones (Fig. 3.6D).

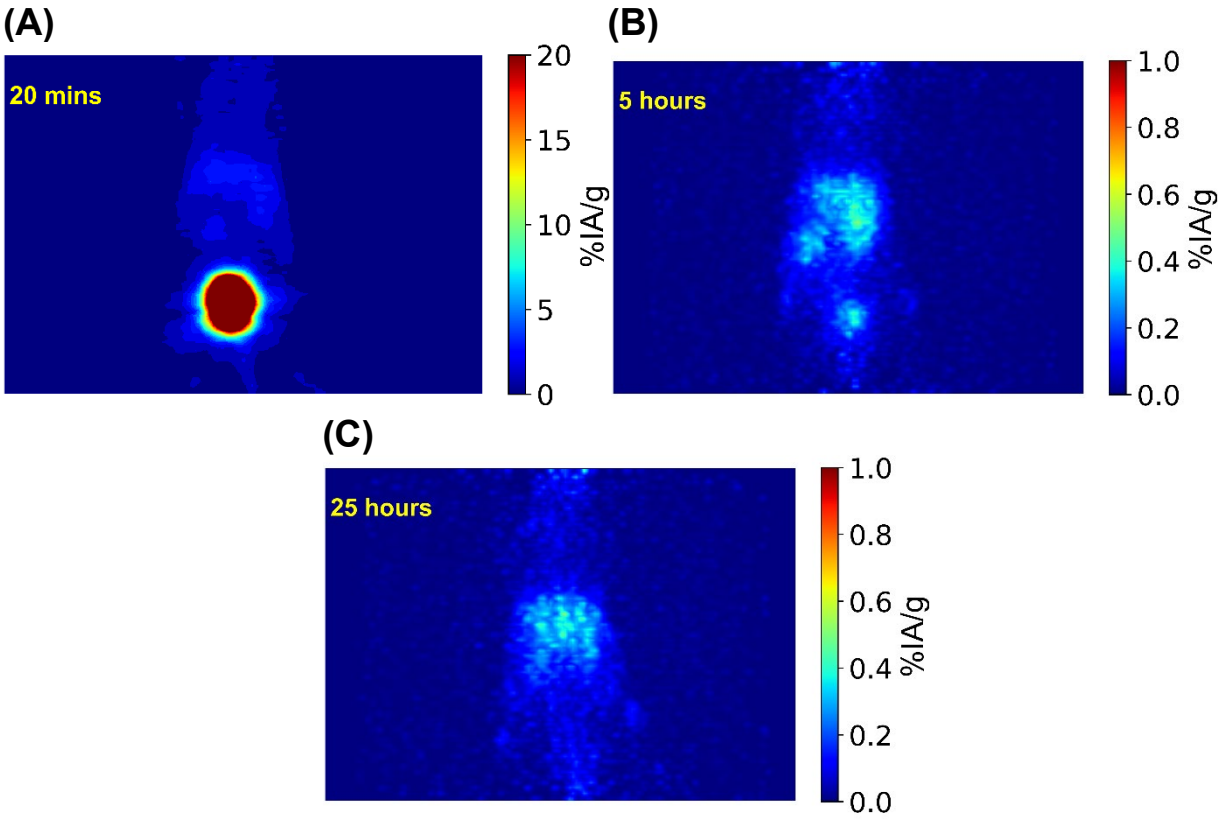

Figure 3.5: MIP PET images of a Swiss Webster mouse injected intravenously with 7.72 MBq of ^{134}Ce-DTPA at (a) 20 minutes, (b) 5 hours, and (c) 25 hours after administration. At 20 minutes, the majority of activity is located in the bladder indicating rapid, renal elimination of ^{134}Ce-DTPA.

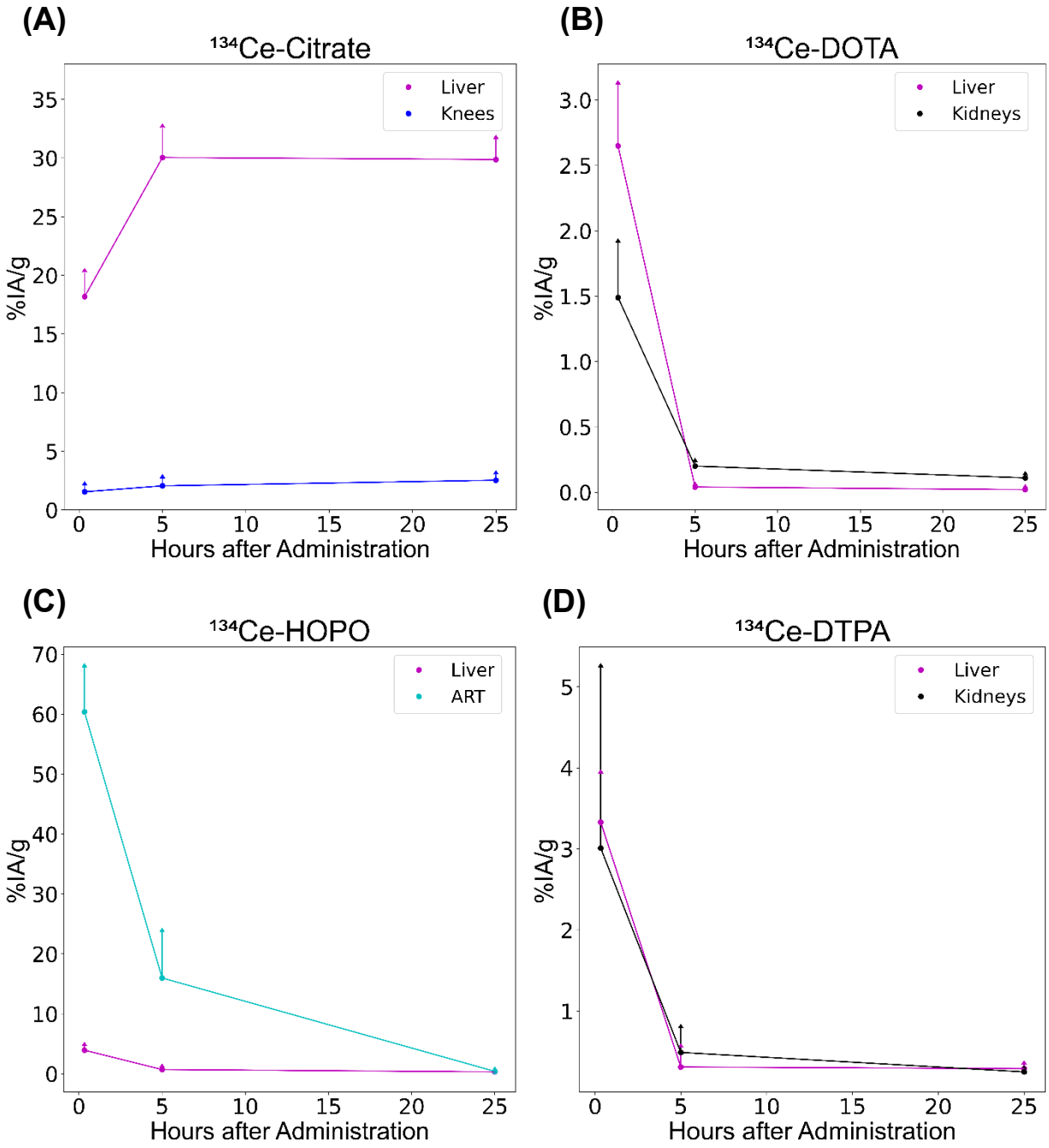

Figure 3.6: ROI analysis of organs of interest in Swiss Webster mice administered intravenously with (A) ^{134}Ce-Citrate, (B) ^{134}Ce-DOTA, (C) ^{134}Ce-HOPO, or (D) ^{134}Ce-DTPA. Each data point is the average value of the 4 mice in each group, and the error bars represent the 1-sigma standard deviation. Only the upper error bar is displayed for ease of visualization. ART is abdominal remaining tissue.

3.3.2 ^{134}Ce *ex vivo* biodistribution and postmortem imaging

The postmortem images of ^{134}Ce-HOPO biodistribution corroborate with the live animal images (Fig. 3.7). The early timepoints (10 minutes and 4 hours) exhibit uptake in the liver and the gastrointestinal tract exhibiting the familiar hepatobiliary elimination pathway. By 24 hours, minimal activity remains (notice the high signal to noise ratio in Figure 3.7C) with the residual predominately in the liver. The *ex vivo* biodistribution is also indicative of the hepatobiliary elimination pathway with the liver having an uptake of 13.22 ± 4.54 %RA/g at 10 minutes and decreasing to 1.60 ± 0.35 %RA/g at 24 hours (Fig. 3.9). The abdominal remaining tissue gradually decreases from 5.54 ± 0.43 %RA/g at 10 minutes to 0.26 ± 0.35 %RA/g at 24 hours. Minimal uptake is also apparent in the lungs, kidneys, and spleen throughout the study.

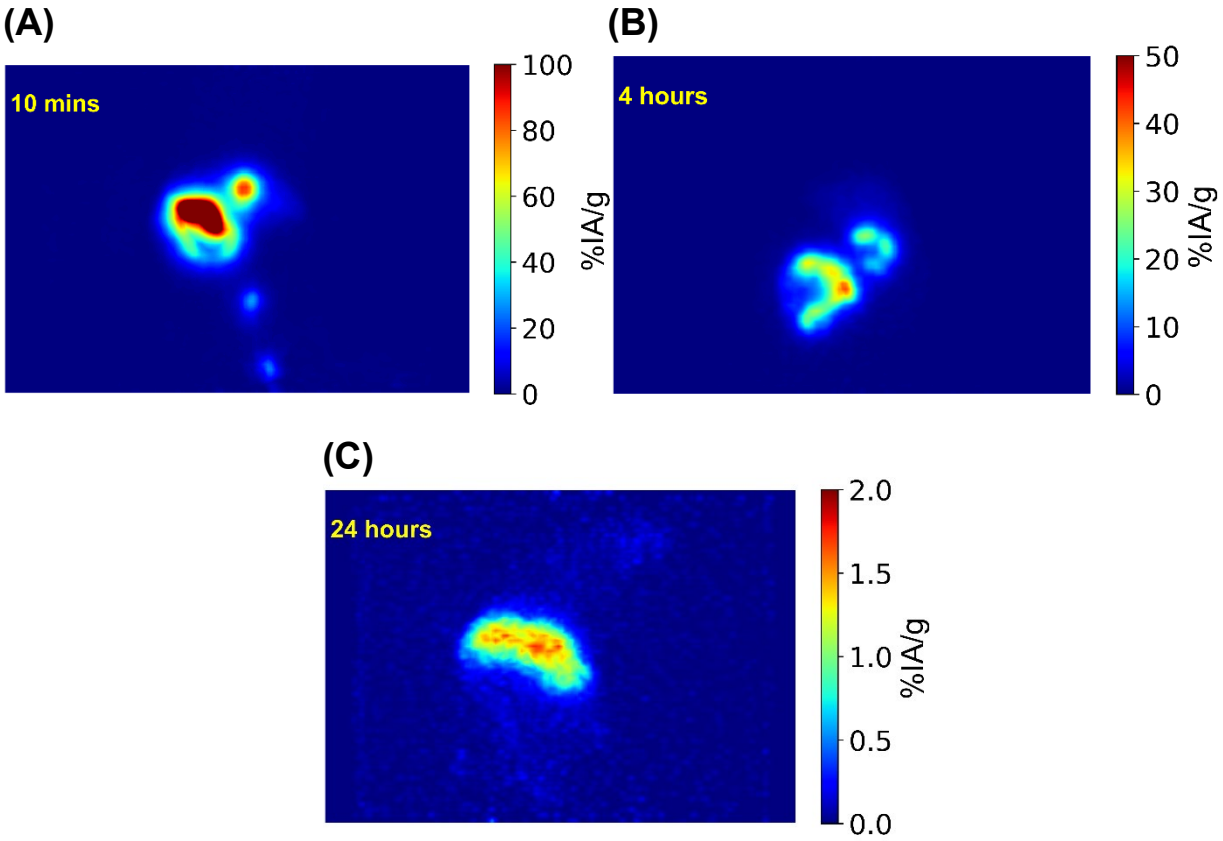

Figure 3.7: Postmortem MIP PET images of a Swiss Webster mouse injected intravenously with 3.19 MBq of ^{134}Ce-HOPO at (a) 10 minutes, (b) 4 hours, and (c) 24 hours after administration.

The postmortem images of ^{134}Ce-DTPA biodistribution display rapid renal elimination like the live animal images (Fig. 3.8). The majority of the activity is located in the bladder and kidneys at 10 minutes. By 4 hours, most of the activity was already eliminated from the mouse with the residual activity located in the liver and the kidneys. By 24 hours, the only remaining activity is located in the liver. The *ex vivo* biodistribution further confirms these results by indicating renal elimination with the kidneys having an uptake of 56.41 ± 24.38 %RA/g at 10 minutes and rapidly decreasing to 0.67 ± 0.06

%RA/g at 4 hours (Fig. 3.9). The abdominal remaining tissue (which contains the bladder) also shows elevated uptake at 10 minutes (6.66 ± 1.14 %RA/g) and rapidly decreases to minimal levels by 4 hours (0.22 ± .09 %RA/g). One of the challenging aspects of doing any postmortem bladder measurement is that the euthanasia technique that is used causes the mouse to empty its bladder upon death. This leads to the activity levels that are reported to be smaller than actual activity levels when the mouse is alive. This difference in bladder activities is also apparent when comparing the 10 minute postmortem and live animal images (Fig. 3.8A and 3.5A) where the postmortem bladder is smaller in volume than the live animal image bladder. The liver uptake also shows a rapid decline from 6.78 ± 3.72 %RA/g at 10 minutes to 1.44 ± 0.29 %RA/g at 4 hours and then stabilizes.

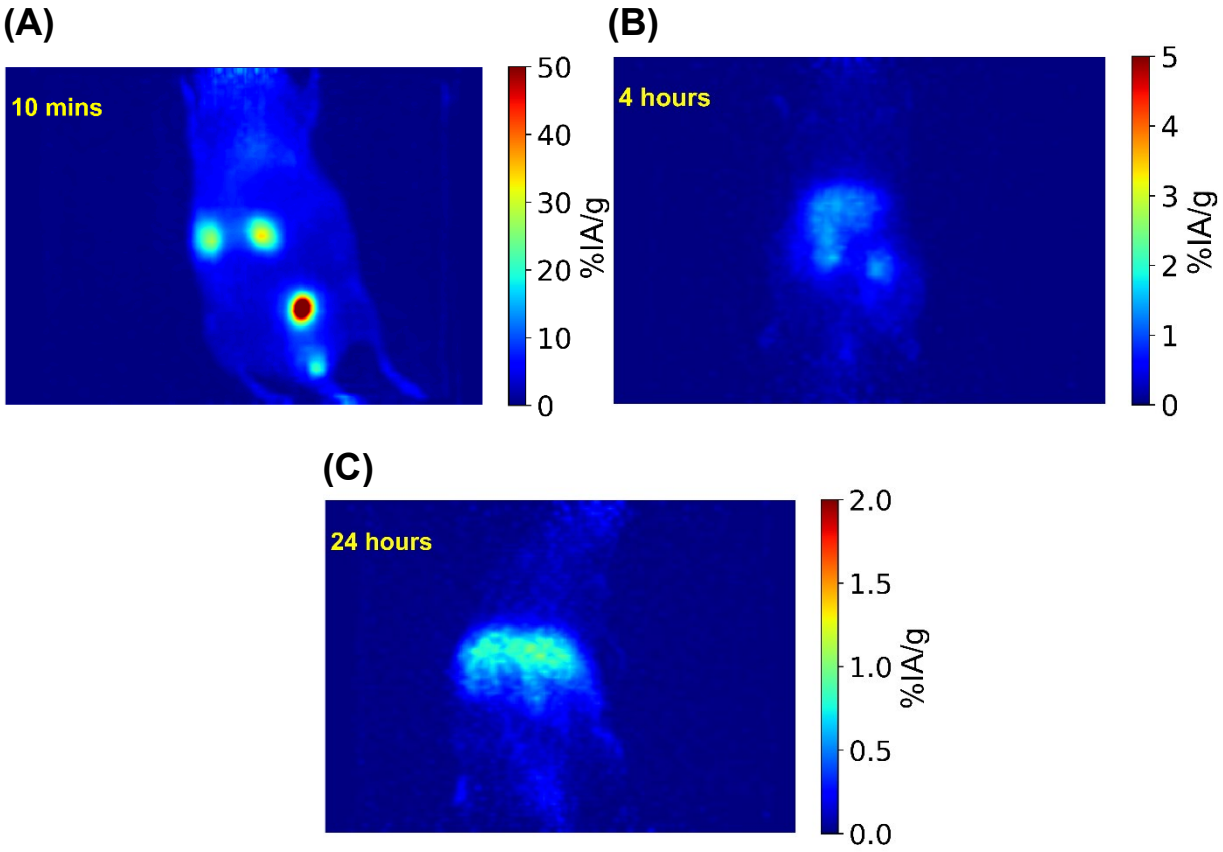

Figure 3.8: Postmortem MIP PET images of a Swiss Webster mouse injected intravenously with 6.27 MBq of ^{134}Ce-DTPA at (a) 10 minutes, (b) 4 hours, and (c) 24 hours after administration.

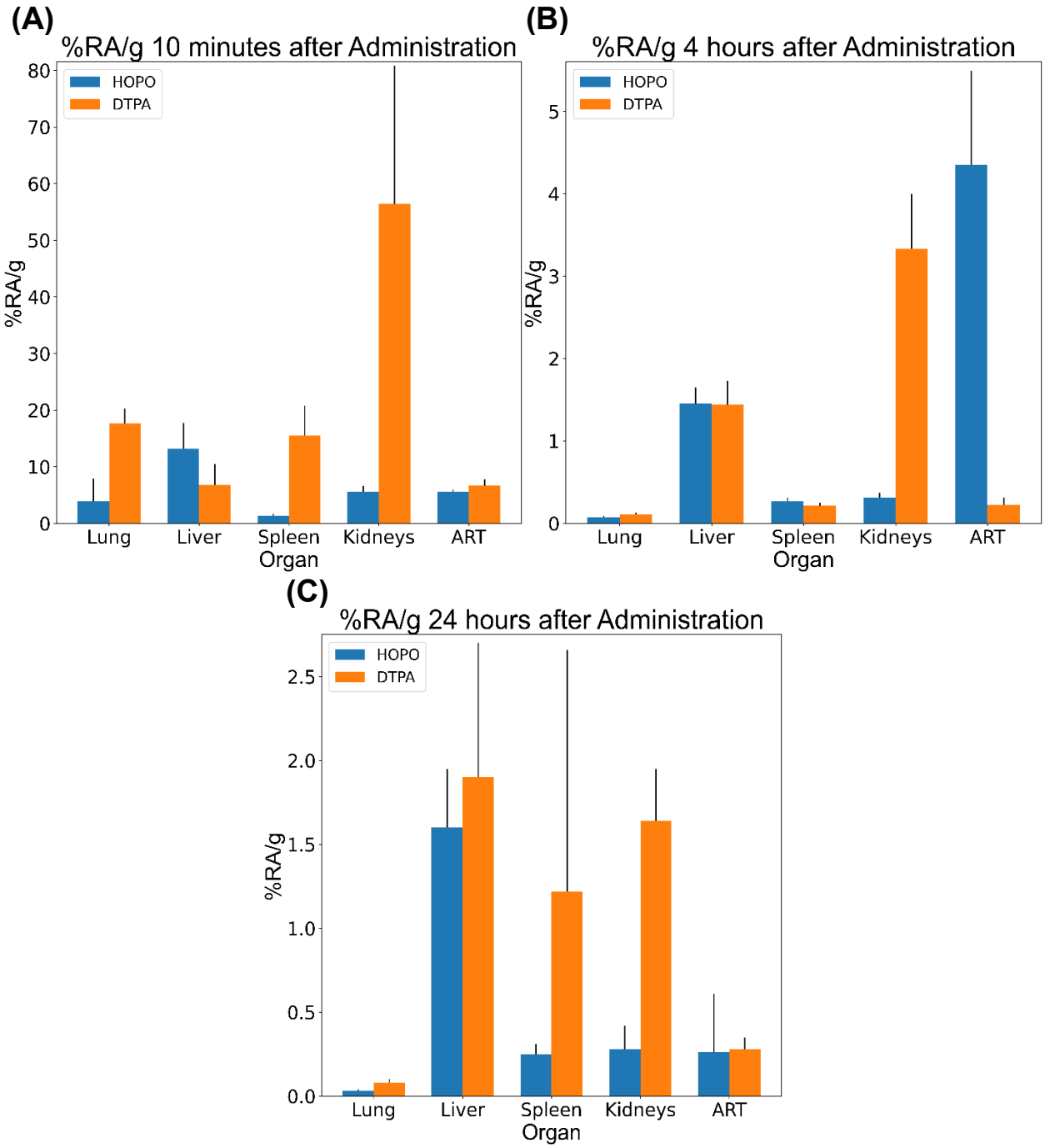

Figure 3.9: *Ex vivo* ^{134}Ce-HOPO and ^{134}Ce-DOTA biodistribution in Swiss Webster mice in terms of %RA/g at (a) 10 minutes, (b) 4 hours, and (c) 24 hours after administration measured by gamma counting. Each data point is the average value of the 3 mice in each group, and the error bars represent the 1-sigma standard deviation. Only the upper error bar is displayed for ease of visualization. ART is abdominal remaining tissue.

3.3.3 ^{86}Y *in vivo* stability

The siderocalin binding assay indicated negligible amounts of ^{86}Y went through the denoting a >99% radiochemical yield. Similarly to ^{134}Ce-HOPO, ^{86}Y-HOPO displayed hepatobiliary elimination with the live animal PET images displaying activity predominately traversing through the liver and gastrointestinal tract (Fig. 3.10). By 24 hours, the vast majority of activity was eliminated by the mice (notice the high signal to noise ratio in Figure 3.10C), and at 48 hours just noise was imaged indicating high *in vivo* stability. This is corroborated by the ROI analysis where the uptake in both the liver (101.77 ± 42.93 %IA/g at 15 minutes to 0.32 ± 0.44 %IA/g at 24 hours) and abdominal remaining tissue (136.35 ± 42.64 %IA/g at 15 minutes to 0.22 ± 0.11 %IA/g at 24 hours) decreases to negligible values by 24 hours (Fig. 3.11). No ROI results are provided for the 48 hour image since no activity uptake was apparent.

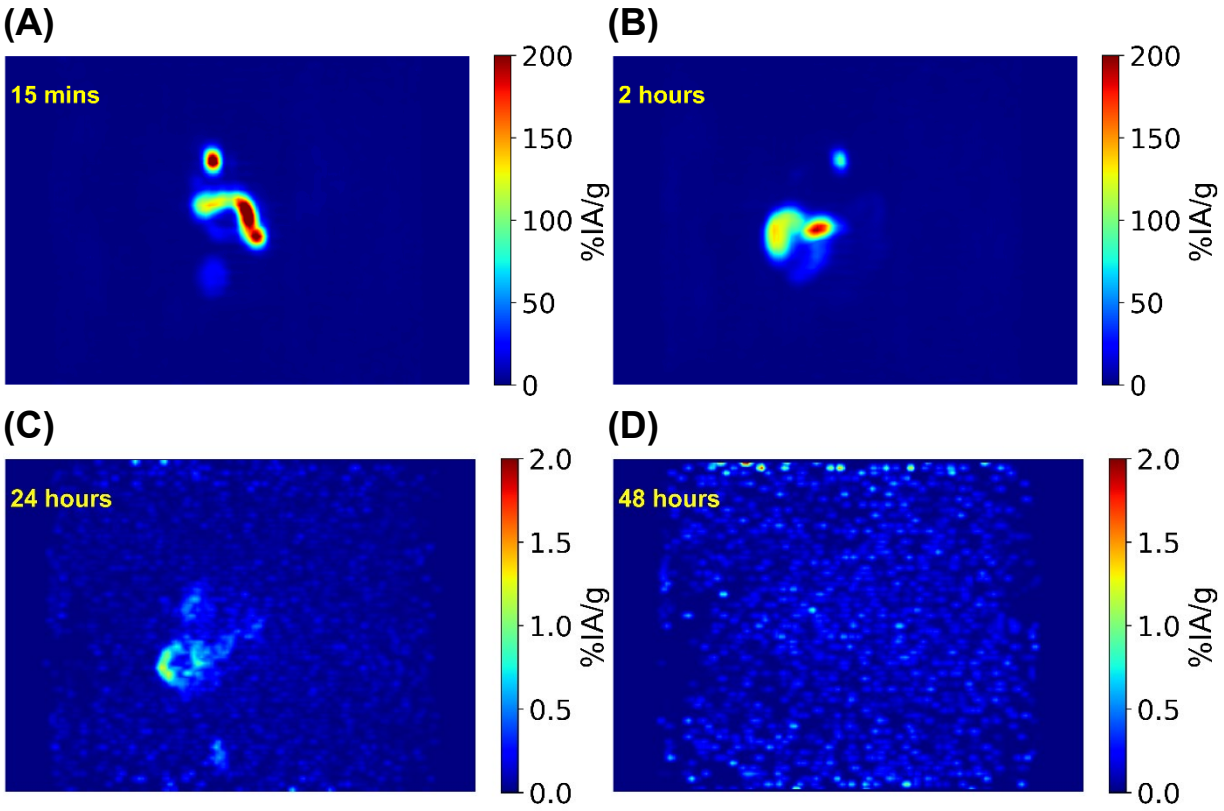

Figure 3.10: MIP PET images of a Swiss Webster mouse injected intravenously with 3.44 MBq of ^{86}Y-HOPO at (a) 15 minutes, (b) 2 hours, (c) 24 hours, and (d) 48 hours after administration.

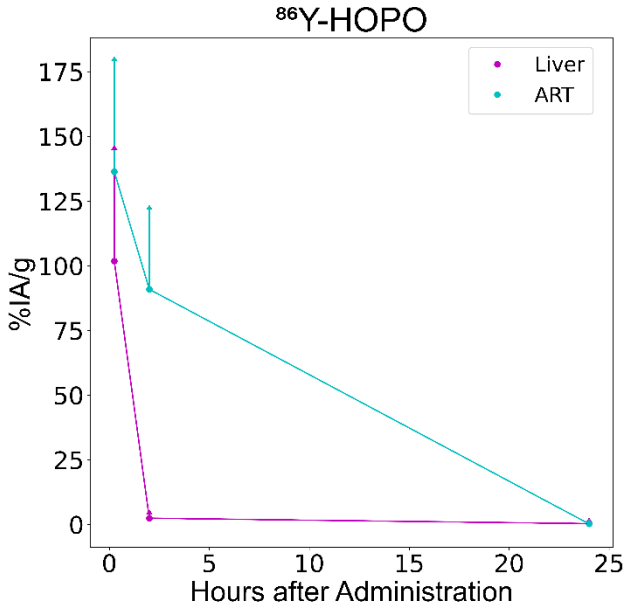

Figure 3.11: ROI analysis of organs of interest in Swiss Webster mice administered intravenously with ^{86}Y-HOPO. Each data point is the average value of the 3 mice in each group, and the error bars represent the 1-sigma standard deviation. Only the upper error bar is displayed for ease of visualization. ART is abdominal remaining tissue.

3.4 Discussion

The goal of these *in vivo* stability studies is to see if the radiometal follows the pharmacokinetics and elimination pathways of the chelator. All of these chelators that were discussed in this chapter should be eliminated within 24-48 hours. A complex with a high *in vivo* stability would be represented by little to no activity at later timepoints. A complex with poor *in vivo* stability would be represented by a large amount of activity located at organs associated with the corresponding radiometal's natural biodistribution. As an example, the ^{134}Ce-citrate (which models cerium natural biodistribution since ^{134}Ce-citrate demetallates *in vivo*) images indicate uptake primarily in the liver and some bone uptake which is similar to the ^{225}Ac-acetate (which models free ^{225}Ac)[57,58]. The $^{134}Ce^{III}$-DOTA and $^{134}Ce^{III}$-DTPA follow both $^{225}Ac^{III}$-DOTA and $^{225}Ac^{III}$-DTPA biodistribution with a rapid renal elimination pathway and minimal activity remaining in the liver, kidneys, and bones[57]. $^{134}Ce^{IV}$-HOPO follows a slower hepatobiliary with the residual activity located in the liver and the GI tract with no apparent bone uptake. This elimination pathway is indicative of chelators with hydroxypyridinone moieties such as Me-3,2-HOPO[101,106]. One thing to consider if using $^{134}Ce^{IV}$ as a surrogate for $^{227}Th^{IV}$ is that if cerium is released *in vivo*, it will be stabilized to 3+ and no longer acts as a surrogate for $^{227}Th^{IV}$[144–146]. This fact demonstrates the necessity of using a chelator, such as HOPO, that can strongly bind to both $^{134}Ce^{IV}$ and $^{227}Th^{IV}$.

Moreover, the ^{86}Y-HOPO complex follows a similar elimination pathway as $^{134}Ce^{IV}$-HOPO with minimal activity remaining in the GI tract at 24 hours and no apparent activity at all at 48 hours. Furthermore, no apparent activity was located in the

bones and kidneys (where free yttrium tends to accumulate) which is indicative of high *in vivo* stability[108].

One of the caveats of using ^{134}Ce in radiopharmaceuticals is the amount of excess chelator that is necessary to ensure a high radiochemical yield. The specific activity of the shipments of ^{134}Ce has ranged from 16.4 kBq/ng (activity of ^{134}Ce to the total mass of cerium) to 96.2 of ^{134}Ce kBq/ng. This corresponds to anywhere from 114-666 total atoms of cerium to atoms of ^{134}Ce (this excess of cerium atoms is primarily from all the radiompurities). While these experiments used excess chelator to ensure high radiochemical in order to investigate the *in vivo* stability of ^{134}Ce complexes, a large excess of chelators is not always possible nor feasible for producing targeted radiopharmaceuticals. In addition, heating at an elevated temperature for a long duration of time was performed on all complexes discussed in this Chapter in order to minimize experimental variables. This is not necessarily needed for HOPO which can form rapidly form stable complexes at room temperature[139,140]. Future work will optimize the radiolabeling condition for these complexes (amount of excess chelator and incubation temperature and time).

One open ended question that remains is whether ^{134}La stays in the chelator after the decay of ^{134}Ce. One potential way to investigate this phenomenon is to use liquid chromatography mass spectrometry[147]. The liquid chromatography can separate free ^{134}La from the ^{134}Ce-complex while the mass spectrometer can determine the ratio of each of the species. While this doesn't give insight into what happens to the ^{134}Ce complex *in vivo*, it would illuminate what types of target vectors are compatible with ^{134}Ce based on whether they internalize or not[34].

3.5 Conclusions

Herein, it was demonstrated that $^{134}Ce^{III}$-DTPA, $^{134}Ce^{III}$-DOTA, $^{134}Ce^{IV}$-HOPO, and ^{86}Y-HOPO all had high *in vivo* stability, rapid pharmacokinetics, and little to no residual activity after 24-48 hours after administration. These studies illuminate that ^{134}Ce could potentially be an effective theranostic matched pair for either $^{225}Ac^{III}$ or $^{227}Th^{IV}$ (based on appropriate chelator selection) and that 3,4,3-LI(1,2-HOPO) could advance ^{90}Y/^{86}Y theranostics. Future work will investigate DOTA-based antibody drug conjugates incorporating ^{134}Ce (see Chapter 4), bifunctional variants of 3,4,3-LI(1,2-HOPO) labeled with ^{134}Ce or ^{86}Y, and siderocalin fusion proteins bound to ^{86}Y-3,4,3-LI(1,2-HOPO) complexes (see Chapter 6)[36,148,149].

CHAPTER 4: Evaluating ^{134}Ce as a theranostic matched pair for antibody drug conjugates incorporating ^{225}Ac

4.1 Introduction

Targeted alpha therapy, where alpha-emitting radionuclides are transported to diseased tissues via biochemical targeting vectors, is a promising approach for cancer therapy[8–10,150]. Once at the targeted sites, radionuclides deliver alpha particles that can deposit large amounts of energy in short distances, thus minimizing the damage to surrounding, non-diseased tissue. Both ^{225}Ac ($T_{1/2}$ = 9.9 days) and ^{227}Th ($T_{1/2}$ = 18.7 days) have shown early success, in part due to decay chains that generate a series of four or five alpha particles[11,62,151–153]. In addition, the long half-lives of both radionuclides allow for compatibility with a wide variety of targeting vectors ranging from small peptides and antibody fragments to large antibodies[62,78,101].

One of the challenges associated with the development of radiopharmaceuticals incorporating ^{225}Ac and ^{227}Th is the lack of imageable photons or positrons from therapeutic quantities of either of these radionuclides or other actinium and thorium isotopes. This prevents routine treatment planning and monitoring of the radiopharmaceuticals with contemporary clinical SPECT and PET scanners, necessitating the use of a chemically analogous diagnostic radionuclide. Among available PET imaging radiometals, ^{68}Ga ($T_{1/2}$ = 67.7 min) and ^{89}Zr ($T_{1/2}$ = 78.4 h) have been used as theranostic matched pairs ^{225}Ac and ^{227}Th, respectively[11,154]. Unfortunately, both of these PET isotopes display different coordination properties from those of their proposed therapeutic counterparts making them poor chemical surrogates. Furthermore, because of the short half-life of ^{68}Ga, monitoring the biodistribution of ^{225}Ac over a few days is not possible. Recently, it was demonstrated that the *in vivo* generator ^{134}Ce ($T_{1/2}$ = 3.2 days)/^{134}La ($T_{1/2}$ = 6.5 minutes) can mimic either $^{225}Ac^{III}$ or $^{227}Th^{IV}$ with appropriate chelator selection (using DTPA to tune ^{134}Ce to 3+ and 3,4,3-LI(1,2-HOPO) to tune ^{134}Ce to 4+) due to the readily accessible Ce^{III}/Ce^{IV} redox couple[85]. Moreover, $^{134}Ce^{III}$-DOTA was shown to have a high *in vivo* stability and a similar biodistribution to $^{225}Ac^{III}$-DOTA which is the most commonly used complex for ^{225}Ac-based targeted radiopharmaceuticals (Chapter 3). In addition, the half-life of ^{134}Ce is long enough to allow tracing the long-term biodistribution of both ^{225}Ac and ^{227}Th.

Herein, the compatibility of ^{134}Ce in DOTA-based antibody drug conjugates is investigated. This is done by demonstrating long-term targeting for up to 9 days after injection of ^{134}Ce-DOTA-Trastuzumab in a SK-OV-3 tumor-bearing murine model. Some of the data and methods included in this Chapter have been published in a peer-reviewed journal with the permission of all authors. All of the figures have been altered for stylistic purposes.

Relevant Publications:

Bailey TA, Wacker JN, An DD, et al. Evaluation of 134Ce as a PET imaging surrogate for antibody drug conjugates incorporating 225Ac. *Nuclear Medicine and Biology*. 2022;110-111:28-36. doi:10.1016/j.nucmedbio.2022.04.007

4.2 Materials and methods

All procedures and protocols used in these studies were reviewed and approved by the Institutional Animal Care and Use Committee of LBNL and were performed in AAALAC-accredited facilities, according to prescribed guidelines and regulations. Intravenous injections into a warmed lateral tail vein and euthanasia by cervical dislocation were performed under isoflurane anesthesia.

4.2.1 Materials

The following chemicals were used as received from chemical suppliers: Trastuzumab (Absolute Antibody), S-2-(4-Isothiocyanatobenzyl)-1,4,7,10-tetraazacylododecane tetraacetic acid (p-SCN-Bn-DOTA; Macrocyclics), Mouse IgG Isotype control (IgG; ImmunoReagents), L-arginine hydrochloride (L-arginine; Spectrum), sodium bicarbonate (NaHCO3; Ward's Science), 1x sterile phosphate buffered saline (PBS, VWR), ammonium acetate (NH_4OAc; Fluka), 0.9% sterile saline (saline; APP Pharmaceuticals), Ethylenediaminetetraacetic acid disodium salt dihydrate (EDTA; VWR), Dimethyl sulfoxide (DMSO; Amresco), 40-86% Nitric Acid (HNO_3; Sigma-Aldrich), and Matrigel matrix (Matrigel; VWR). All solutions were prepared with deionized water purified by a Millipore Milli-Q water purification system. SK-OV-3 cells were used as received from ATCC.

4.2.2 Antibody conjugation

Conjugation of Trastuzumab antibodies occurred through covalent coupling of p-SCN-Bn-DOTA to the lysine residues of the antibodies[155]. In brief, 0.9 mg of Trastuzumab was buffer-exchanged into 0.1 M $NaHCO_3$ using 0.5 mL 30 kDa Amicon Ultra Centrifugal Filter Units (Millipore Sigma). Trastuzumab was then incubated with p-SCN-Bn-DOTA for 60 min at 37 °C in a DMSO matrix at a 1:40 molar ratio. The resulting solution was buffer-exchanged into 0.2 M NH_4OAc for radiolabeling. Conjugation of IgG antibodies occurred with 0.2 mg of IgG and a 1:20 antibody to chelator molar ratio using the same procedure outlined above.

4.2.3 ^{134}Ce production and radiolabeling

^{134}Ce was produced according to a previously described method at the Isotope Production Facility (IPF) of Los Alamos National Laboratory (LANL)[85]. In brief, ^{134}Ce was obtained through a ^{139}La(p,6n)^{134}Ce reaction by the 100 MeV proton bombardment of a natural lanthanum target. After dissolving the target, separation of ^{134}Ce from the rest of the lanthanum was achieved through the oxidation of Ce from +3 to +4 using $NaBrO_3$, and Ce^{IV} was separated from La^{III} using anion-exchange chromatography. At 7.3 days after end of irradiation, the purified product contained 24.7 GBq of ^{134}Ce ($T_{1/2}$ = 3.16 days), 1.4 GBq of ^{137m}Ce ($T_{1/2}$ = 34.4 hours), 122.1 MBq of ^{135}Ce ($T_{1/2}$ = 17.7 hours), and 177.6 MBq of ^{139}Ce ($T_{1/2}$ = 137.6 days). A 370 MBq sample of ^{134}Ce was

then shipped to Lawrence Berkeley National Laboratory with a specific activity of 162 kBq/ng (activity of ^{134}Ce to the total mass of cerium).

For labeling Trastuzumab and IgG, 125 MBq and 100 MBq aliquots of ^{134}Ce were added to the DOTA-Trastuzumab and DOTA-IgG solutions, respectively, followed by an incubation period of 90 min at 45 °C. The solutions were then buffer-exchanged 4 times into PBS using 0.5 mL 30 kDa Amicon Ultra centrifugal filter units to remove unlabeled metal. The ^{134}Ce-DOTA-Trastuzumab solution was diluted into saline while ^{134}Ce-DOTA-IgG was diluted into 0.1 M L-arginine in saline for animal injections.

Activities of the injection solutions were determined by gamma spectroscopy via a P-Type High Purity Germanium gamma spectrometer using the 511.00 and 604.72 keV lines of ^{134}La. Before counting, samples were allowed to sit at rest for more than 1 hour prior to measurements to allow ^{134}La to reach secular equilibrium with ^{134}Ce, allowing the ^{134}La activity to be equivalent to ^{134}Ce. The radiochemical yields were determined by measuring the activity of ^{134}Ce that stayed at the top of the 30 kDa filter (the labeled ^{134}Ce) and the activity of ^{134}Ce that was in the filtrate (the unlabeled ^{134}Ce). The radiochemical yield is then calculated by the ratio of labeled radiometal to the sum of labeled radiometal and unlabeled radiometal. The radiochemical purities of radiolabeled antibody drug conjugate solutions were determined by radio-ITLC (Bioscan System 200 Imaging Scanner), using Varian ITLC-SA strips (Agilent Technologies) and 50 mM EDTA at pH 10.5 as the mobile phase. Radiochemical purities were determined by drawing two regions of interest (using Bioscan System 200 Imaging Scanner software) over the gaussian peak at the origin (which contains the labeled antibodies) and the region outside the origin peak (which constitutes unlabeled radiometal. The radiochemical purity is then calculated by the ratio of labeled radiometal to the total amount of radiometal on the plate.

4.2.4 Small animal PET imaging and biodistribution

Biodistribution studies were performed to evaluate the tumor targeting capability of ^{134}Ce-DOTA-Trastuzumab in SK-OV-3 tumor-bearing (0.39 ± 0.11 cm^3), adult female NOD SCID mice (15 weeks; 24.3 ± 1.7 g; Charles River Laboratories, NY). The SK-OV-3 tumors were passaged in mice and prepared as single-cell suspensions (10^6 cells) in 50% Matrigel prior to subcutaneous transplantation in the right mammary fat pad of NOD SCID mice under isoflurane anesthesia. Groups of three mice were injected intravenously with a single 0.2 mL dose of either ^{134}Ce-DOTA-Trastuzumab (3.20 ± 0.1 MBq, 738.5 nM of antibody) or ^{134}Ce-DOTA-IgG (1.28 ± 0.19 MBq, 189.6 nM of antibody). Mice were anesthetized at 20 minutes, 5 hours, 25 hours, 52 hours, 75 hours, 100 hours, 124 hours, and 147 hours, and subsequently imaged on a Concorde microPET R4 in the head first prone position. At 214 hours, mice were euthanized by cervical dislocation, subsequently imaged 1 hour after euthanasia, and then dissected for an ex vivo biodistribution study. For each mouse, kidneys, liver, spleen, and tumor were dissected, and the abdominal remainder tissue (ART, which includes the (GI) tract, reproductive organs, urinary bladder, and abdominal fat) was removed. The organ samples and the partially eviscerated carcasses were managed as individual samples. All samples were dried at 100 °C, dry-ashed at 575 °C, and dissolved in concentrated nitric acid. The ashed-soft tissue in the carcass was rinsed from the ashed-bone with HNO_3 and both soft tissue and bone were diluted with water into polyethylene bottles.

The dissolved organs, 2 g aliquots of the soft tissue and bone, and 2 mL aliquots of standard solutions were mixed with 10 mL of Ultima Gold LLT (Perkin Elmer, Shelton) for counting by liquid scintillation counting (Packard Tri-Carb model B4430, Perkin Elmer) using a window of 50 keV-2000 keV with the results being reported in terms of percent injected activity per gram of tissue (%IA/g).

The Concorde microPET R4 supports a transaxial resolution of 1.66 mm FWHM, an energy window of 350-650 keV, and a coincidence timing window of 6 ns were used during image acquisition. Images were reconstructed using 3D ordered subset expectation maximum followed by maximum a posteriori onto a 128 x 128 x 63 (0.85 x 0.85 x 1.2 mm^3) matrix. Image data underwent normalization, dead-time count losses, positron branching ratio, and decay corrections. The counting rates in the processed images were converted to the percentage of injected activity per gram of tissue (%IA/g) using a system calibration factor obtained by imaging a cylinder filled with a known concentration and volume of the injection solutions. The reported images are coronal maximum intensity projection images. Quantitative imaging analysis on organs of interest was done by hand-drawing three-dimensional regions of interest (ROI) using AMIDE v1.0.5 with the results being reported in terms of percent injected activity per gram of tissue (%IA/g)[143].

4.3 Results

The radiochemical yield was determined to be 80.9% for ^{134}Ce-DOTA-Trastuzumab, while it was 43.7% for ^{134}Ce-DOTA-IgG. Radiochemical purity was determined by radio-ITLC where the antibody drug conjugate stayed at the origin and the free metal moved up the plate with the solvent front (Fig. 4.1A). The radiochemical purity was determined to be 80.7% for ^{134}Ce-DOTA-Trastuzumab (Fig 4.1B) and 68.8% for ^{134}Ce-DOTA-IgG (Fig 4.1C).

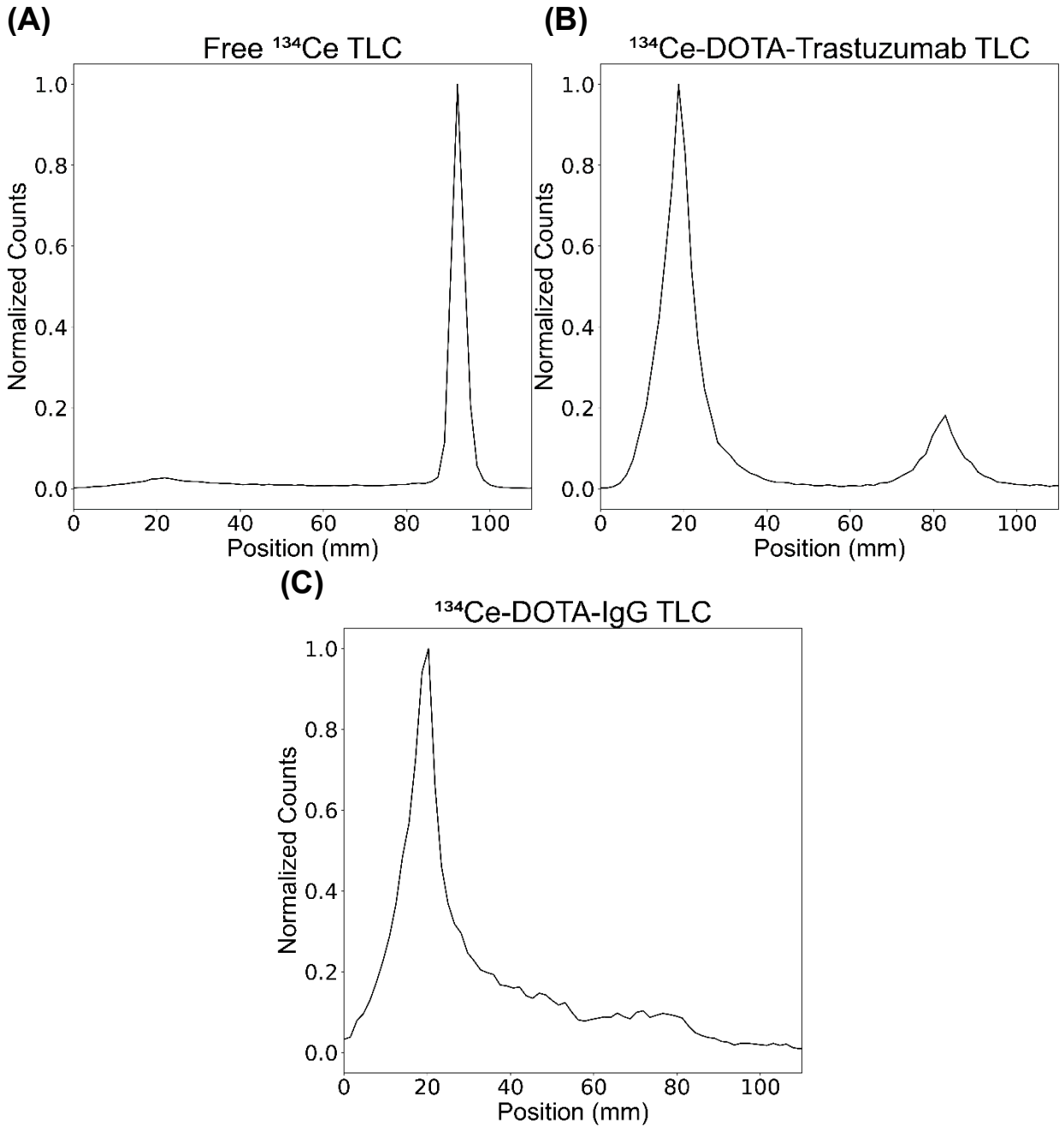

Figure 4.1: Radio-ITLC traces of (A) free ^{134}Ce, (B) ^{134}Ce-DOTA-Trastuzumab, and (C) ^{134}Ce-DOTA-IgG.

Figure 4.2A shows representative MIP PET images of 134Ce-DOTA-Trastuzumab in a SK-OV-3 tumor-bearing NOD SCID mouse through 147 h. At 214 h, mice were euthanized and imaged 1 h later (allowing ^{134}La to reach secular equilibrium with ^{134}Ce) (Fig. 4.3A). Through the first 25 h after administration, tumor uptake steadily increased over time (1.76 ± 0.17 %IA/g to 9.28 ± 2.07 %IA/g) (Fig. 4.4A). From 25 h to 75 h, tumor uptake plateaued and then steadily decreased from 75 h through 147 h (8.83 ± 2.73 %IA/g to 5.49 ± 2.00 %IA/g). The postmortem image at 214 h also displayed tumor uptake at 3.74 ± 0.86 %IA/g. The liver uptake steadily decreased over

time, from 16.90 ± 4.87 %IA/g at 20 min to 4.30 ± 0.18 %IA/g at 147 h. The knee bones uptake generally remained constant over the 147 h (2.99 ± 0.36 %IA/g at 20 min to 2.37 ± 0.79 %IA/g at 147 h), while the ART steadily decreased over the 147 h (2.78 ± 1.06 %IA/g to 1.41 ± 0.61 %IA/g). *Ex vivo* biodistribution confirmed tumor uptake at 214 h (6.19 ± 2.08 %IA/g) (Fig. 4.5A). Elevated uptake in both the liver and spleen was also apparent with respective burdens of 4.77 ± 1.06 %IA/g and 20.72 ± 12.83 %IA/g. The entire skeletal system was also counted, revealing an uptake of 4.20 ± 0.36 %IA at 214 h (Fig. 4.5B).

Figure 4.2B shows representative coronal MIP PET images of 134Ce-DOTA-IgG in a SK-OV-3 tumor-bearing NOD SCID mouse through 147 h. At 214 h, mice were euthanized and imaged 1 hour later (allowing ^{134}La to reach secular equilibrium with ^{134}Ce) (Fig. 4.3B). Through all 147 h, tumor uptake remained minimal (0.70 ± 0.14 %IA/g at 20 min to 0.59 ± 0.11 %IA/g at 147 h) (Fig. 4.4B). The postmortem images at 214 h also displayed minimal tumor uptake (0.50 ± 0.28 %IA/g). Liver uptake increased initially from 39.78 ± 2.65 %IA/g at 20 min to 43.67 ± 2.39 %IA/g at 5 h and slightly decreased over time, ending up at 37.58 ± 5.68 %IA/g at 147 h. The knee bone uptake remained relatively constant over time (1.23 ± 0.15 %IA/g at 20 min to 1.05 ± 0.14 %IA/g at 147 h), while the ART uptake slightly decreased over time (0.59 ± 0.10 %IA/g at 20 min to 0.36 ± 0.07 %IA/g at 147 h). *Ex vivo* biodistribution confirmed minimal tumor uptake at 214 h (0.49 ± 0.18 %IA/g) (Fig. 4.5A). Elevated uptake was confirmed in both the liver and the spleen with respective burdens of 53.37 ± 5.84 %IA/g and 28.30 ± 7.71 %IA/g. The entire skeletal system was also counted, displaying an uptake of 5.77 ± 0.74 %IA at 214 h (Fig. 4.5B).

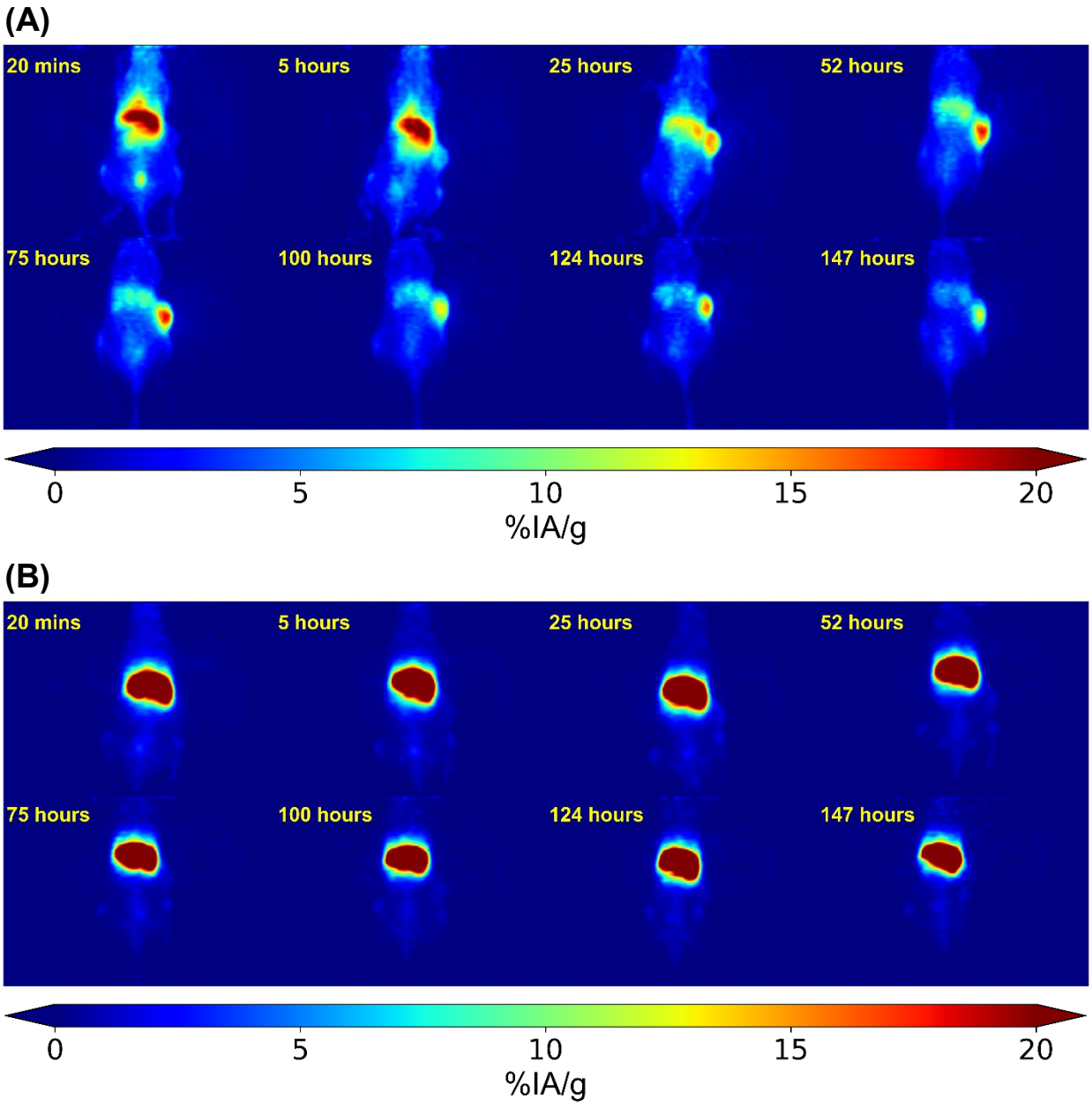

Figure 4.2: (A) MIP PET images of a SK-OV-3 tumor bearing NOD SCID mice injected intravenously with 3.20 MBq ^{134}Ce-DOTA-Trastuzumab over 147 hours after administration. (B) MIP PET images of a SK-OV-3 tumor bearing mice injected intravenously with 1.28 MBq ^{134}Ce-DOTA-IgG over 147 hours after administration.

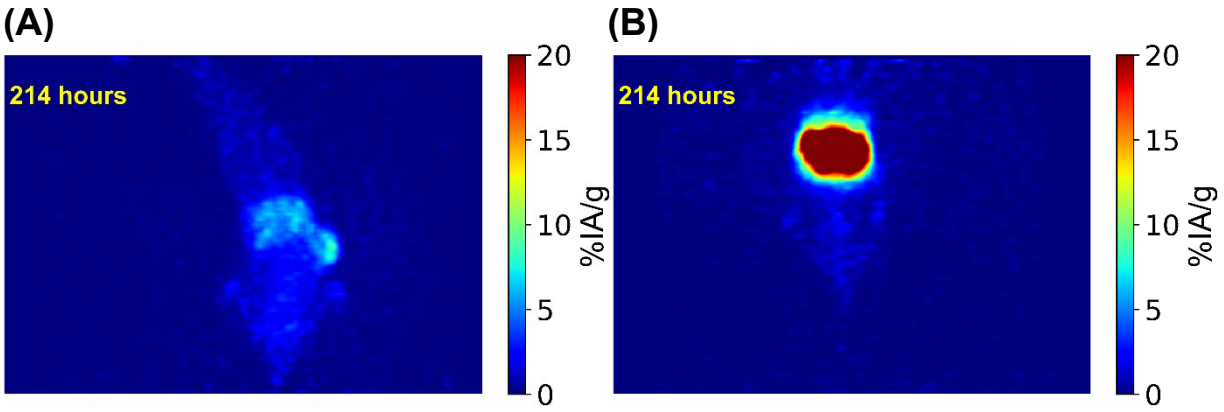

Figure 4.3: (A) Postmortem MIP PET image of a SK-OV-3 tumor bearing NOD SCID mouse injected with 3.20 MBq ^{134}Ce-DOTA-Trastuzumab at 214 hours after administration. (B) Postmortem MIP PET image of a SK-OV-3 tumor-bearing NOD SCID mouse injected with 1.28 MBq ^{134}Ce-DOTA-IgG at 214 hours after administration. Both mice were imaged at 1 hour after euthanasia.

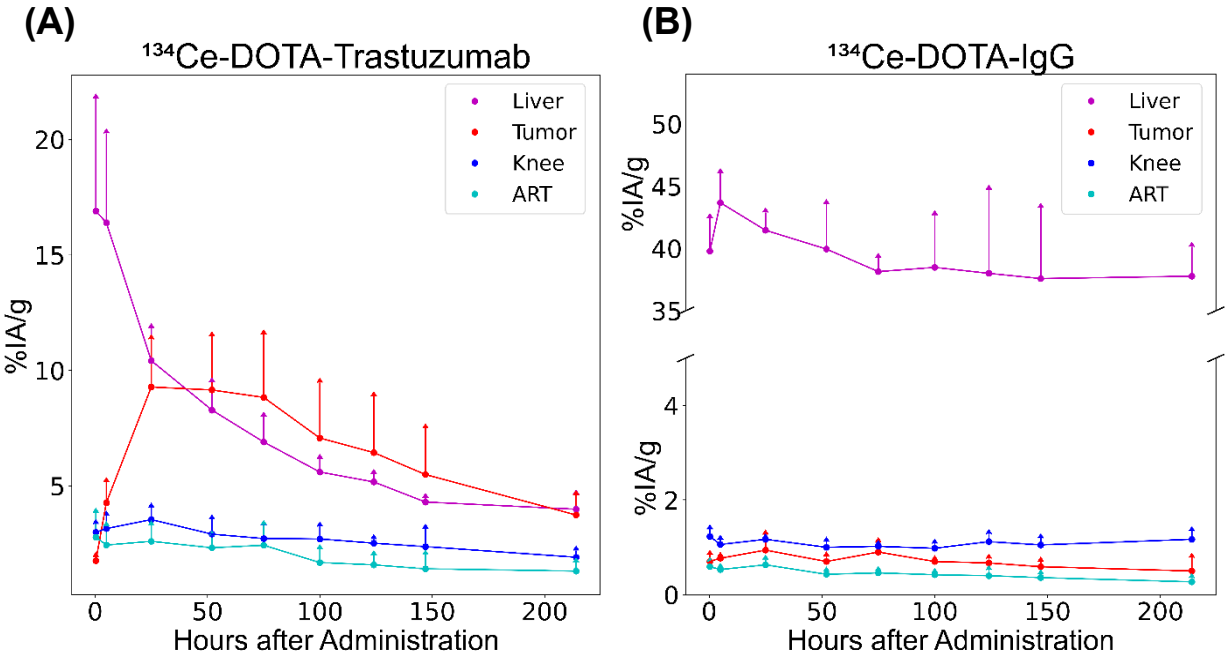

Figure 4.4: ROI analysis of organs of interest in SK-OV-3 tumor bearing NOD SCID mice administered intravenously with (A) ^{134}Ce-DOTA-Trastuzumab or (B) ^{134}Ce-DOTA-IgG. Each data point is the average value of the 3 mice in each group, and the error bars represent the 1-sigma standard deviation. Only the upper error bar is displayed for ease of visualization. ART is abdominal remaining tissue.

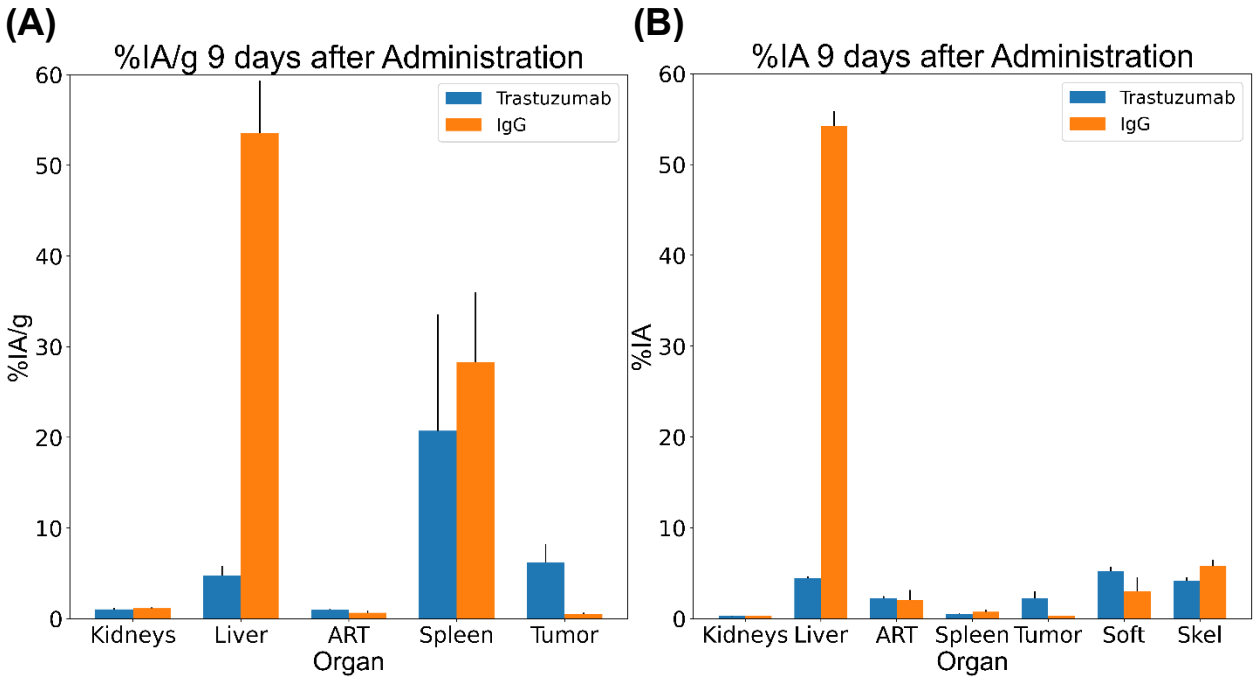

Figure 4.5: *Ex vivo* ^{134}Ce-DOTA-Trastuzumab and ^{134}Ce-DOTA-IgG biodistribution SK-OV-3 tumor bearing NOD SCID mice in terms of (A) %IA/g and (B) %IA at 9 days after administration measured by liquid scintillation counting. Each data point is the average value of the 3 mice in each group, and the error bars represent the 1-sigma standard deviation. Only the upper error bar is displayed for ease of visualization. ART is abdominal remaining tissue. Skel is the entire skeletal system. Soft is the remaining soft tissue that was not already harvested.

4.4 Discussion

As discussed in Chapter 2, there has been recent interest in other PET-active lanthanum isotopes as surrogates for ^{225}Ac such as ^{132}La ($T_{1/2}$ = 4.8 hours) and ^{133}La ($T_{1/2}$ = 3.9 hours)[78,84]. The ^{134}Ce/^{134}La *in vivo* generator system stands out amongst these other radiolanthanum isotopes due to its much longer half-life, allowing the tracing of large macromolecules (such as antibodies) over long periods of time. These results demonstrate that ^{134}Ce allows for monitoring elevated tumor uptake of Trastuzumab over 214 h which would not be possible with ^{132}La or ^{133}La.

When compared to a previously published ^{225}Ac-DOTA-Trastuzumab biodistribution study, the *in vivo* stability and biodistribution of the ^{134}Ce radimmunoconjugate were both similar[38,63]. The Borchardt, et al. study also displayed minimal bone uptake, gradually decreasing liver uptake, and elevated tumor uptake is evident over 120 h.

One of the challenges involved in PET imaging ^{134}Ce is the high positron endpoint energy (2709 keV) of ^{134}La can degrade the system spatial resolution of a PET scanner[51]. While not as pertinent for clinical PET scanners, in preclinical PET scanners this can lead to partial volume effects, which can then result in underestimation of the true activity concentration of a small structure. This is apparent when comparing the ROI analysis at 214 h to the ex vivo biodistribution of the tumor in the mice that were

administered ^{134}Ce-DOTA-Trastuzumab. The ROI analysis yielded 3.74 ± 0.86 %IA/g at 214 h, less than the *ex vivo* biodistribution result of 6.19 ± 2.08 %IA/g, which is not impacted by the partial volume effect. To minimize this partial volume effect in ^{134}Ce preclinical imaging, it is advisable to use dual-modality PET-MRI scanners, which will reduce the range of the positrons[55,156].

One of the open-ended questions that is yet to be addressed by the ^{134}Ce/^{134}La system is whether ^{134}La is released from its chelate after the decay of ^{134}Ce *in vivo*, leading to the potential redistribution of ^{134}La. While a similar *in vivo* generator system, ^{140}Nd (ε, $T_{1/2}$ = 3.4 days) /^{140}Pr (β+, $T_{1/2}$ = 3.4 minutes), was shown to display this redistribution effect with the non-internalizing targeting vector DOTA-LM3, the methodology used would not work with a targeting vector that can be internalized (such as Trastuzumab)[35,157]. One potential way to evaluate if redistribution occurs with any targeting vector is to leverage the ^{139}Ce radio-impurity 165.86 keV gamma photon[85]. If a ^{134}Ce labeled targeting vector is imaged by a dual-modality PET-SPECT scanner, the PET image will display the biodistribution of ^{134}La, and the SPECT image will display the biodistribution of ^{139}Ce, which will have the equivalent biodistribution of ^{134}Ce. Any significant differences between the two isotopes' biodistribution would indicate redistribution. Future work will attempt to tackle this question.

4.5 Conclusions

Herein, it was demonstrated that the long half-life of ^{134}Ce allows for antibody drug conjugates incorporating ^{134}Ce to image tumors for long periods of time after administration. In addition, because of the high *in vivo* stability of $^{134}Ce^{III}$-DOTA and $^{134}Ce^{III}$ chemical similarity to $^{225}Ac^{III}$, ^{134}Ce-DOTA-Trastuzumab can act as a surrogate for ^{225}Ac-DOTA-Trastuzumab. Future work will focus on investigating the redistribution effect of ^{134}La from its ^{134}Ce parent.

CHAPTER 5: Optimizing radiolabeling of ^{224}Ra generator-produced ^{212}Pb

5.1 Introduction

The use of α emitters in targeted radionuclide therapy has been shown to have many advantages in comparison to β emitters. The short path lengths of α particles allow for diseased tissue to be selectively destroyed while sparing nearby healthy tissue unlike β particles. In addition, there has been clinical evidence that targeted alpha therapy can be effective against chemotherapy-resistant, photon irradiation-resistant, and castration-resistant lesions[11,12]. Despite these advantages, the availability of α emitters with a suitable half-life for clinical use is limited. Often, the radionuclide needs to be produced offsite, purified, shipped to the clinic, radiolabeled to a targeting vector, and after quality control, the targeted radiopharmaceutical can be administered to the patient. Moreover, monoclonal antibodies are common targeting vectors and can take multiple days to uptake sufficiently in a lesion due to their slower pharmacokinetics[36,129]. Both ^{225}Ac ($T_{1/2}$=9.9 days) and ^{227}Th ($T_{1/2}$=18.7 days) have long enough half-lives to be effective in targeted radiopharmaceuticals, and they have shown great success in clinical trials due to their decay chains which feature 4 or 5 alpha emissions[11,25]. Unfortunately, these long half-lives are a double-edged sword that may become a problem in terms of waste disposal if used in large enough quantities[129]. Also, ^{225}Ac low availability makes clinical trials rather difficult[69].

^{212}Pb ($T_{1/2}$=10.6 hours) medium length half-life negates this problem and its more commonly available by ^{224}Ra ($T_{1/2}$=3.6 days) generators which are rather convenient for clinical sites since a single generator can be used for a couple weeks[14]. Unlike ^{225}Ac and ^{227}Th, ^{212}Pb has a theranostic pair, ^{203}Pb ($T_{1/2}$=2.2 days) which can be imaged via SPECT imaging allowing treatment planning and accurate dosimetry[23]. Unfortunately, the common method of eluting ^{224}Ra/^{212}Pb generators requires running high concentrations of hydrochloric acid through the cation exchange column (which separates the ^{212}Pb from the ^{224}Ra) which yields rather pure ^{212}Pb (^{224}Ra breakthrough is typically less than 1 ppm) in an unfavorable electrolytic solution for radiolabeling[14,128]. Because of this, it is required to evaporate the ^{212}Pb solution down to a residue and then redissolve the residue in a more favorable matrix before radiolabeling. Moreover, targeted radiopharmaceuticals commonly use the chelator TCMC which requires incubating at elevated temperatures in order to ensure quantitative radiolabeling[123,128]. All of these steps including quality control can take several hours to produce the targeted radiopharmaceutical which can limit the amount of activity that can be administered to the patient.

Herein, an elution method of using a 1.0 M sodium acetate and a Pb selective column is applied to a ^{224}Ra/^{212}Pb generator[125]. This method circumnavigates the need for the evaporation and redissolution steps and allows for direct labeling of the targeting vector since the sodium acetate matrix is more favorable. This method is tested by labeling TCMC conjugated Trastuzumab with the ^{212}Pb from the 1.0 M sodium acetate method and from the evaporation and redissolution with 0.1 M hydrochloric acid and 0.1 M nitric acid over two labeling trials over two weeks. The metrics used to compare each of the methods are radiochemical yield and radiochemical purity (see Appendix A).

5.2 Materials and methods

5.2.1 Materials

The following chemicals were used as received from chemical suppliers: Trastuzumab (Absolute Antibody), S-2-(4-Isothiocyanatobenzyl)-1,4,7,10-tetraaza-1,4,7,10-tetra(2-carbamoylmethyl)cyclododecane (p-SCN-Bn-TCMC; Macrocyclics), sodium bicarbonate (NaHCO3; Ward's Science), hydrochloric acid optima (HCl; Fisher Scientific), nitric acid optima (HNO_3; Fisher Scientific), sodium acetate trihydrate (NaOAc; VWR), L-ascorbic acid (ascorbic acid; Sigma-Aldrich), 1x sterile phosphate buffered saline (PBS, VWR), ammonium acetate (NH_4OAc; Fluka), 0.9% sterile saline (saline; APP Pharmaceuticals), Ethylenediaminetetraacetic acid disodium salt dihydrate (EDTA; VWR), and Dimethyl sulfoxide (DMSO; Amresco). All solutions were prepared with deionized water purified by a Millipore Milli-Q water purification system. The 2 mL 50-100 micron lead resin cartridges were purchased from Eichrom Technologies, Inc.

5.2.2 Antibody conjugation

Conjugation of Trastuzumab antibodies occurred through covalent coupling of p-SCN-Bn-DOTA to the lysine residues of the antibodies[155]. In brief, known masses of Trastuzumab were buffer-exchanged into 0.1 M $NaHCO_3$ using 0.5 mL 30 kDa Amicon Ultra Centrifugal Filter Units (Millipore Sigma). Trastuzumab was then incubated with p-SCN-Bn-TCMC for 60 min at 37 °C in a DMSO matrix at a 1:40 molar ratio. The resulting solution was buffer-exchanged into 0.2 M NH_4OAc for radiolabeling.

5.2.3 ^{224}Ra/^{212}Pb generator elution

The 89.5 MBq ^{224}Ra/^{212}Pb generator that was used for this study was designed by, produced by, and shipped to Lawrence Berkeley National Laboratory by the Nuclear Chemistry and Engineering technical group at Pacific Northwest National Laboratory. The generator was eluted by two different methods two times over two weeks.

The first method used was based on a procedure described by Baidoo, et al[128]. In brief, ^{212}Bi (the daughter of ^{212}Pb) can be removed by washing the generator with 1 mL of 0.5 M HCl. From there, ^{212}Pb can be eluted by washing the column twice with 250 µL of 2.0 M HCl followed by 250 µL of Milli-Q water. Two separate aliquots of the total solution were taken, and both were evaporated down (using a stirring and hot plate) to a ^{212}Pb-chloride residue. One of the residues was dissolved into 8.0 M HNO_3 and subsequently evaporated down to a ^{212}Pb-nitrate residue. Finally, the ^{212}Pb-chloride residue was redissolved using 0.1 M HCl, and the ^{212}Pb-nitrate residue was redissolved using 0.1 M HNO_3. Both of these solutions were then used for radiolabeling

The second method uses 1.0 M NaOAc and a Pb selective column. The 2 mL 50-100 micron lead resin cartridge is attached to the end of the ^{224}Ra column. 1 mL of 2.0 M HCl is then pushed through the generator which causes the majority of the ^{212}Pb to be at the top of the lead resin. The lead resin is then detached from the generator, flipped upside down, and reattached again to the end of the generator. 1.0 M NaOAc is then pushed through the generator to collect the ^{212}Pb in a 1.0 M NaOAc matrix. This solution can then be assayed and prepared for radiolabeling.

5.2.4 ^{212}Pb radiolabeling

After elution, the three ^{212}Pb solutions (in 0.1 M HCl, 0.1 M HNO_3, or 1.0 M NaOAc) were used to label TCMC-conjugated Trastuzumab antibodies in order to compare the three methods. These radiolabeling experiments were performed twice over two weeks to emulate a fractionated radiotherapy therapy study that is commonly performed in the Bioactinide Chemistry Group. The radiolabeling procedures employed were also adapted from Baidoo, et al (which described the labeling of TCMC-conjugated Trastuzumab with ^{212}Pb in a 0.1 M HNO_3 matrix)[128].

For both the 0.1 M HCl ^{212}Pb solution and the 0.1 M HNO_3 solution, the pH was adjusted to 5.0-5.5 by adding 1 part 5 M NH_4OAc to 10 part acid (volume-wise). In addition, 220 mg/ml of ascorbic acid was also added as a radioprotectant in a 1 part ascorbic acid to 10 part acid ratio (volume-wise). A known mass of TCMC-conjugated Trastuzumab in a 0.2 M NH_4OAc matrix was then added to each ^{212}Pb solution. For the 0.1 M HCl ^{212}Pb solution, 10 µg of trastuzumab was added during week 1 while 26.7 µg of trastuzumab was added during week 2 (Table 5.1). For the 0.1 M HNO_3 solution, 10 µg of trastuzumab was added during week 1 while 25.2 µg of Trastruzumab was added during week 2. Both reaction solutions were then heated at 37 °C for 1 hour, and the reactions were quenched by the addition of 50 mM EDTA in a 2 part EDTA to 125 part acid ratio (volume-wise). The solutions were then buffer-exchanged into saline using 0.5 mL 30 kDa Amicon Ultra centrifugal filter units to remove unlabeled metal.

For the 1.0 M NaOAc ^{212}Pb solution, just 220 mg/ml of ascorbic acid was added in a 1 part ascorbic acid to 10 part NaOAc ratio (volume-wise) in order to reach the desired pH (5.0-5.5) and to serve as a radioprotectant. A known mass of TCMC-conjugated Trastuzumab in a 0.2 M NH_4OAc matrix was then added to the ^{212}Pb solution (10 µg during week 1 and 25.2 µg during week 2) (Table 5.1). The reaction solution was then heated at 37 °C for 1 hour, and the reaction was then quenched by the addition of 50 mM EDTA in a 2 part EDTA to 125 part NaOAc ratio (volume-wise). The solution was then buffer-exchanged into saline using 0.5 mL 30 kDa Amicon Ultra centrifugal filter units to remove unlabeled metal.

Table 5.1: Mass of Trastuzumab added for each labeling trial.

Week	0.1 M HCl	0.1 M HNO3	1.0 M NaOAc
1	10 µg	10 µg	10 µg
2	26.7 µg	25.2 µg	25.2 µg

Activities of the ^{212}Pb solutions were determined by gamma spectroscopy via a P-Type High Purity Germanium gamma spectrometer using the 238.63 keV line. The radiochemical yields were determined by measuring the activity of ^{212}Pb that stayed at the top of the 30 kDa filter (the labeled ^{212}Pb) and the activity of ^{212}Pb that was in the filtrate (the unlabeled ^{212}Pb). The radiochemical yield is then calculated by the ratio of labeled radiometal to the sum of labeled radiometal and unlabeled radiometal. The radiochemical purities of radiolabeled antibody drug conjugate solutions were determined by radio-ITLC (Bioscan System 200 Imaging Scanner), using Supelco ITLC-SG glass plates (Sigma-Aldrich) and 20 mM EDTA at pH 5.5 as the mobile phase. Radiochemical purities were determined by drawing two regions of interest (using Bioscan System 200 Imaging Scanner software) over the gaussian peak at the origin

(which contains the labeled antibodies) and the region outside the origin peak (which constitutes unlabeled radiometal. The radiochemical purity is then calculated by the ratio of labeled radiometal to the total amount of radiometal on the plate.

5.3 Results

For the 0.1 M HCl labeling trials, the activity of ^{212}Pb per microgram of antibody incubation was 58.8 kBq/µg for week 1 (588.0 kBq of ^{212}Pb and 10 µg of Trastuzumab) and was 25.5 kBq/µg for week 2 (680.9 µCi of ^{212}Pb and 26.7 µg of Trastuzumab) (Table 5.2). The radiochemical yield was consistently low at 17.66% for week 1 and 19.18% for week 2 (Table 5.2). Table 5.2 also contains the radiochemical yield per microgram of antibody in order to normalize the radiochemical with respect to the amount of antibody added for each trial. For this trial, this quantity was 1.77 %/µg for week 1 and was 0.72 %/µg for week 2. Radiochemical purity was determined by radio-ITLC where the antibody drug conjugate stayed at the origin and the free metal moved up the plate with the solvent front and formed a double peak (one peak for ^{212}Pb and another peak for ^{212}Bi) (Fig. 5.1B and Fig. 5.1D). Radiochemical purity (Table 5.3) stayed consistent over both weeks with 85.5% at week 1 (Fig. 5.1A) and 80.3% at week 2 (Fig. 5.1C).

Table 5.2: Activity of ^{212}Pb per microgram of antibody, radiochemical yield, and radiochemical yield per microgram of antibody for each labeling trial.

	0.1 M HCl			0.1 M HNO_3			1.0 M NaOAc		
Week	A/µg[a] (kBq/µg)	RCY[b] (%)	RCY/µg[c] (%/µg)	A/µg (kBq/µg)	RCY (%)	RCY/µg (%/ug)	A/µg (kBq/ug)	RCY (%)	RCY/µg (%/µg)
1	58.8	17.66	1.77	75.5	28.69	2.87	170.9	75.41	7.54
2	25.5	19.18	0.72	22.2	26.83	1.06	8.9	88.65	3.52

[a]A/µg is the activity of ^{212}Pb per microgram of antibody at the time of antibody incubation
[b]RCY is radiochemical yield
[c]RCY/µg is the radiochemical yield per microgram of antibody

Table 5.3: Radiopurity of ^{212}Pb-TCMC-Trastuzumab for each labeling trial.

Week	0.1 M HCl	0.1 M HNO3	1.0 M NaOAc
1	85.5%	88.8%	85.8%
2	80.3%	93.2%	88.2%

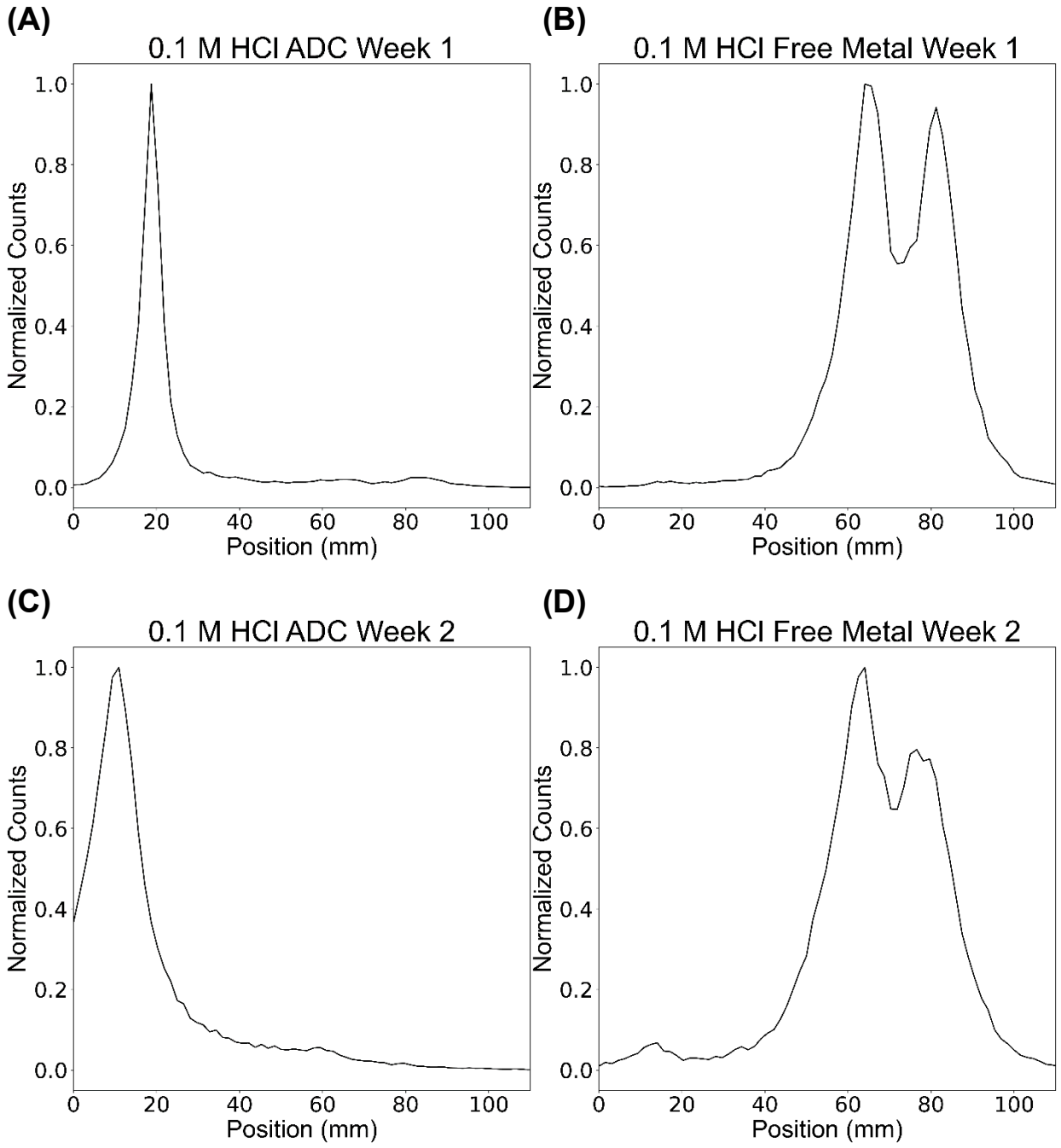

Figure 5.1: Radio-ITLC traces of (A) ^{212}Pb-TCMC-Trastuzumab during week 1's labeling experiments, (B) free ^{212}Pb during week 1's labeling experiments, (C) ^{212}Pb-TCMC-Trastuzumab during week 2's labeling experiments, and (D) free ^{212}Pb during week 2's labeling experiments after reconstituting the lead residue in 0.1 M HCl.

For the 0.1 M HNO_3 labeling trial, the activity of ^{212}Pb per microgram of antibody incubation was 75.5 kBq/µg for week 1 (755.0 kBq of ^{212}Pb and 10 µg of Trastuzumab) and was 22.2 kBq/µg for week 2 (559.4 kBq of ^{212}Pb and 25.2 µg of Trastuzumab) (Table 5.2). The radiochemical yield was slightly higher than the 0.1 M HCl labeling trial

at 28.69% for week 1 and 26.83% for week 2 (Table 5.2). The radiochemical yield per microgram of antibody was 2.87 %/μg for week 1 and was 1.06 %/μg for week 2 (Table 5.2). Radiochemical purity (Table 5.3) was determined by radio-ITLC where the antibody drug conjugate stayed at the origin and the free metal moved up the plate with the solvent front and formed a double peak (one peak for ^{212}Pb and another peak for ^{212}Bi) (Fig. 5.2B and Fig. 5.2D). Radiochemical purity stayed consistent over both weeks with 88.8% at week 1 (Fig. 5.2A) and 93.2% at week 2 (Fig. 5.2C).

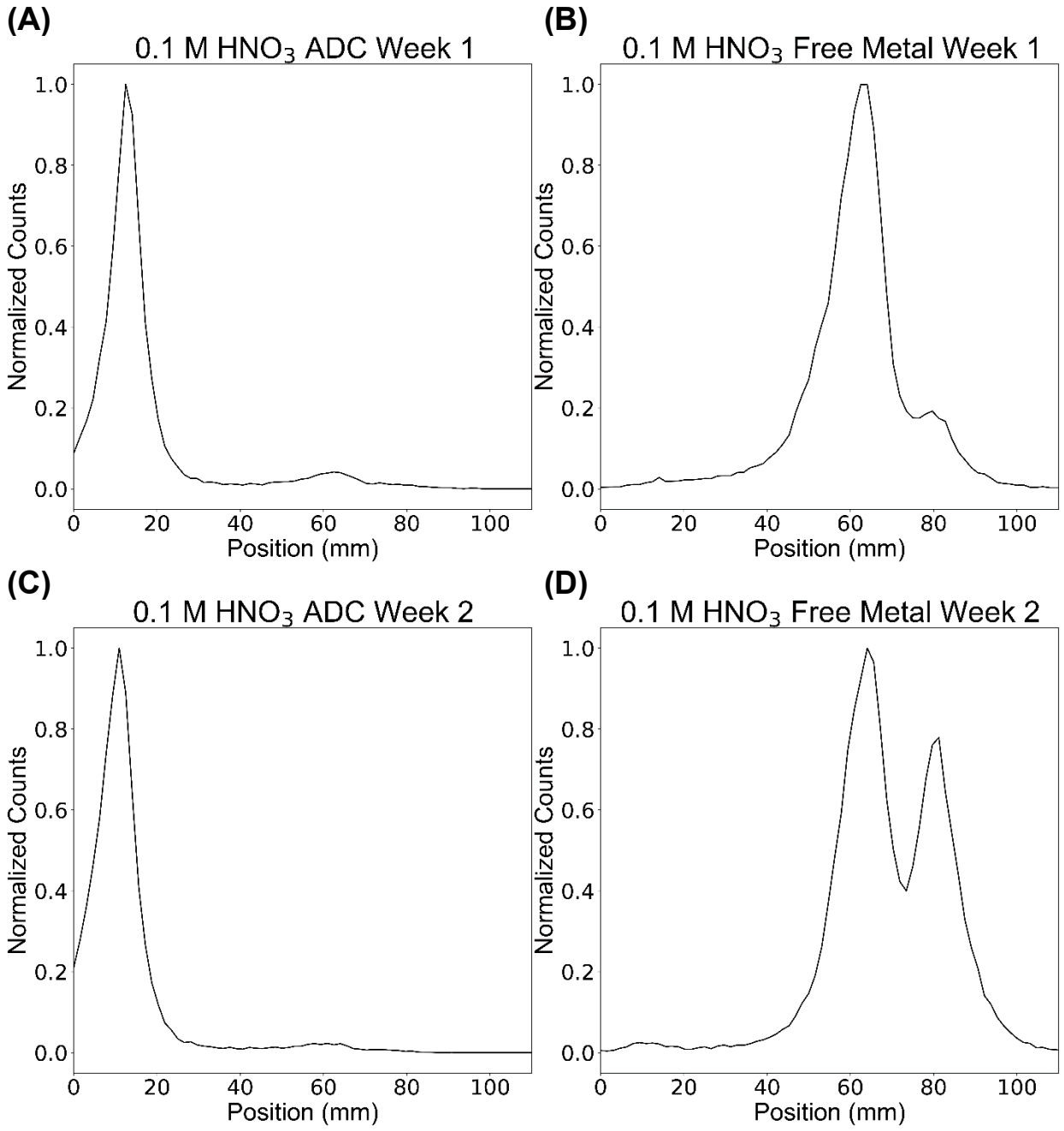

Figure 5.2: Radio-ITLC traces of (A) ^{212}Pb-TCMC-Trastuzumab during week 1's labeling experiments, (B) free ^{212}Pb during week 1's labeling experiments, (C) ^{212}Pb-TCMC-Trastuzumab during week 2's labeling experiments, and (D) free ^{212}Pb during week 2's labeling experiments after reconstituting the lead residue in 0.1 M HNO_3.

For the 1.0 M NaOAc labeling trial, the activity of ^{212}Pb per microgram of antibody incubation was 170.9 kBq/μg for week 1 (1709.0 kBq of ^{212}Pb and 10 μg of Trastuzumab) and was 8.9 kBq/μg for week 2 (224.3 kBq of ^{212}Pb and 25.2 μg of Trastuzumab) (Table 5.2). The radiochemical yield was dramatically higher than the other labeling trials at 75.41% for week 1 and 88.65% for week 2 (Table 5.2). The

radiochemical yield per microgram of antibody was 7.54 %/µg for week 1 and was 3.52 %/µg for week 2 (Table 5.2). Radiochemical purity (Table 5.3) was determined by radio-ITLC where the antibody drug conjugate stayed at the origin and the free metal moved up the plate with the solvent front and formed a double peak (one peak for ^{212}Pb and another peak for ^{212}Bi) (Fig. 5.3B and Fig. 5.3D). Radiochemical purity stayed consistent over both weeks with 85.8% at week 1 (Fig. 5.2A) and 88.2% at week 2 (Fig. 5.2C).

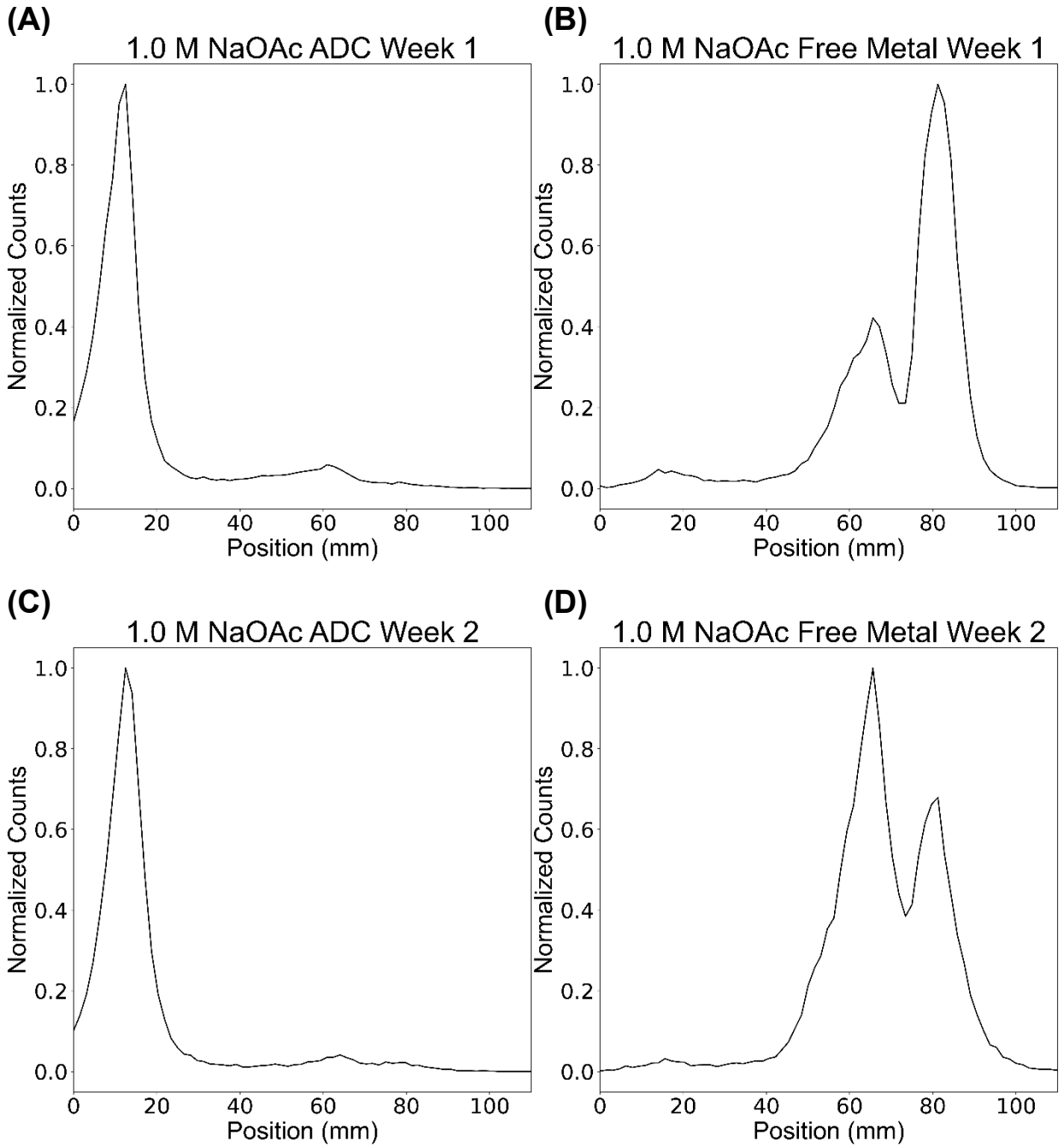

Figure 5.3: Radio-ITLC traces of (A) ^{212}Pb-TCMC-Trastuzumab during week 1's labeling experiments, (B) free ^{212}Pb during week 1's labeling experiments, (C) ^{212}Pb-TCMC-Trastuzumab during week 2's labeling experiments, and (D) free ^{212}Pb during week 2's labeling experiments after eluting the generator with 1.0 M NaOAc.

5.4 Discussion

One of the benefits of the 1.0 M NaOAc method is that it circumvents the need for the evaporation and redissolution step. The evaporation step alone takes anywhere from 1 to 1.5 hours. Removing this step can minimize the loss of activity due to decay

and process loss during the extra steps. In addition, for both of the weeks, the radiochemical yield was substantially higher for the NaOAc method compared to the other 2 methods. The radiochemical yields for the 0.1 M HCl and 0.1 M HNO_3 trials were considerably lower than what has been reported[128]. Adding more antibody the second week only slightly increased the radiochemical yield for the 0.1 M HCl trial but decreased for the 0.1 M HNO_3 trials. One other possibility is that the pH of the solution before antibody addition needed to be brought even higher by adding more 5 M NH_4OAc.

Another reason for increasing the amount of antibodies for the second week is that in previous studies involving TCMC conjugated antibodies incorporating ^{212}Pb in the Bioactinide Chemistry Group, the radiochemical yield and radiochemical purity dramatically decreased during the second week of using the $^{224}Ra/^{212}Pb$ generator. It is suspected that this labeling degradation is due to the radiolytic break down of the cation exchange column, and this led to the formation of ^{212}Pb complexes with organic molecules from the column which outcompeted TCMC[14,133,138]. In the future, this hypothesis will be verified using mass spectrometry.

It is common during running radio-TLC for ^{212}Pb to allow the plate to decay over 24 hours in order for all the free ^{212}Bi ($T_{1/2}$= 1.0 hours) to decay and for the remaining ^{212}Pb and ^{212}Bi to reach secular equilibrium[125]. While this leads to more accurate results (radio-ITLC typically can't distinguish between ^{212}Pb and ^{212}Bi), this isn't feasible if being used as a quality control procedure to determine whether a dose will be administered to the patient. For this study in order to emulate a typical preclinical study, the plate was ran right after radiolabeling. This leads to a double peak where the free metal is located where one peak is ^{212}Pb and the other peak is ^{212}Bi. While radio-TLC is not able to determine which peak is which and thus limits the accuracy of this measurement, high performance liquid chromatography could be collecting fractions of the mobile phase and counting each fraction using gamma spectrometry to determine the radionuclide composition in each fraction which would allow for more accurate quality control before administration. If the plate was allowed to decay in place for 24 hours getting rid of the free ^{212}Bi peak, the radiochemical purity would be higher since the free ^{212}Bi peak contributes to the degradation of the radiochemical purity.

While the 1.0 M NaOAc elution method was first demonstrated using a $^{228}Th/^{212}Pb$ generator, this study demonstrates that this method is also compatible with $^{224}Ra/^{212}Pb$ generators. While $^{228}Th/^{212}Pb$ can be used for much longer periods of time because of the 1.9 year half-life of ^{228}Th, the generators are known to break down over time and leading to more and more ^{228}Th breakthrough[14,133,138]. While the $^{224}Ra/^{212}Pb$ generator is only usable for up to two weeks due to the shorter half-life of ^{224}Ra and is only typically available with up to 740 MBq of ^{224}Ra, there is minimal ^{224}Ra breakthrough, which is acceptable for clinical trials. This new elution method could potentially facilitate future clinical trials.

While TCMC has been the most commonly used chelator for ^{212}Pb, its slower binding kinetics also make the logistics of prepping ^{212}Pb-based targeted radiopharmaceuticals challenging. The hydroxypyridinone-based 3,4,3-LI(1,2-HOPO) could potentially allow for highly stable lead complexes and the ability to rapidly bind lead at room temperature[32]. While HOPO may form more stable complexes with tetravalent metal cations compared to divalent metal cations, limiting the radiolabeling

time through 3,4,3-LI(1,2-HOPO) could minimize activity loss potentially allowing for the treatment of more patients.

5.5 Conclusions

Herein, it was demonstrated that the elution of ^{224}Ra/^{212}Pb generators with 1.0 M NaOAc both minimizes the time to fabricate targeted radiopharmaceuticals and maintains a high radiochemical yield and radiochemical purity over two weeks. Incorporation of this strategy could advance ^{212}Pb/^{203}Pb theranostics and facilitate clinical studies Future work will investigate ^{212}Pb-3,4,3-LI(1,2-HOPO) complexes and incorporate ^{212}Pb into siderocalin fusion proteins[32,36,148,149].

CHAPTER 6: Delivering ^{225}Ac and ^{90}Y through non-covalent interactions of small molecule ligands with siderocalin fusion proteins

6.1 Introduction

One of the key components of a targeted radiopharmaceutical is the chelator which is responsible for binding the therapeutic and diagnostic radiometal with high *in vivo* stability. If the chelator releases the radiometal *in vivo*, the metal could potentially redistribute to a healthy organ and unnecessary dose it potentially leading to radiotoxicity and second cancers[26,27]. The ideal chelator for theranostic applications would have high *in vivo* stability, allow for rapid room temperature radiolabeling, and be compatible with a wide variety of metal cations. This last point would facilitate the further modularization of targeted radiopharmaceuticals: easily allowing the radiometal to be swapped to another radiometal in a targeted radiopharmaceutical without changing the chelator.

Several strategic radiometals for theranostic applications are trivalent and tetravalent actinides ($^{225}Ac^{III}$ and $^{227}Th^{IV}$) and rare earth metals ($^{86}Y^{III}$, $^{90}Y^{III}$, $^{44}Sc^{III}$, $^{47}Sc^{III}$, $^{132}La^{III}$, $^{133}La^{III}$, $^{134}Ce^{III}$, $^{149}Tb^{III}$, $^{155}Tb^{III}$, $^{152}Tb^{III}$, $^{161}Tb^{III}$, and $^{177}Lu^{III}$)[21,78,84,85,120,158–160]. In the past, chelation of actinides for the application of decorporation has been focused on siderophore derivatives, which are a class of molecules that are typically produced by bacteria or fungi and used to traffic Fe^{III} to them[31]. A siderophore-derived chelator with hydroxypyridinone moieties, 3,4,3-LI(1,2-HOPO), has been shown to rapidly bind both trivalent and tetravalent actinides and rare earth metals with higher selectivity compared to divalent endogenous metals[30,32,33].

While 3,4,3-LI(1,2-HOPO) (referred to now as HOPO) has been bifunctionalized as p-SCN-Bn-HOPO, conjugated to Trastuzumab, and labeled with ^{89}Zr in order to image BT474 tumor bearing mice, the synthesis process is challenging and has low yield prompting the need to investigate other means of linking HOPO to targeting vectors[36,161]. One potential option is to use the mammalian 24 kDa Siderocalin protein. Siderocalin has been shown to be part of the innate immune system where it binds through electrostatic interactions with the negatively charged $[Fe^{III}$-enterobactin$]^{-3}$ complex where enterobactin is a hexadentate siderophore produced by *Escherichia coli* and *Salmonella typhimurium*[41]. Interestingly, If the iron is swapped with a trivalent or tetravalent actinide or rare earth metal, siderocalin will still bind rather strongly with the complex[42]. Furthermore, swapping enterobactin with HOPO allows for the same electrostatic binding if the metal is a trivalent cation because HOPO trivalent metal complexes have a charge of negative 1[42]. If a HOPO is bound to a tetravalent metal cation, the complex that is formed is neutral and is not recognized by Siderocalin. This non-covalent interaction could potentially be used as a linker to bind M^{III}-HOPO complexes to a targeting vector if the targeting vector incorporates Siderocalin's binding pocket.

In order to investigate this hypothesis, Siderocalin-Trastuzumab fusion proteins were developed (Fig. 6.1). These fusion proteins have the functionality of both the original proteins, Siderocalin's ability to tightly bind negatively charged HOPO

complexes and Trastuzumab's ability to selectively bind to the HER2+ protein, allowing them to be used for targeted radiopharmaceuticals[148,149]. Two different fusion proteins were developed: Siderocalin-Trastuzumab-IgG (Fig. 6.2(A)) which contains two siderocalin proteins allowing for the binding of 2 $[M^{III}\text{-HOPO}]^{-1}$ complexes and Siderocalin-Trastuzumab-Fab (Fig. 6.2(B)) which contains one Siderocalin protein allowing for the binding of 1 $[M^{III}\text{-HOPO}]^{-1}$ complex.

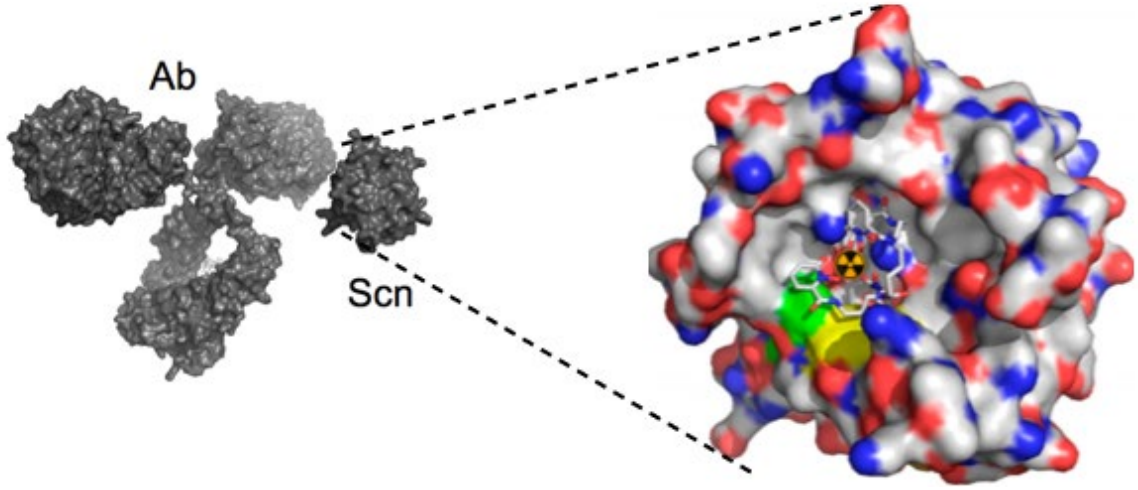

Figure 6.1: The chemical structure of the Siderocalin-Trastuzumab fusion protein. Ab is antibody, and Scn is Siderocalin.

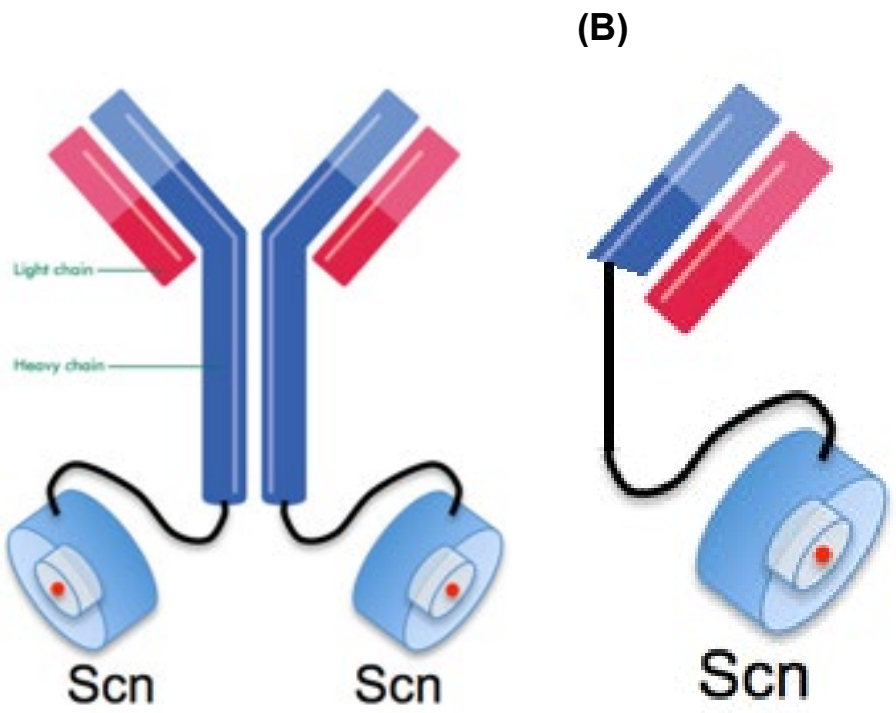

Figure 6.2: A schematic of (A) Siderocalin-Trastuzumab-IgG and (B) Siderocalin-Trastuzumab-Fab. Siderocalin-Trastuzumab-IgG has two Siderocalin proteins while Siderocalin-Trastuzumab-Fab only has one Siderocalin protein. Scn is Siderocalin.

Herein, the *ex vivo* biodistribution of ^{90}Y and ^{225}Ac bound to both of these fusion proteins in SK-OV-3 tumor bearing NOD SCID mice is investigated. In addition, a tumor control efficacy study is performed with both of these therapeutic radionuclides.

6.2 Materials and methods

All procedures and protocols used in these studies were reviewed and approved by the Institutional Animal Care and Use Committee of LBNL and were performed in AAALAC-accredited facilities, according to prescribed guidelines and regulations. Intraperitoneal (IP) injections and euthanasia by cervical dislocation were performed under isoflurane anesthesia.

6.2.1 Materials

The following chemicals were used as received from chemical suppliers: Yttrium-90 (^{90}Y; Eckert & Ziegler), hydrochloric acid optima (HCl; Fisher Scientific), 1x sterile phosphate buffered saline (PBS, VWR), 0.9% sterile saline (saline; APP Pharmaceuticals), 3,4,3-LI(1,2-HOPO) (HOPO; Ash Stevens), Ethylenediaminetetraacetic acid disodium salt dihydrate (EDTA; VWR), 40-86% Nitric Acid (HNO_3; Sigma-Aldrich), Dimethyl sulfoxide (DMSO; Amresco), and Matrigel matrix (Matrigel; VWR). The wild-type Siderocalin proteins were produced as previously described by Roland Strong's laboratory at Fred Hutchinson Cancer Research Center[41]. Also, the Siderocalin fusion proteins were produced at the beforementioned lab. Generator-produced ^{225}Ac was received from the National Isotope Development Center at Oak Ridge National Laboratory as ^{225}Ac trichloride[69]. All solutions were prepared with

deionized water purified by a Millipore Milli-Q water purification system. SK-OV-3 cells were used as received from ATCC.

6.2.2 ^{225}Ac radiolabeling

Radiolabeling of the fusion proteins with ^{225}Ac was performed by Dr. Korey Carter while gamma spectroscopy was performed by me. ^{225}Ac trichloride was dissolved in 0.05 N of HCl. 3 aliquots of the ^{225}Ac solution were added to pre-prepared PBS solutions containing HOPO in DMSO in a 100:1 ligand to metal ratio. The solution was mixed thoroughly by pipetting up and down and then allowed to incubate for 1 hour at 60 degrees Celsius. Afterwards, the solutions were then added to either wild-type Siderocalin proteins (200:1 protein to metal ratio), Siderocalin-Trastuzumab-IgG proteins (100:1 protein to metal ratio), or Siderocalin-Trastuzumab-Fab proteins (200:1 protein to metal ratio) in a PBS matrix. These solutions were mixed thoroughly by pipetting up and down and then were allowed to incubate for 5 minutes at room temperature. The solutions were then buffer-exchanged into saline using 0.5 mL 10 kDa Amicon Ultra centrifugal filter units to remove unlabeled metal and then diluted for animal injection. A cold HOPO-Siderocalin-Trastuzumab-IgG solution was prepared as a negative control with the same procedure minus the ^{225}Ac.

Activities of the injection solutions were determined by gamma spectroscopy via a P-Type High Purity Germanium gamma spectrometer using the 218.00 keV line of ^{221}Fr. Before counting, samples were allowed to sit at rest for more than 1 hour prior to measurements to allow ^{221}Fr to reach secular equilibrium with ^{225}Ac, allowing the ^{221}Fr activity to be equivalent to ^{225}Ac. The radiochemical yields were determined by measuring the activity of ^{225}Ac that stayed at the top of the 10 kDa filter (the labeled ^{225}Ac) and the activity of ^{225}Ac that was in the filtrate (the unlabeled ^{225}Ac). The radiochemical yield is then calculated by the ratio of labeled radiometal to the sum of labeled radiometal and unlabeled radiometal.

6.2.3 ^{90}Y radiolabeling

6 aliquots (3 for biodistribution experiments and 3 for therapy experiments) of ^{90}Y in a 0.04 N HCl matrix were added to pre-prepared PBS solutions containing HOPO in DMSO in a 100:1 ligand to metal ratio. The solution was mixed thoroughly by pipetting up and down, and then allowed to incubate for 5 minutes at room temperature. Afterwards, the solutions were then added to either wild-type Siderocalin proteins (200:1 protein to metal ratio), Siderocalin-Trastuzumab-IgG proteins (100:1 protein to metal molar ratio), or Siderocalin-Trastuzumab-Fab proteins (200:1 protein to metal molar ratio) in a PBS matrix. These solutions were mixed thoroughly by pipetting up and down and then were allowed to incubate for 5 minutes at room temperature. The solutions were then diluted for animal injection.

Activities of the injection solutions were measured by Liquid Scintillation Counting (Packard Tri-Carb model B4430, Perkin Elmer), using a 20 – 2000 keV window and Ultima Gold LLT. The radiochemical purities of radiolabeled antibody drug conjugate solutions were determined by radio-ITLC (Bioscan System 200 Imaging Scanner), using Supelco ITLC-SG glass plates (Sigma-Aldrich) and 20 mM EDTA at pH 5.5 as the mobile phase. Radiochemical purities were determined by drawing two regions of interest (using Bioscan System 200 Imaging Scanner software) over the gaussian peak

at the origin (which contains the labeled proteins and ^{90}Y-HOPO) and the region outside the origin peak (which constitutes unlabeled radiometal). Because both ^{90}Y-HOPO bound to protein and ^{90}Y-HOPO unbound to protein stayed at the origin, this radiochemical purity measurement does not distinguish between the two cases (this is discussed further in Section 6.4). The radiochemical purity is then calculated by the ratio of labeled radiometal to the total amount of radiometal on the plate. The radiochemical purities were measured immediately, 1 day, and 3 days after solution prep in order to determine if the purity degraded overtime *in vitro.*

6.2.4 ^{225}Ac labeled fusion protein biodistribution and tumor control studies

Ex vivo biodistribution and tumor control studies were performed in SK-OV-3 tumor-bearing (0.28 ± 0.04 cm^3), adult female NOD SCID mice (13 weeks; 23.9 ± 2.3 g; Charles River, CA) to evaluate the tumor targeting capability and the tumor control efficacy of the ^{225}Ac labeled fusion proteins. The SK-OV-3 tumors were passaged in NOD SCID mice and prepared as single-cell suspensions (10^6 cells) in 50% Matrigel prior to subcutaneous transplantation in the right mammary fat pad of NOD SCID mice under isoflurane anesthesia.

For the biodistribution study, groups of 3 mice were injected intraperitoneally with a single dose of either 0.2 mL ^{225}Ac-HOPO-Siderocalin (3784.1 ± 51.5 Bq, 39.2 pM), 0.2 mL ^{225}Ac-HOPO-Siderocalin-Trastuzumab-IgG (333 ± 33.5 Bq, 3.4 pM), or 0.2 mL ^{225}Ac-HOPO-Siderocalin-Trastuzumab-Fab (59.2 ± 2.3 Bq, 0.6 pM). Molarities of the antibodies, ligands, and the metals in each injection dose are included in Table 6.1. At 24 hours after administration, mice were euthanized by cervical dislocation and then dissected. For each mouse, kidneys, liver, spleen, and tumor were dissected, and the abdominal remainder tissue (ART, which includes the (GI) tract, reproductive organs, urinary bladder, and abdominal fat) was removed. Feces samples were separated manually from urine-stained cellulose bedding and treated as group samples (each group had their own cage). The organ samples and the partially eviscerated carcasses were managed as individual samples. All samples were dried at 100 °C, dry-ashed at 575 °C, and dissolved in concentrated nitric acid. The ashed-soft tissue in the carcass was rinsed from the ashed-bone with HNO_3 and both soft tissue, bone, feces, and urine were diluted with water into polyethylene bottles. The dissolved organs, 2 g aliquots of the soft tissue, bone, feces, and urine, and 2 mL aliquots of standard solutions were mixed with 10 mL of Ultima Gold LLT (Perkin Elmer, Shelton) for counting by liquid scintillation counting (Packard Tri-Carb model B4430, Perkin Elmer) using a window of 50 keV-2000 keV with the results being reported in terms of percent injected activity per gram of tissue (%IA/g).

For the tumor control study, groups of 4 mice were injected intraperitoneally with a single dose of either 0.2 mL cold HOPO-Siderocalin-Trastuzumab-IgG, 0.2 mL ^{225}Ac-HOPO-Siderocalin (3784.1 ± 51.5 Bq, 39.2 pM), 0.2 mL ^{225}Ac-HOPO-Siderocalin-Trastuzumab-IgG (333.0 ± 33.5 Bq, 3.4 pM), 0.4 mL ^{225}Ac-HOPO-Siderocalin-Trastuzumab-IgG (603.0 ± 22.8 Bq, 3.1 pM), or 0.2 mL ^{225}Ac-HOPO-Siderocalin-Trastuzumab-Fab (59.2 ± 2.3 Bq, 0.6 pM). Molarities of the proteins, ligands, and the metals in each injection dose are included in Table 6.1. Mice were checked daily for signs of distress, and weights and tumor volumes were measured twice a week. Mice were euthanized by cervical dislocation if tumor volumes were larger than 1000 mm^3 for

two consecutive measurements, lost more than 15% of their original body mass at the time of drug administration, or if the tumor ulcerated.

Table 6.1: Protein molarity, ligand Molarity, goal ^{225}Ac molarity, and actual ^{225}Ac molarity for the ^{225}Ac labeled fusion proteins injection solutions.

Injection Dose[a]	Protein Molarity	Ligand Molarity	Goal ^{225}Ac Molarity	Actual ^{225}Ac Molarity
HOPO-Siderocalin-Trastuzumab-IgG	7.7 nM	7.7 nM	N/A	N/A
^{225}Ac-HOPO-Siderocalin	15.3 nM	7.7 nM	76.6 pM	39.2 pM
^{225}Ac-HOPO-Siderocalin-Trastuzumab-IgG	7.7 nM	7.7 nM	76.6 pM	3.45 pM
^{225}Ac-HOPO-Siderocalin-Trastuzumab-IgG[b]	7.7 nM	7.7 nM	76.6 pM	3.12 pM
^{225}Ac-HOPO-Siderocalin-Trastuzumab-Fab	15.3 nM	7.7 nM	76.6 pM	0.6 pM

[a]Unless otherwise stated, the injection dose was 0.2 mL injected intraperitoneally.
[b]The injection dose was 0.4 mL injected intraperitoneally

6.2.5 ^{90}Y labeled fusion protein biodistribution and tumor control studies

Ex vivo biodistribution and tumor control studies were performed in SK-OV-3 tumor-bearing (0.04 ± 0.01 cm^3), adult female NOD SCID mice (10 weeks; 24.2 ± 1.4 g; Charles River, CA) to evaluate the tumor targeting capability and the tumor control efficacy of the ^{90}Y labeled fusion proteins. The SK-OV-3 tumors were passaged in NOD SCID mice and prepared as single-cell suspensions (10^6 cells) in 50% Matrigel prior to subcutaneous transplantation in the right mammary fat pad of NOD SCID mice under isoflurane anesthesia.

For the biodistribution study, groups of 3 mice were injected Intraperitoneally with a single 0.2 mL dose of either ^{90}Y-HOPO-Siderocalin (76.6 ± 0.4 kBq), ^{90}Y-HOPO-Siderocalin-Trastuzumab-IgG (74.1 ± 0.7 kBq), or ^{90}Y-HOPO-Siderocalin-Trastuzumab-Fab (49.3 ± 4.5 kBq). Molarities of the proteins, ligands, and the metals in each injection dose are included in Table 6.2. At 24 hours after administration, mice were euthanized by cervical dislocation and then dissected. For each mouse, kidneys, liver, spleen, femur, heart, and tumor were dissected, and the abdominal remainder tissue (ART, which includes the (GI) tract, reproductive organs, urinary bladder, and abdominal fat) was removed. All samples were dried at 100 °C, dry-ashed at 575 °C, and dissolved in concentrated nitric acid. The dissolved organs and 2 mL aliquots of standard solutions were mixed with 10 mL of Ultima Gold LLT (Perkin Elmer, Shelton) for counting by liquid scintillation counting (Packard Tri-Carb model B4430, Perkin Elmer) using a window of 50 keV-2000 keV with the results being reported in terms of percent injected activity per gram of tissue (%IA/g).

For the tumor control study, groups of 4 mice were injected intraperitoneally with a single 0.2 mL dose of either ^{90}Y-HOPO-Siderocalin (1.63 ± 0.03 MBq), ^{90}Y-HOPO-Siderocalin-Trastuzumab-IgG (1.65 ± 0.03 MBq), ^{90}Y-HOPO-Siderocalin-Trastuzumab-Fab (1.70 ± 0.03 MBq), or no treatment. Molarities of the proteins, ligands, and the metals in each injection dose are included in Table 6.2. Mice were checked daily for signs of distress, and weights and tumor volumes were measured twice a week. Mice were euthanized by cervical dislocation if tumor volumes were larger than 1000 mm^3 for two consecutive measurements, lost more than 15% of their original body mass at the time of drug administration, or if the tumor ulcerated.

Table 6.2: Protein molarity, ligand molarity, and ^{90}Y molarity for the ^{90}Y labeled fusion proteins.

Injection Dose[a]	Protein Molarity	Ligand Molarity	^{90}Y Molarity
Biodistribution			
^{90}Y-HOPO-Siderocalin	42.3 nM	21.2 nM	211.6 pM
^{90}Y-HOPO-Siderocalin-Trastuzumab-IgG	20.5 nM	20.5 nM	204.7 pM
^{90}Y-HOPO-Siderocalin-Trastuzumab-Fab	27.2 nM	13.6 nM	136.2 pM
Tumor Control			
^{90}Y-HOPO-Siderocalin	900.7 nM	450.4 nM	4.5 nM
^{90}Y-HOPO-Siderocalin-Trastuzumab-IgG	455.9 nM	455.9 nM	4.6 nM
^{90}Y-HOPO-Siderocalin-Trastuzumab-Fab	939.4 nM	469.7 nM	4.7 nM

[a]The injection dose was 0.2 mL injected intraperitoneally.

6.3 Results

6.3.1 Fusion proteins labeled with ^{225}Ac

The radiochemical yield was determined to be 17.7% for ^{225}Ac-HOPO-Siderocalin, 2.2% for ^{225}Ac-HOPO-Siderocalin-Trastuzumab, and 0.4% for ^{225}Ac-HOPO-Siderocalin-Fab. Because of the low yield, the goal doses for therapy (200 nCi for 0.2 mL injections and 400 nCi for 0.4 mL injections) were not able to be met. In addition, there was not enough activity to determine radiochemical purity using radio-ITLC.

Figure 6.3(A) and Figure 6.3(B) show the results of the *ex vivo* biodistribution 24 hours after administration of the constructs in terms of %IA/g and %IA respectively. Minimal tumor uptake is apparent in all three groups with 0.82 ± 0.36 %IA/g for ^{225}Ac-HOPO-Siderocalin (negative control), 2.97 ± 3.98 %IA/g for ^{225}Ac-HOPO-Siderocalin-Trastuzumab-IgG, and 0.97 ± 0.57 %IA/g for ^{225}Ac-HOPO-Siderocalin-Trastuzumab-

Fab indicated minimal tumor uptake. Furthermore, elevated uptake is apparent in the liver, spleen, and skeletal system for all three constructs which is indicative of the natural biodistribution of free ^{225}Ac. Interestingly, ^{225}Ac-HOPO-SCN-Fab has elevated uptake in the feces at 26.15 ± 0.32 %IA which could be due to the elimination pathway ^{225}Ac-HOPO not bound to the protein.

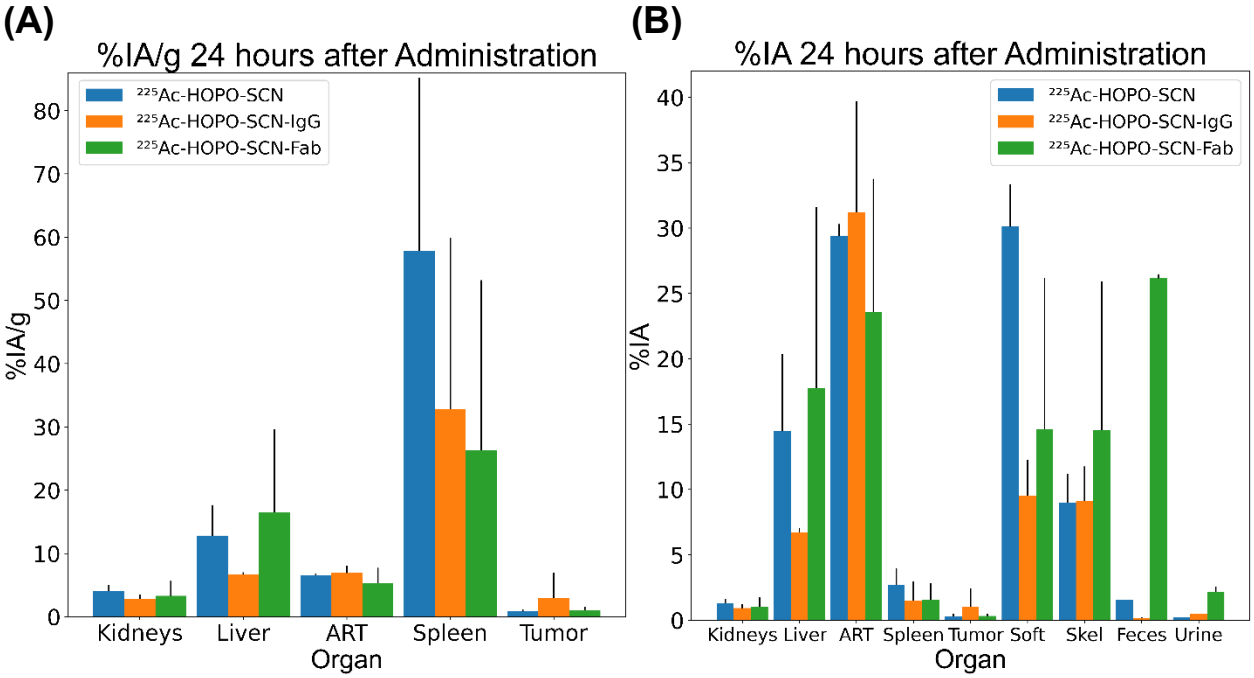

Figure 6.3: *Ex vivo* ^{225}Ac-HOPO-Siderocalin, ^{225}Ac-HOPO-Siderocalin-Trastuzumab-IgG, and ^{225}Ac-HOPO-Siderocalin-Trastuzumab-Fab biodistribution in SK-OV-3 tumor bearing NOD SCID mice in terms of (A) %IA/g and (B) %IA at 1 day after administration measured by liquid scintillation counting. Each data point is the average value of the 3 mice in each group, and the error bars represent the 1-sigma standard deviation. Only the upper error bar is displayed for ease of visualization. IgG is Trastuzumab-IgG, Fab is Trastuzumab-Fab, and SCN is Siderocalin. ART is abdominal remaining tissue. Skel is the entire skeletal system. Soft is the remaining soft tissue that was not already harvested.

The individual tumor growth curves are shown for all 5 treatment groups in Figure 6.4. The ^{225}Ac radiolabeled groups (3784.1 Bq of ^{225}Ac-HOPO-Siderocalin (Fig. 6.4(B)), 333.0 Bq of ^{225}Ac-HOPO-Siderocalin-Trastuzumab-IgG (Fig. 6.4(C)), 603 Bq of ^{225}Ac-HOPO-Siderocalin-Trastuzumab-IgG (Fig. 6.4(D)), and 59.2 Bq of ^{225}Ac-HOPO-Siderocalin-Trastuzumab-Fab (Fig. 6.4(E)) all follow a similar growth trend to the negative control HOPO-Siderocalin-Trastuzumab group in Figure 6.4(A). This similarity is also apparent in Figure 6.5(A) which shows the average tumor volume growth for each group is not statistically significantly different from one and other (notice the 1 standard deviation error bars all overlap). The mice seemed to tolerate the constructs well and did not lose more than %15 of their body mass on administration day. All the mice were euthanized early due to ulcerations in their tumors as shown in the survival curve in Figure 6.5(B).

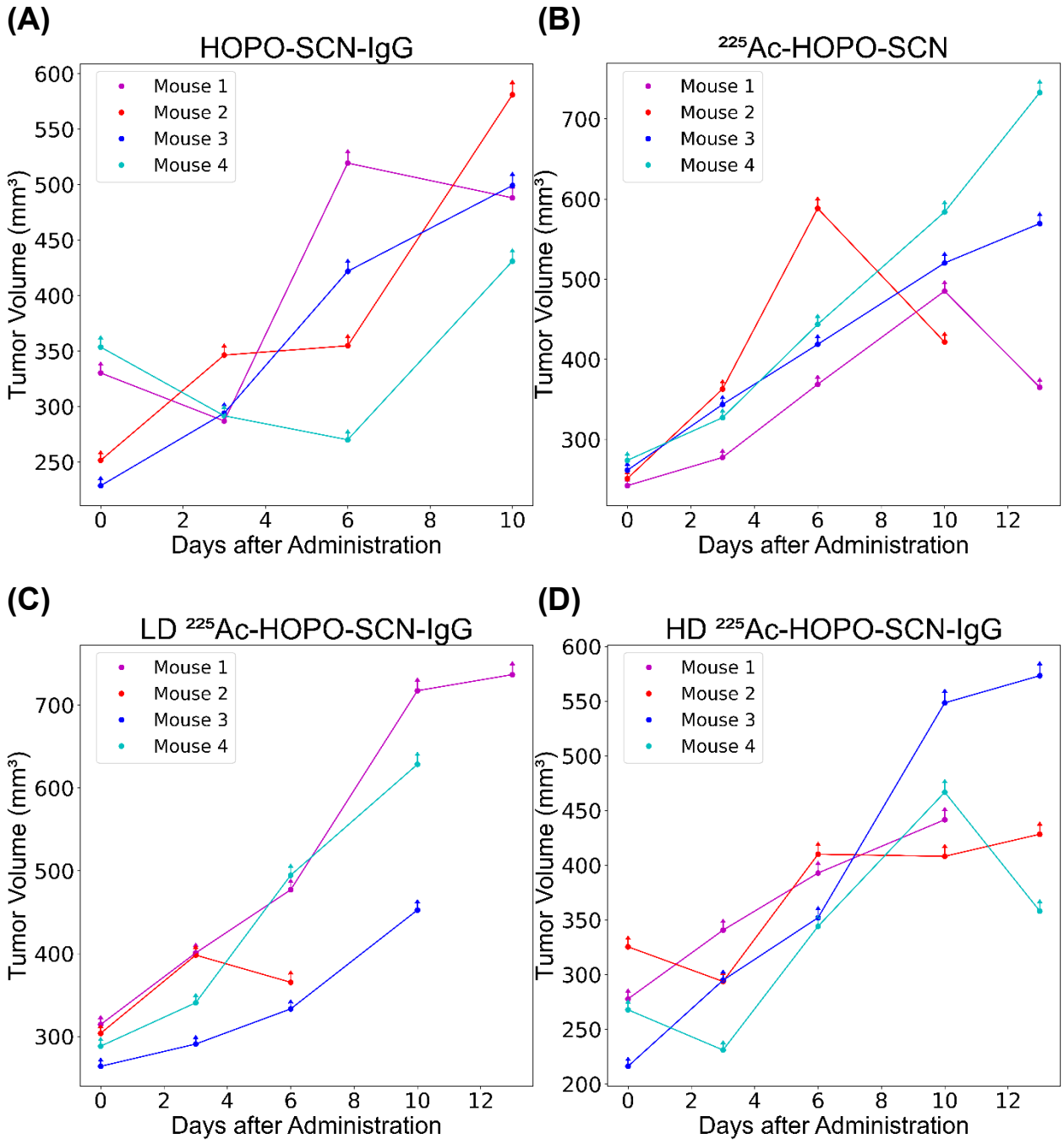
(A)
HOPO-SCN-IgG
Mouse 1
Mouse 2
Mouse 3
Mouse 4
Tumor Volume (mm³)
Days after Administration
(B)
225Ac-HOPO-SCN
Mouse 1
Mouse 2
Mouse 3
Mouse 4
Tumor Volume (mm³)
Days after Administration
(C)
LD 225Ac-HOPO-SCN-IgG
Mouse 1
Mouse 2
Mouse 3
Mouse 4
Tumor Volume (mm³)
Days after Administration
(D)
HD 225Ac-HOPO-SCN-IgG
Mouse 1
Mouse 2
Mouse 3
Mouse 4
Tumor Volume (mm³)
Days after Administration

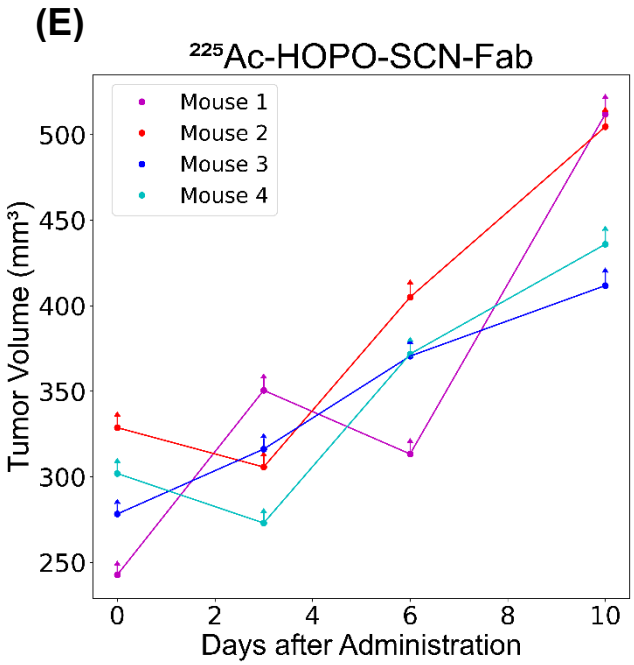

Figure 6.4: Individual tumor growth curves of SK-OV-3 tumor bearing NOD SCID mice administered with (A) cold HOPO-Siderocalin-Trastuzumab-IgG, (B) 3784.1 Bq of ^{225}Ac-HOPO-Siderocalin, (C) 333.0 Bq of ^{225}Ac-HOPO-Siderocalin-Trastuzumab-IgG, (D) 603 Bq of ^{225}Ac-HOPO-Siderocalin-Trastuzumab-IgG, and (E) 59.2 Bq of ^{225}Ac-HOPO-Siderocalin-Trastuzumab-Fab. Each data point is the tumor volume for a single mouse, and the error bars represent the experimental error of manually measuring tumors with calipers. Only the upper error bar is displayed for ease of visualization. IgG is Trastuzumab-IgG, Fab is Trastuzumab-Fab, and SCN is Siderocalin. LD is the low dose of ^{225}Ac-HOPO-Siderocalin-Trastuzumab-IgG at 333.0 Bq while HD is the high dose of ^{225}Ac-HOPO-Siderocalin-Trastuzumab-IgG at 603 Bq.

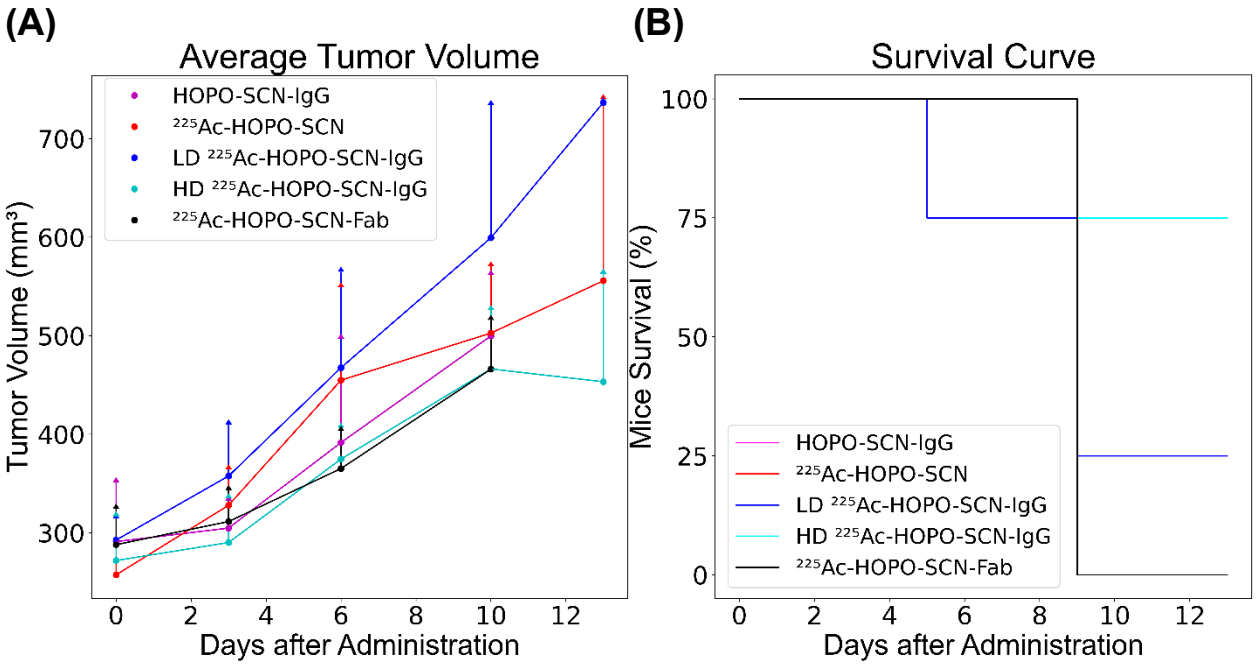

Figure 6.5: (A) Average tumor growth curves and (B) survival curves of SK-OV-3 tumor bearing NOD SCID mice administered with cold HOPO-Siderocalin-Trastuzumab-IgG, 3784.1 Bq of ^{225}Ac-HOPO-Siderocalin, 333 Bq of ^{225}Ac-HOPO-Siderocalin-Trastuzumab-IgG, 603.0 Bq of ^{225}Ac-HOPO-Siderocalin-Trastuzumab-IgG, and 59.2 Bq of ^{225}Ac-HOPO-Siderocalin-Trastuzumab-Fab. Each data point is the average value of the 4 mice in each group, and the error bars represent the 1-sigma standard deviation. Only the upper error bar is displayed for ease of visualization. IgG is Trastuzumab-IgG, Fab is Trastuzumab-Fab, and SCN is Siderocalin. LD is the low dose of ^{225}Ac-HOPO-Siderocalin-Trastuzumab-IgG at 333.0 Bq while HD is the high dose of ^{225}Ac-HOPO-Siderocalin-Trastuzumab-IgG at 603.0 Bq. For the survival curve, the cold HOPO-Siderocalin-IgG curve is overlapping with the ^{225}Ac-HOPO-Siderocalin-Fab curve and the ^{225}Ac-HOPO-Siderocalin curve is overlapping with the HD ^{225}Ac-HOPO-Siderocalin-IgG curve.

6.3.2 Fusion proteins labeled with ^{90}Y

Radiochemical yield was not measured for labeling these fusion proteins with ^{90}Y as spin filtration was not done for purification purposes like with the ^{225}Ac labeled fusion proteins and the antibody drug conjugates in Chapter 4 and 5. Radiochemical purity was determined by radio-ITLC where it was determined that labeled proteins and HOPO (Figure 6.6(B)) stayed at the origin and the free metal moved up the plate with the solvent front (Fig. 6.6(A)). ^{90}Y-HOPO had a radiochemical purity of 81.0% (Fig.6.6(B)). The ^{90}Y-HOPO-Siderocalin radiochemical purity was rather consistent over 3 days where it was 85.9% at day 0 (Fig.6.7(A)), 84.3% at day 1 (Fig.6.7(B)), and 86.7% at day 3 (Fig. 6.7(C)). The ^{90}Y-HOPO-Siderocalin-Trastuzumab-IgG radiochemical purity was also consistent over 3 days where it was 86.3% at day 0 (Fig. 6.8(A)), 82.6% at day 1 (Fig. 6.8(B)), and 84.9% at day 3 (Fig.6.8(C)). The ^{90}Y-HOPO-Siderocalin-Trastuzumab-

Fab radiochemical purity also displayed the latter's consistency where it was 87.2% at day 0 (Fig. 6.9(A), 86.7% at day 1 (Fig. 6.9(B)), and 84.9% at day 3 (Fig. 6.9(C)). All of these radiochemical purity results are tabulated in Table 6.3 for ease of comparison. Table 6.4 tabulates the location and the full width at half maximum (FWHM) of the prominent peak for the ^{90}Y-HOPO-Siderocalin, ^{90}Y-HOPO-Siderocalin-Trastuzumab-IgG, and ^{90}Y-HOPO-Siderocalin-Trastuzumab-Fab TLC traces. Based on the location and FWHM of the peaks, there seems to be no difference in retention times for all three constructs.

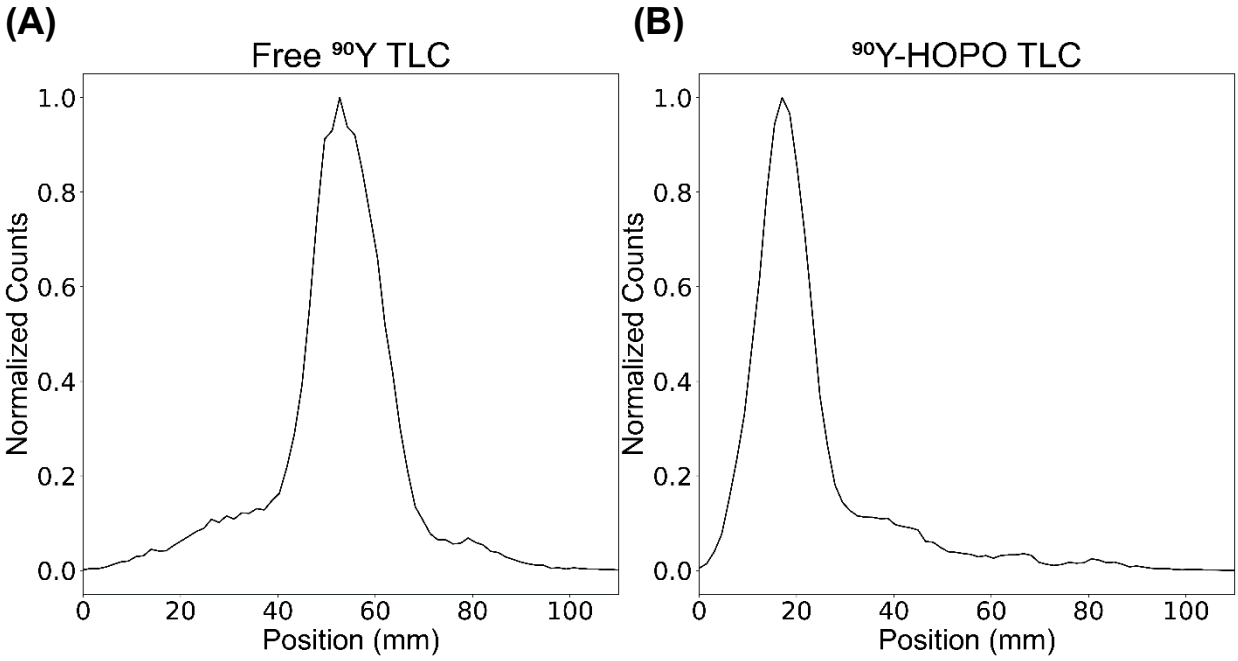

Figure 6.6: Radio-ITLC traces of (A) free ^{90}Y and (B) ^{90}Y-HOPO.

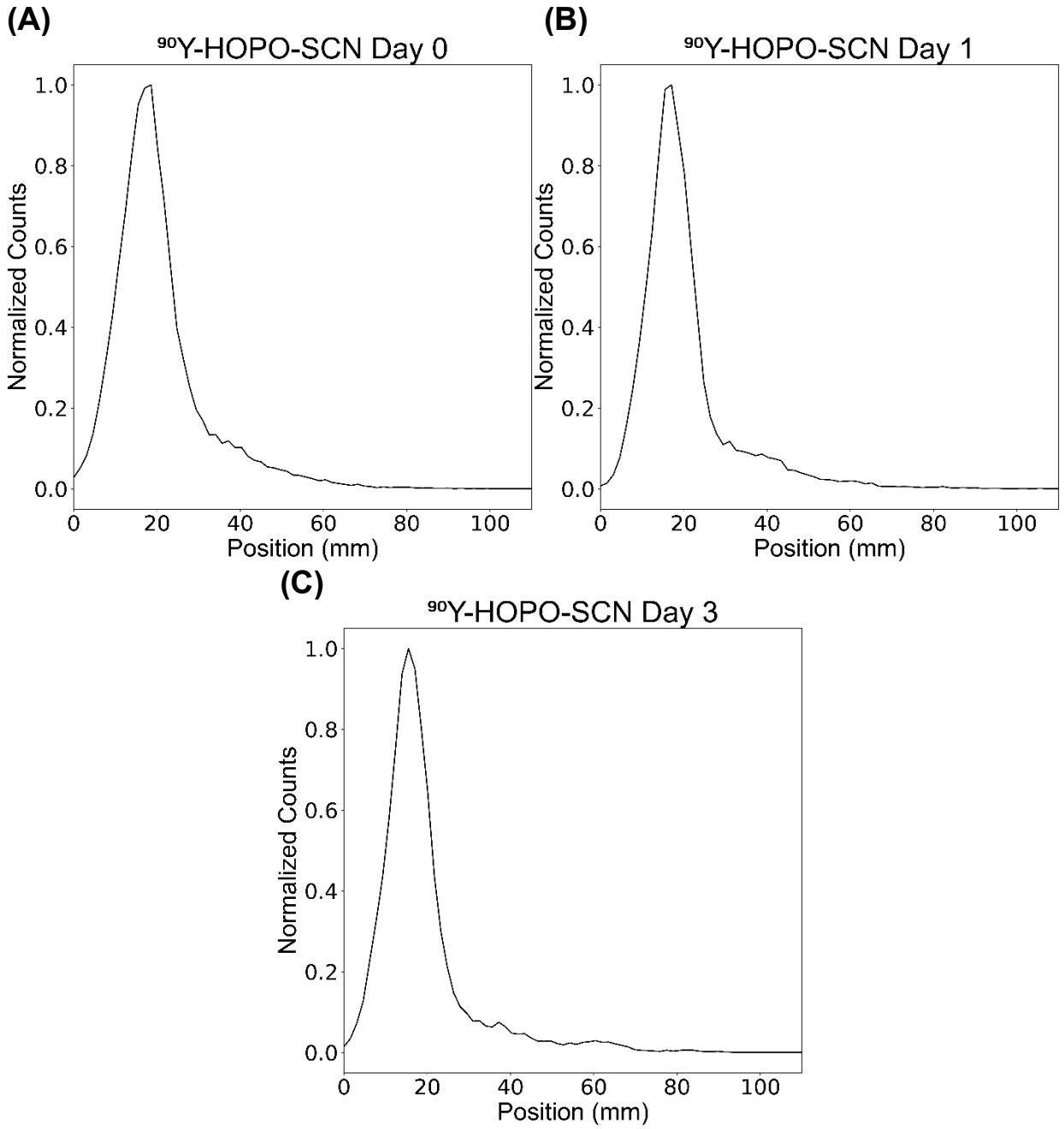

Figure 6.7: Radio-ITLC traces of ^{90}Y-HOPO-Siderocalin (A) immediately after radiolabeling, (B) a day after radiolabeling, and (C) 3 days after radiolabeling. SCN is Siderocalin.

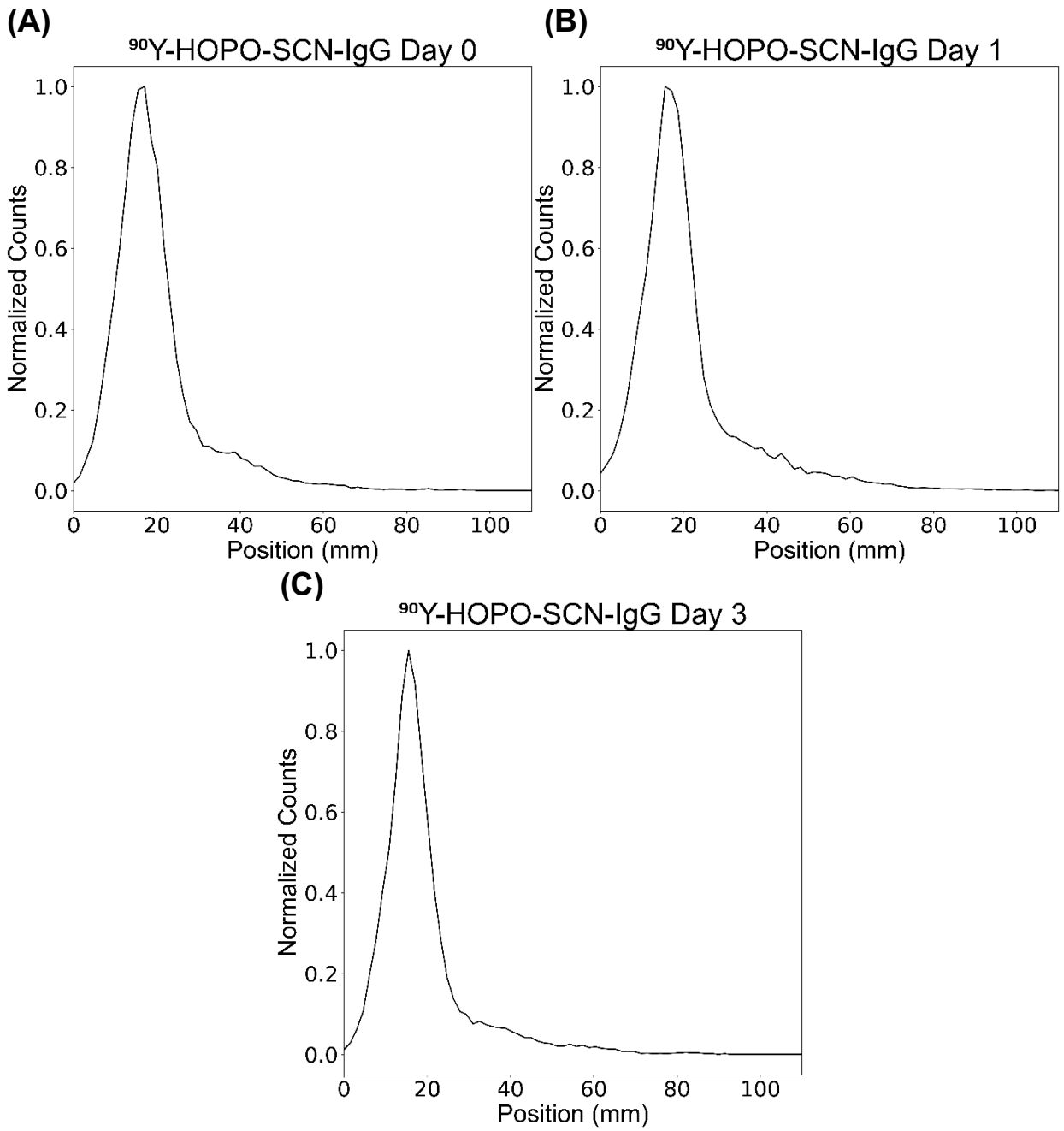

Figure 6.8: Radio-ITLC traces of ^{90}Y-HOPO-Siderocalin-Trastuzumab-IgG (A) immediately after radiolabeling, (B) a day after radiolabeling, and (C) 3 days after radiolabeling. SCN is Siderocalin and IgG is Trastuzumab-IgG.

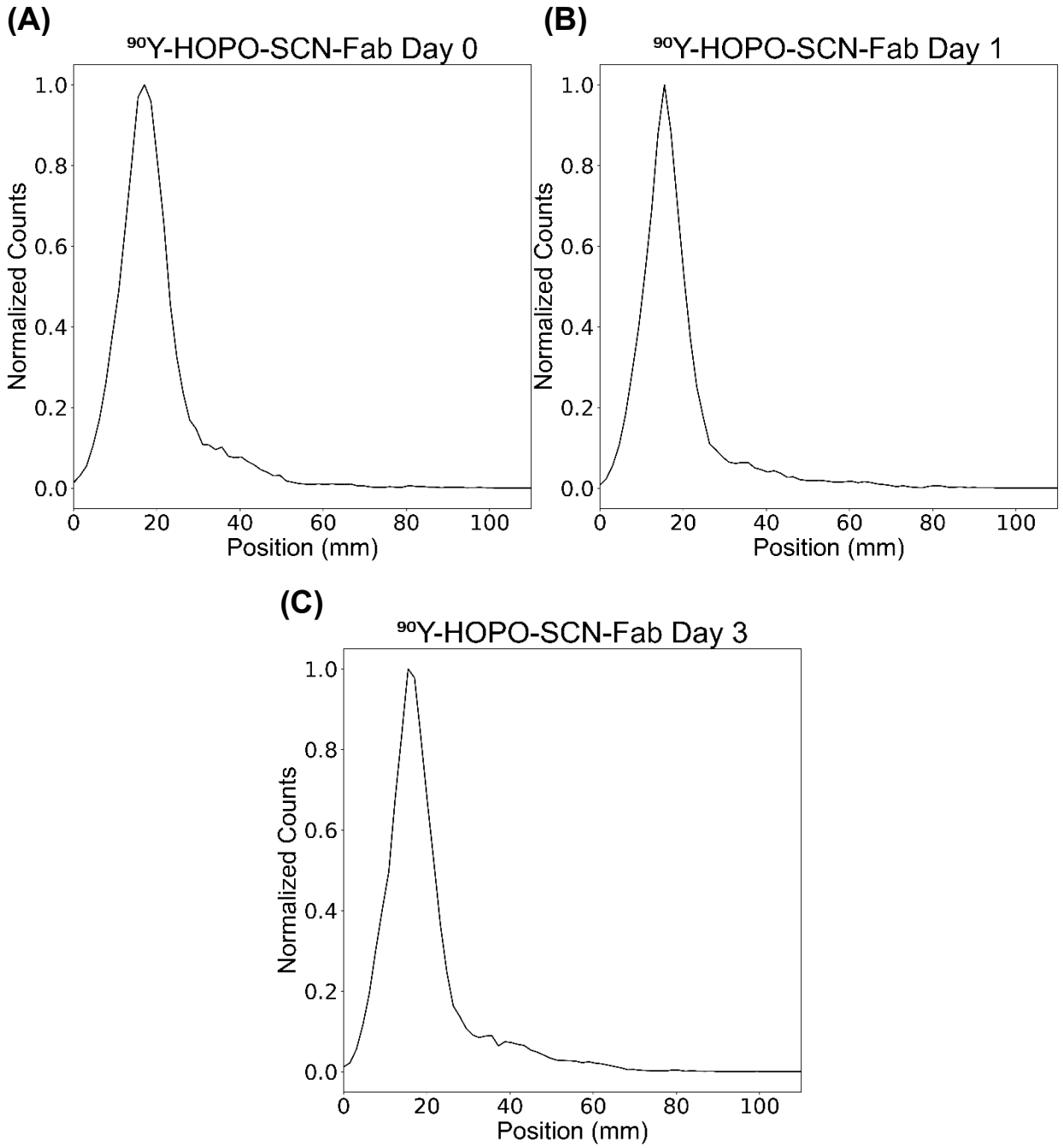

Figure 6.9: Radio-ITLC traces of ^{90}Y-HOPO-Siderocalin-Trastuzumab-Fab (A) immediately after radiolabeling, (B) a day after radiolabeling, and (C) 3 days after radiolabeling. SCN is Siderocalin and Fab is Trastuzumab-Fab.

Table 6.3: Radiopurity for ^{90}Y-HOPO-Siderocalin, ^{90}Y-HOPO-Siderocalin-Trastuzumab-IgG, and ^{90}Y-HOPO-Siderocalin-Trastuzumab-Fab.

Day	^{90}Y-HOPO-SCN	^{90}Y-HOPO-SCN- IgG	^{90}Y-HOPO-SCN-Fab
0	85.9%	86.3%	87.2%
1	84.3%	82.6%	86.7%
3	86.7%	84.9%	84.9%

Table 6.4: Location of the peak and the full width at half maximum (FWHM) of the prominent peak for the ^{90}Y-HOPO-Siderocalin, ^{90}Y-HOPO-Siderocalin-Trastuzumab-IgG, and ^{90}Y-HOPO-Siderocalin-Trastuzumab-Fab TLC traces.

	^{90}Y-HOPO-SCN		^{90}Y-HOPO-SCN-IgG		^{90}Y-HOPO-SCN-Fab	
Day	Peak (mm)	FWHM (mm)	Peak (mm)	FWHM (mm)	Peak (mm)	FWHM (mm)
0	18.6	14.0	17.1	12.4	17.1	10.9
1	17.1	10.9	15.5	12.4	15.5	10.9
3	15.5	10.9	15.5	10.9	15.5	10.9
Avg ± SD	17.1 ± 1.6	11.9 ± 1.8	16.0 ± 0.9	11.9 ± 0.9	16.0 ± 0.9	10.9 ± 0.0

Figure 6.10 shows the *ex vivo* biodistribution for the 3 constructs at 5 hours, 25 hours, and 50 hours. The ^{90}Y-HOPO-Siderocalin negative control group shows surprisingly consistent but stagnant elevated tumor uptake at all three timepoints (5.91 ± 4.66 %IA/g at 5 hours, 5.53 ± 5.33 %IA/g at 25 hours, and 6.03 ± 1.86 %IA/g at 50 hours) (Fig. 6.10(A, D)). ^{90}Y-HOPO-Siderocalin-Trastuzumab-IgG showed similar results as well through all three timepoints (4.71 ± 2.14 %IA/g at 5 hours, 7.24 ± 3.39 %IA/g at 25 hours, and 4.35 ± 2.71 %IA/g at 50 hours) (Fig. 6.10(B, D)). ^{90}Y-HOPO-Siderocalin-Trastuzumab-Fab showed rapid elevated tumor uptake at 5 hours and then decreased and plateaued at the later timepoints (12.73 ± 3.72 %IA/g at 5 hours, 5.09 ± 7.86 %IA/g at 25 hours, 6.30 ± 2.06 %IA/g at 50 hours) (Fig. 6.10(C, D)). Minimal ^{90}Y uptake is located femur through all three constructs indicating high *in vivo* stability.

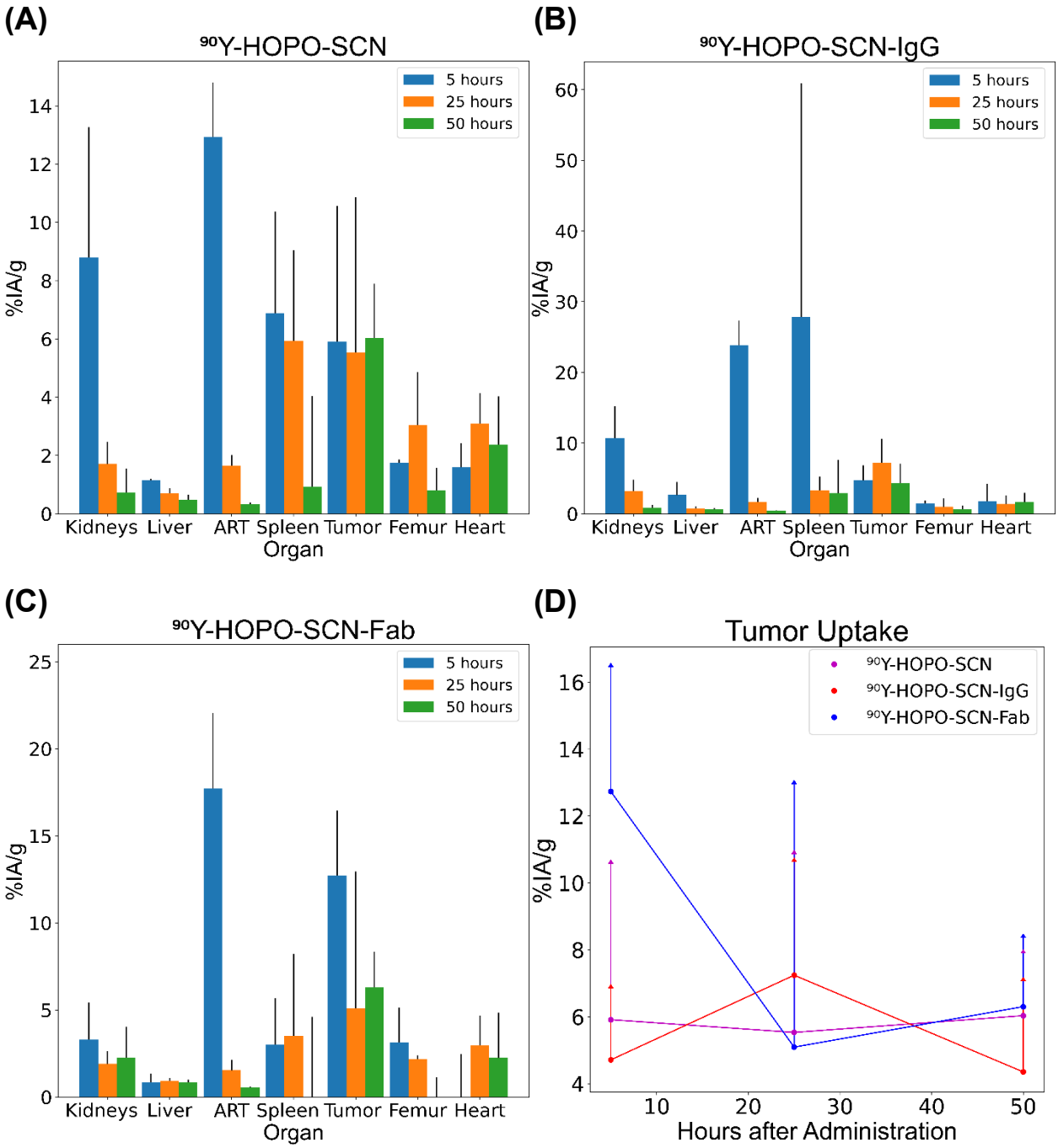

Figure 6.10: *Ex vivo* (A) ^{90}Y-HOPO-Siderocalin, (B) ^{90}Y-HOPO-Siderocalin-Trastuzumab-IgG, and (C) ^{90}Y-HOPO-Siderocalin-Trastuzumab-Fab biodistribution in SK-OV-3 tumor bearing NOD SCID mice in terms of %IA/g at 5 hours, 25 hours, and 50 hours after administration measured by liquid scintillation counting. Each data point is the average value of the 3 mice in each group, and the error bars represent the 1-sigma standard deviation. Only the upper error bar is displayed for ease of visualization. IgG is Trastuzumab-IgG, Fab is Trastuzumab-Fab, and SCN is Siderocalin. ART is abdominal remaining tissue. The tumor uptake (D) is displayed in a separate graph for ease of comparison).

The individual tumor growth curves are shown for all 4 treatment groups in Figure 6.11. The ^{90}Y radiolabeled groups (^{90}Y-HOPO-Siderocalin (Fig. 6.11(A)), ^{90}Y-HOPO-Siderocalin-Trastuzumab-IgG (Fig. 6.11(B)), and ^{90}Y-HOPO-Siderocalin-Trastuzumab-IgG (Fig. 6.11(C))) all follow a similar growth trend to the negative control no treatment group in Figure 6.11(D). This similarity is also apparent in Figure 6.12(A) which shows the average tumor volume growth for each group is not statistically significantly different from one and other (notice the 1 standard deviation error bars all overlap). The mice seemed to tolerate the constructs well and did not lose more than %15 of their body mass on administration day. All the mice were euthanized due to ulcerations in their tumors as shown in the survival curve in Figure 6.12(B).

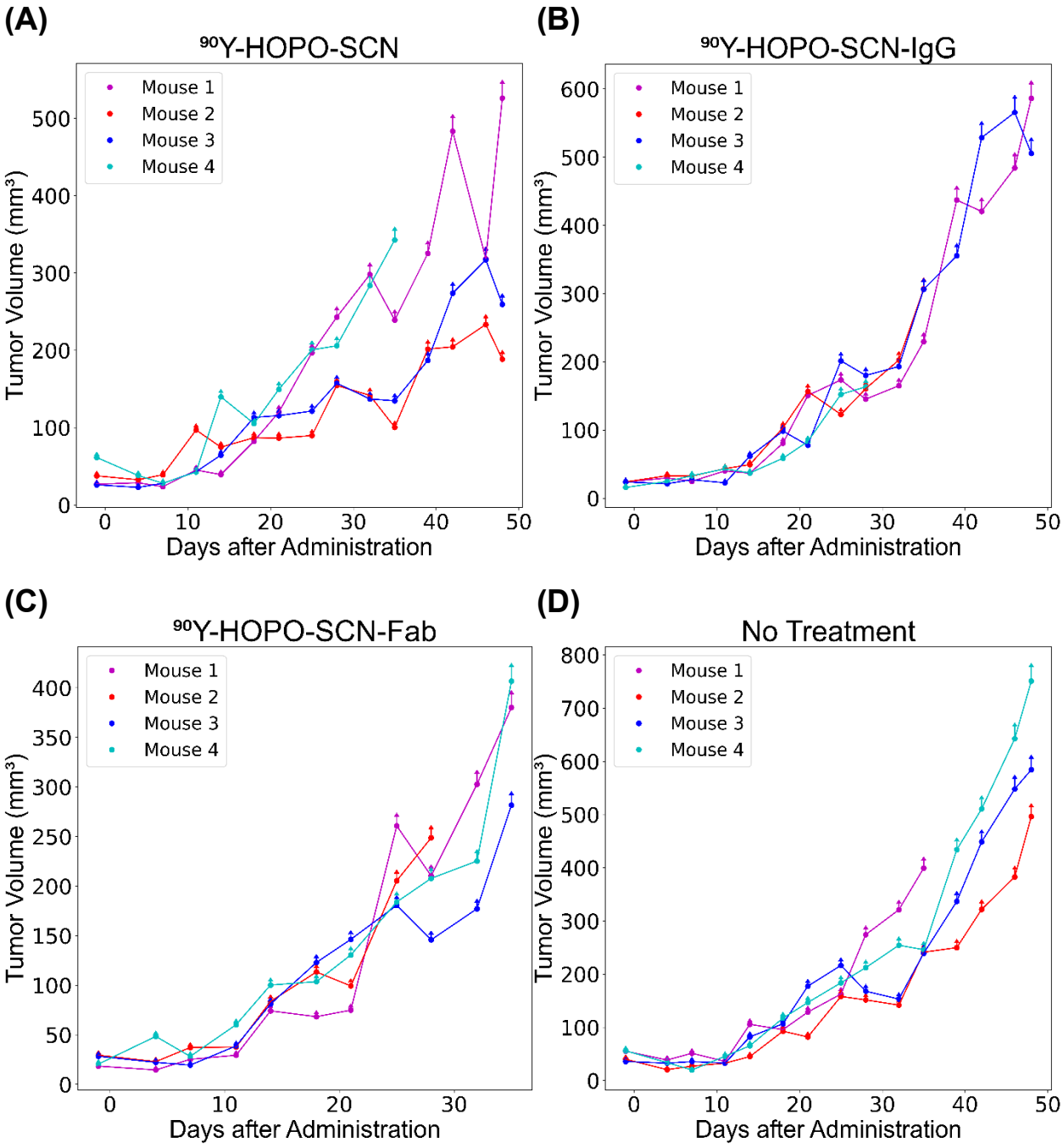

Figure 6.11: Individual tumor growth curves of SK-OV-3 tumor bearing NOD SCID mice administered with (A) 1.63 MBq of ^{90}Y-HOPO-Siderocalin, (B) 1.65 MBq of ^{90}Y-HOPO-Siderocalin-Trastuzumab-IgG, (C) 1.70 MBq of ^{90}Y-HOPO-Siderocalin-Trastuzumab-Fab, and (D) no treatment. Each data point is the tumor volume for a single mouse, and the error bars represent the experimental error of manually measuring tumors with calipers. Only the upper error bar is displayed for ease of visualization. IgG is Trastuzumab-IgG, Fab is Trastuzumab-Fab, and SCN is Siderocalin.

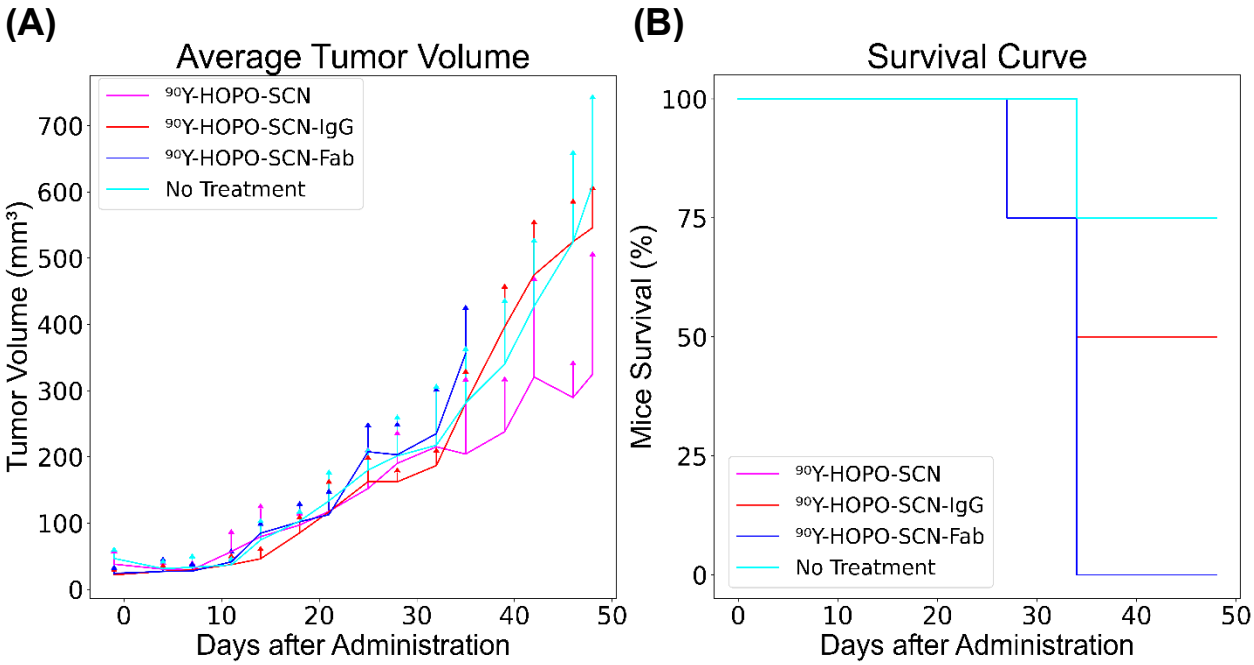

Figure 6.12: (A) Average tumor growth curves and (B) survival curves of SK-OV-3 tumor bearing NOD SCID mice administered with 1.63 MBq of ^{90}Y-HOPO-Siderocalin, 1.65 MBq of ^{90}Y-HOPO-Siderocalin-Trastuzumab-IgG, 1.70 MBq of ^{90}Y-HOPO-Siderocalin-Trastuzumab-Fab, and no treatment. Each data point is the average value of the 4 mice in each group, and the error bars represent the 1-sigma standard deviation. Only the upper error bar is displayed for ease of visualization. IgG is Trastuzumab-IgG, Fab is Trastuzumab-Fab, and SCN is Siderocalin. For the survival curve, the ^{90}Y-HOPO-Siderocalin curve is overlapping with the no treatment curve.

6.4 Discussion

One of the benefits of using Siderocalin's ability to non-covalently bind to negatively charged HOPO complexes is the binding process is fast and can be performed at room temperature unlike the more traditional covalent binding approach using isothiocyanatobenzyl-based bifunctional chelators which require elevated heating for 1 hour and then require more time and potentially more heating for radiolabeling[42,155]. Siderocalin and HOPO could pave the door way for antibody labeling "cold-kits" which could facilitate the use of targeted radiopharmaceuticals in the clinical setting[162]. Unfortunately one of the downsides of this study is that the radio-ITLC conditions that were used could not distinguish between ^{90}Y-HOPO-Siderocalin and ^{90}Y-HOPO since both of these species stayed at the origin. In Chapter 3, the radio-ITLC conditions used for the ^{134}Ce-HOPO complex were pH shifted to 10.5 which caused HOPO to follow the solvent front[85]. Unfortunately, these conditions are not commonly used for radiolabeled antibodies where the pH is not adjusted and stays around 5-5.5, and previous studies investigating HOPO complexes with radio-ITLC used these same conditions[36,106]. In the future, liquid chromatography with mass spectrometry will be used to quality control these fusion proteins as the technique could easily separate free ^{90}Y, ^{90}Y-HOPO, and ^{90}Y-HOPO-Siderocalin[147].

One of the failures of this study was that it is not clear that either the ^{225}Ac was bound to HOPO or that the ^{225}Ac-HOPO complex was bound to the fusion protein based on the low radiochemical yield and the biodistribution results. This failure of HOPO to coordinate ^{225}Ac with the given conditions isn't necessarily surprising because the chemical properties of actinium are generally unknown compared to other *f*-elements due to its limited availability[69]. In fact, no crystal structure has ever been solved for actinium since its discovery in 1899[136]. Unfortunately, because the ^{225}Ac-based experiment occurred before the ^{90}Y experiment, purification of the ^{90}Y fusion proteins through 0.5 mL 10 kDa Amicon Ultra centrifugal filter units was not performed as it was thought to be potentially one of the causes of the low radiochemical yield for the ^{225}Ac study. Future work will rigorously test ^{225}Ac-HOPO labeling conditions with High Performance Liquid Chromatography and develop a more robust purification methodology for these Siderocalin fusion proteins using size exclusion chromatography using PD-10 columns[163].

The ^{90}Y fusion protein study highlights the stability of ^{90}Y-HOPO complexes. Over 3 days, the radiochemical purity stayed approximately constant. In addition, limited bone and kidney uptake were apparent in the biodistribution with the exception of elevated kidney uptake for ^{90}Y-HOPO-Siderocalin and ^{90}Y-HOPO-Siderocalin-Trastuzumab-Fab. This elevated kidney uptake is due to renal elimination of the Siderocalin protein which is not surprising based on previous Siderocalin biodistribution studies[161]. Unlike Trastuzumab-IgG which circulates in the body for a long period of time, Trastuzumab-Fab is more rapidly cleared through renal elimination which explains the consistently elevated kidney uptake in the ^{90}Y biodistribution study[39,164,165]. Furthermore, Trastuzumab-Fab expresses elevated uptake in tumors more rapidly than Trastuzumab-IgG explaining the more elevated levels in the tumor. It is anticipated that at longer timepoints the uptake of the Trastuzumab-IgG fusion protein will increase dramatically which is what has been observed with ^{89}Zr-HOPO-Trastuzumab[36]. While imaging ^{86}Y labeled fusion proteins will be done in the future in order to corroborate the ^{90}Y biodistribution results, a longer-lived PET isotope such as ^{134}Ce or ^{89}Zr is required to confirm long term tumor targeting with the Trastuzumab-IgG fusion proteins.

While the ^{225}Ac fusion protein tumor control experiment failed due to a poor radiochemical yield, the ^{90}Y fusion protein tumor control experiment could have failed due to the administration of too little activity. In other preclinical yttrium theranostic experiments using antibodies, the administered ^{90}Y dose was between 4.4 and 5.5 MBq while the administered dose for this experiment was around 1.7 MBq[115,117]. This lower dose was due to material limitations and also an attempt to take into account the radiosensitivity of NOD SCID mice[166]. Higher activity and potentially another mouse model (athymic nude mice) are warranted in order to see tumor control.

The down side of using HOPO for Siderocalin fusion proteins is that it prevents the use of tetravalent metal cations such as the $^{227}Th^{IV}$ and $^{89}Zr^{IV}$ since they would form neutrally charged complexes. In addition, labeling HOPO with ^{134}Ce would stabilize ^{134}Ce to $^{134}Ce^{IV}$ causing the formation of a neutral complex which prevents the use of ^{225}Ac-$^{134}Ce^{III}$ theranostics[85]. Through the use of a chelator with catecholamide (CAM) moieties on a spermine backbone or 3,4,3-LI(CAM), the use of tetravalent metal cations in these Siderocalin fusion proteins since these complexes will form a $[M^{IV}$-3,4,3-LI(CAM)$]^{-4}$ complex and bind strongly to Siderocalin[161]. Unfortunately, it is unknown

whether 3,4,3-LI(CAM) will stabilize ^{134}Ce to $^{134}Ce^{IV}$ which could limit this system's potential for ^{227}Th-$^{134}Ce^{IV}$ theranostics.

6.5 Conclusions

Herein, it was demonstrated that Siderocalin fusion proteins allow for tumor targeting with high *in vivo* stability with ^{90}Y-HOPO complexes. In addition, the rapid non-covalent binding of Siderocalin to negative charged HOPO complexes allows could facilitate the labeling of trivalent radiometals to antibodies by completely removing the conjugation step and greatly reducing the time needed to label the radiometal the targeted radiopharmaceutical. Future work will investigate a more robust quality control and purification method for Siderocalin fusion proteins and investigate the system with other strategic radiometals.

CHAPTER 7: Conclusion

In this dissertation, new strategies were discussed with the purpose of advancing targeting radiopharmaceuticals for theranostic applications. These strategies ranged from a new diagnostic radiometal (^{134}Ce) to serve as theranostic matched pairs for ^{225}Ac and ^{227}Th, a novel chelator, 3,4,3-LI(1,2-HOPO) (HOPO), that can enable rapid, room-temperature radiolabeling that form complexes with high kinetic inertness with a variety of radiometals, a new elution strategy for a generator produced radiometal, ^{212}Pb, which can facilitate radiolabeling of said radiometal, and Siderocalin fusion proteins which could open the doorway for antibody-based “cold-kits”.

Through the investigations of the ^{134}Ce/^{134}La *in vivo* generator system, the biodistribution of ^{134}Ce complexes was assayed through microPET imaging. These studies demonstrated the surrogacy of ^{134}Ce to both ^{225}Ac and ^{227}Th (with appropriate chelator selection) because of the unique Ce^{III}/Ce^{IV} redox couple. Moreover, ^{134}Ce long half-life allowed for the long term (9 days after administration) tumor imaging of ^{134}Ce-DOTA-Trastuzumab in a SK-OV-3 murine model. This proof of concept experiment demonstrates ^{134}Ce ability to act as a theranostic matched pair for ^{225}Ac in antibody-based targeted radiopharmaceuticals.

Through the investigations of the *in vivo* stability and biodistribution of ^{86}Y-HOPO, HOPO was demonstrated to be a superior chelator for ^{86}Y compared to DTPA or DOTA due to HOPO allowing for rapid room temperature labeling and high *in vivo* stability. This further demonstrates HOPO’s potential as a theranostic chelator that can bind a myriad of trivalent and tetravalent radiometals. Moreover, the negatively charged ^{90}Y-HOPO complex allowed for the non-covalent binding to Siderocalin fusion proteins which demonstrated tumor targeting. With further work and optimization, this system can be used as the blueprint for antibody-based “cold-kits”.

Through the benchmarking of a novel 1.0 M sodium acetate elution strategy of a ^{224}Ra/^{212}Pb generator, radiolabeling TCMC-conjugated Trastuzumab yielded a higher radiochemical yield through 2 weeks than the traditional 2.0 M hydrochloric acid elution strategy. In addition, because the 1.0 M sodium acetate elution strategy does not require a matrix exchange, this approach minimizes the time needs to prep targeted radiopharmaceuticals which can facilitate the use of ^{212}Pb/^{203}Pb in the clinic.

7.1 Future Work

While this dissertation introduces the use of ^{134}Ce as a theranostic matched pair for both ^{225}Ac and ^{227}Th, most of the work that has been done focused on ^{134}Ce as a surrogate for ^{225}Ac. Although impeded by the low availability of both ^{134}Ce and the chelator Me-3,2-HOPO (which is the most commonly used chelator for Targeted Thorium Conjugates), *in vitro* and *in vivo* experiments are required to determine the surrogacy of Me-3,2-HOPO complexes incorporating either ^{134}Ce or ^{227}Th[25]. This coupled with a bifunctional variant of 3,4,3-LI(1,2-HOPO) could become cornerstones in ^{227}Th/^{134}Ce theranostics.

One remaining question about the use of ^{134}Ce is whether ^{134}La is released from its chelator after the decay of ^{134}Ce. This release could potentially degrade the spatial resolution ^{134}Ce PET images which could be problematic for imaging smaller structures. While this can be mitigated through the use of internalizing target vectors,

characterizing this release would be necessary to facilitate the use of non-internalizing target vectors. The use of liquid chromatography and mass spectrometry could determine this *in vitro*. For *in vivo* situations, imaging the targeted radiopharmaceutical through PET/SPECT system would allow the PET scanner to determine the biodistribution of ^{134}La while the SPECT scanner can determine the biodistribution of the ^{139}Ce impurity.

While the ^{90}Y-labeled Siderocalin fusion proteins showed tumor targeting, both the tumor control experiments and the labeling of ^{225}Ac to the fusion proteins failed. There are a few avenues that can be pursued from here. The first is more rigorous *in vitro* experiments of ^{225}Ac complexes are required in order to determine if chelation is feasible. If this is the case, the determination of adequate radiolabeling conditions is also required. The second avenue that can be pursued is developing more robust purification and quality control strategies. While the experiments that were performed in this dissertation utilized Amicon Centrifugal Filter Units, these have only led to radiochemical purities of less than 90%. Other studies in the literature have used size exclusion columns (PD-10 columns) or a combination of size exclusion columns and centrifugal filters and have obtained radiochemical purities of greater than 99%[163]. In addition, as discussed in Chapter 6, Thin layer chromatography has a hard time separating labeled Siderocalin fusion protein from free HOPO. Utilizing liquid chromatography and mass spectrometry could separate the two allowing for the determination of the proportion of HOPO complexes bound to the fusion protein. A third and final avenue would be to investigate other strategic *f*-elements including terbium radioisotopes (^{149}Tb, ^{152}Tb, ^{155}Tb, and ^{161}Tb) and ^{227}Th in these Siderocalin fusion proteins. The terbium radioisotopes are a promising theranostic quadruplet that allow for α therapy, β- therapy, auger electron therapy, SPECT imaging, and PET imaging[24]. While ^{227}Th would require the use of 3,4,3-LI(CAM) in order to be incorporated into Siderocalin fusion proteins, it is unclear whether the terbium radiometals would be stabilized to 4+ when complexed to 3,4,3-LI(1,2-HOPO). Either way, due to HOPO's affinity for trivalent and tetravalent rare earth metals, the development of terbium radiometals in HOPO-based targeted vectors could greatly advance targeted radionuclide therapy.

7.2 Outlook

While this dissertation has focused on the advancement of targeted radiopharmaceuticals through *in vivo* studies and developing new radiochemical strategies, facilitating the use of theranostics is a multidisciplinary effort. One of the main hurdles in targeted radiopharmaceuticals is the actual production of the radionuclides. The lack of availability of certain radionuclides, such as ^{225}Ac, has limited their use in clinical trials which has slowed their pathway to FDA approval and commercialization. While accelerator-produced ^{225}Ac has increased its availability in recent years, it is unclear if ^{227}Ac impurity leads to long term toxic effects[69,71]. In addition, the technological development of molecular imaging modalities is also warranted. While theranostic matched pairs allow for "unimageable" therapeutic radionuclides to be traced via conventional PET or SPECT imaging, determining accurate dosimetry of ^{225}Ac and ^{227}Th is still rather difficult due to their recoiling daughters. Advancements in sensitivity and energy resolution of SPECT systems could

potentially allow for imaging the individual daughters of both of these radionuclides. While great strides have been made in the past couple decades for targeted radionuclide therapy, there is still a long way to go.

Bibliography

1. Goldsmith SJ. Targeted Radionuclide Therapy: A Historical and Personal Review. *Seminars in Nuclear Medicine*. 2020;50(1):87-97. doi:10.1053/j.semnuclmed.2019.07.006

2. Strebhardt K, Ullrich A. Paul Ehrlich's magic bullet concept: 100 years of progress. *Nat Rev Cancer*. 2008;8(6):473-480. doi:10.1038/nrc2394

3. Parker CC, Coleman RE, Sartor O, et al. Three-year Safety of Radium-223 Dichloride in Patients with Castration-resistant Prostate Cancer and Symptomatic Bone Metastases from Phase 3 Randomized Alpharadin in Symptomatic Prostate Cancer Trial. *Eur Urol*. 2018;73(3):427-435. doi:10.1016/j.eururo.2017.06.021

4. Noto RB, Pryma DA, Jensen J, et al. Phase 1 Study of High-Specific-Activity I-131 MIBG for Metastatic and/or Recurrent Pheochromocytoma or Paraganglioma. *The Journal of Clinical Endocrinology & Metabolism*. 2018;103(1):213-220. doi:10.1210/jc.2017-02030

5. Larson SM, Carrasquillo JA, Cheung NKV, Press O. Radioimmunotherapy of human tumours. *Nat Rev Cancer*. 2015;15(6):347-360. doi:10.1038/nrc3925

6. Mondello P, Cuzzocrea S, Navarra M, Mian M. 90 Y-ibritumomab tiuxetan: a nearly forgotten opportunity. *Oncotarget*. 2015;7(7):7597-7609. doi:10.18632/oncotarget.6531

7. Hennrich U, Kopka K. Lutathera®: The First FDA- and EMA-Approved Radiopharmaceutical for Peptide Receptor Radionuclide Therapy. *Pharmaceuticals*. 2019;12(3):114. doi:10.3390/ph12030114

8. Aghevlian S, Boyle AJ, Reilly RM. Radioimmunotherapy of cancer with high linear energy transfer (LET) radiation delivered by radionuclides emitting α-particles or Auger electrons. *Adv Drug Deliv Rev*. 2017;109:102-118. doi:10.1016/j.addr.2015.12.003

9. Graf F, Fahrer J, Maus S, et al. DNA double strand breaks as predictor of efficacy of the alpha-particle emitter Ac-225 and the electron emitter Lu-177 for somatostatin receptor targeted radiotherapy. *PLoS One*. 2014;9(2):e88239. doi:10.1371/journal.pone.0088239

10. Wulbrand C, Seidl C, Gaertner FC, et al. Alpha-Particle Emitting 213Bi-Anti-EGFR Immunoconjugates Eradicate Tumor Cells Independent of Oxygenation. *PLoS One*. 2013;8(5):e64730. doi:10.1371/journal.pone.0064730

11. Kratochwil C, Bruchertseifer F, Giesel FL, et al. 225Ac-PSMA-617 for PSMA-Targeted α-Radiation Therapy of Metastatic Castration-Resistant Prostate Cancer. *J Nucl Med*. 2016;57(12):1941-1944. doi:10.2967/jnumed.116.178673

12. Friesen C, Glatting G, Koop B, et al. Breaking Chemoresistance and Radioresistance with [^{213} Bi]anti-CD45 Antibodies in Leukemia Cells. *Cancer Res*. 2007;67(5):1950-1958. doi:10.1158/0008-5472.CAN-06-3569

13. Wilbur DS. The Radiopharmaceutical Chemistry of Alpha-Emitting Radionuclides. In: Lewis JS, Windhorst AD, Zeglis BM, eds. *Radiopharmaceutical Chemistry*. Springer International Publishing; 2019:409-424. doi:10.1007/978-3-319-98947-1_23

14. Kokov KV, Egorova BV, German MN, et al. 212Pb: Production Approaches and Targeted Therapy Applications. *Pharmaceutics*. 2022;14(1):189. doi:10.3390/pharmaceutics14010189

15. Gott M, Steinbach J, Mamat C. The Radiochemical and Radiopharmaceutical Applications of Radium. *Open Chemistry*. 2016;14(1):118-129. doi:10.1515/chem-2016-0011

16. Ku A, Facca VJ, Cai Z, Reilly RM. Auger electrons for cancer therapy – a review. *EJNMMI Radiopharmacy and Chemistry*. 2019;4(1):27. doi:10.1186/s41181-019-0075-2

17. Paillas S, Ladjohounlou R, Lozza C, et al. Localized Irradiation of Cell Membrane by Auger Electrons Is Cytotoxic Through Oxidative Stress-Mediated Nontargeted Effects. *Antioxid Redox Signal*. 2016;25(8):467-484. doi:10.1089/ars.2015.6309

18. Pouget JP, Georgakilas AG, Ravanat JL. Targeted and Off-Target (Bystander and Abscopal) Effects of Radiation Therapy: Redox Mechanisms and Risk/Benefit Analysis. *Antioxid Redox Signal*. 2018;29(15):1447-1487. doi:10.1089/ars.2017.7267

19. Santoro L, Boutaleb S, Garambois V, et al. Noninternalizing monoclonal antibodies are suitable candidates for 125I radioimmunotherapy of small-volume peritoneal carcinomatosis. *J Nucl Med*. 2009;50(12):2033-2041. doi:10.2967/jnumed.109.066993

20. Yordanova A, Eppard E, Kürpig S, et al. Theranostics in nuclear medicine practice. *Onco Targets Ther*. 2017;10:4821-4828. doi:10.2147/OTT.S140671

21. Müller C, Vermeulen C, Köster U, et al. Alpha-PET with terbium-149: evidence and perspectives for radiotheragnostics. *EJNMMI Radiopharmacy and Chemistry*. 2016;1(1):5. doi:10.1186/s41181-016-0008-2

22. Rösch F, Herzog H, Qaim SM. The Beginning and Development of the Theranostic Approach in Nuclear Medicine, as Exemplified by the Radionuclide Pair 86Y and 90Y. *Pharmaceuticals (Basel)*. 2017;10(2):E56. doi:10.3390/ph10020056

23. Máthé D, Szigeti K, Hegedűs N, et al. Production and in vivo imaging of (203)Pb as a surrogate isotope for in vivo (212)Pb internal absorbed dose studies. *Appl Radiat Isot*. 2016;114:1-6. doi:10.1016/j.apradiso.2016.04.015

24. Müller C, Domnanich KA, Umbricht CA, van der Meulen NP. Scandium and terbium radionuclides for radiotheranostics: current state of development towards clinical application. *BJR*. 2018;91(1091):20180074. doi:10.1259/bjr.20180074

25. Hagemann UB, Wickstroem K, Hammer S, et al. Advances in Precision Oncology: Targeted Thorium-227 Conjugates As a New Modality in Targeted Alpha Therapy. *Cancer Biother Radiopharm*. 2020;35(7):497-510. doi:10.1089/cbr.2020.3568

26. Pelletier K, Côté G, Fallah-Rad N, John R, Kitchlu A. CKD After 225Ac-PSMA617 Therapy in Patients With Metastatic Prostate Cancer. *Kidney Int Rep*. 2020;6(3):853-856. doi:10.1016/j.ekir.2020.12.006

27. Le Fur M, Rotile NJ, Correcher C, et al. Yttrium-86 is a Positron Emitting Surrogate of Gadolinium for Noninvasive Quantification of Whole-Body Distribution of Gadolinium-Based Contrast Agents. *Angew Chem Int Ed Engl*. 2020;59(4):1474-1478. doi:10.1002/anie.201911858

28. Khozeimeh Sarbisheh E, Price EW. The Radiopharmaceutical Chemistry of the Radioisotopes of Lutetium and Yttrium. In: Lewis JS, Windhorst AD, Zeglis BM, eds. *Radiopharmaceutical Chemistry*. Springer International Publishing; 2019:359-370. doi:10.1007/978-3-319-98947-1_20

29. Abergel RJ, Kozimor SA. Innovative f-Element Chelating Strategies. *Inorg Chem*. 2020;59(1):4-7. doi:10.1021/acs.inorgchem.9b03583

30. Deblonde GJP, Sturzbecher-Hoehne M, Abergel RJ. Solution Thermodynamic Stability of Complexes Formed with the Octadentate Hydroxypyridinonate Ligand 3,4,3-LI(1,2-HOPO): A Critical Feature for Efficient Chelation of Lanthanide(IV) and Actinide(IV) Ions. *Inorg Chem*. 2013;52(15):8805-8811. doi:10.1021/ic4010246

31. Gorden AEV, Xu J, Raymond KN, Durbin P. Rational Design of Sequestering Agents for Plutonium and Other Actinides. *Chem Rev*. 2003;103(11):4207-4282. doi:10.1021/cr990114x

32. Deblonde GJP, Lohrey TD, An DD, Abergel RJ. Toxic heavy metal – Pb, Cd, Sn – complexation by the octadentate hydroxypyridinonate ligand archetype 3,4,3-LI(1,2-HOPO). *New J Chem*. 2018;42(10):7649-7658. doi:10.1039/C7NJ04559J

33. Sturzbecher-Hoehne M, Deblonde GJP, Abergel RJ. Solution thermodynamic evaluation of hydroxypyridinonate chelators 3,4,3-LI(1,2-HOPO) and 5-LIO(Me-3,2-HOPO) for UO2(VI) and Th(IV) decorporation. *Radiochimica Acta*. 2013;101(6):359-366. doi:10.1524/ract.2013.2047

34. de Kruijff RM, Wolterbeek HT, Denkova AG. A Critical Review of Alpha Radionuclide Therapy-How to Deal with Recoiling Daughters? *Pharmaceuticals (Basel)*. 2015;8(2):321-336. doi:10.3390/ph8020321

35. Lv Q, Meng Z, Yu Y, et al. Molecular Mechanisms and Translational Therapies for Human Epidermal Receptor 2 Positive Breast Cancer. *Int J Mol Sci*. 2016;17(12):2095. doi:10.3390/ijms17122095

36. Deri MA, Ponnala S, Kozlowski P, et al. p-SCN-Bn-HOPO: A Superior Bifunctional Chelator for (89)Zr ImmunoPET. *Bioconjug Chem*. 2015;26(12):2579-2591. doi:10.1021/acs.bioconjchem.5b00572

37. O'Donoghue JA, Lewis JS, Pandit-Taskar N, et al. Pharmacokinetics, Biodistribution, and Radiation Dosimetry for 89Zr-Trastuzumab in Patients with Esophagogastric Cancer. *Journal of Nuclear Medicine*. 2018;59(1):161-166. doi:10.2967/jnumed.117.194555

38. Borchardt PE, Yuan RR, Miederer M, McDevitt MR, Scheinberg DA. Targeted Actinium-225 in Vivo Generators for Therapy of Ovarian Cancer. *Cancer Res*. 2003;63(16):5084-5090.

39. Mendler CT, Gehring T, Wester HJ, Schwaiger M, Skerra A. 89Zr-Labeled Versus 124I-Labeled αHER2 Fab with Optimized Plasma Half-Life for High-Contrast Tumor Imaging In Vivo. *Journal of Nuclear Medicine*. 2015;56(7):1112-1118. doi:10.2967/jnumed.114.149690

40. Cardinale J, Giammei C, Jouini N, Mindt TL. Bioconjugation Methods for Radiopharmaceutical Chemistry. In: Lewis JS, Windhorst AD, Zeglis BM, eds. *Radiopharmaceutical Chemistry*. Springer International Publishing; 2019:449-466. doi:10.1007/978-3-319-98947-1_25

41. Goetz DH, Holmes MA, Borregaard N, Bluhm ME, Raymond KN, Strong RK. The Neutrophil Lipocalin NGAL Is a Bacteriostatic Agent that Interferes with Siderophore-Mediated Iron Acquisition. *Molecular Cell*. 2002;10(5):1033-1043. doi:10.1016/S1097-2765(02)00708-6

42. Allred BE, Rupert PB, Gauny SS, et al. Siderocalin-mediated recognition, sensitization, and cellular uptake of actinides. *PNAS*. 2015;112(33):10342-10347. doi:10.1073/pnas.1508902112

43. Könik A, O'Donoghue JA, Wahl RL, Graham MM, Van den Abbeele AD. Theranostics: The Role of Quantitative Nuclear Medicine Imaging. *Seminars in Radiation Oncology*. 2021;31(1):28-36. doi:10.1016/j.semradonc.2020.07.003

44. Bailey DL, Willowson KP. An Evidence-Based Review of Quantitative SPECT Imaging and Potential Clinical Applications. *Journal of Nuclear Medicine*. 2013;54(1):83-89. doi:10.2967/jnumed.112.111476

45. Dewaraja YK, Frey EC, Sgouros G, et al. MIRD Pamphlet No. 23: Quantitative SPECT for Patient-Specific 3-Dimensional Dosimetry in Internal Radionuclide Therapy. *Journal of Nuclear Medicine*. 2012;53(8):1310-1325. doi:10.2967/jnumed.111.100123

46. Larsson E, Brolin G, Cleton A, Ohlsson T, Lindén O, Hindorf C. Feasibility of Thorium-227/Radium-223 Gamma-Camera Imaging During Radionuclide Therapy. *Cancer Biother Radiopharm*. 2020;35(7):540-548. doi:10.1089/cbr.2019.3516

47. Hutton BF, Erlandsson K, Thielemans K. Advances in clinical molecular imaging instrumentation. *Clin Transl Imaging*. 2018;6(1):31-45. doi:10.1007/s40336-018-0264-0

48. Zheng Y, Huh Y, Su Q, et al. Collimatorless Scintigraphy for Imaging Extremely Low Activity Targeted Alpha Therapy (TAT) with Weighted Robust Least Squares (WRLS). *Med Image Comput Comput Assist Interv*. 2020;12267:803-811. doi:10.1007/978-3-030-59728-3_78

49. Seo Y. Quantitative Imaging of Alpha-Emitting Therapeutic Radiopharmaceuticals. *Nucl Med Mol Imaging*. 2019;53(3):182-188. doi:10.1007/s13139-019-00589-8

50. Cherry SR, Jones T, Karp JS, Qi J, Moses WW, Badawi RD. Total-Body PET: Maximizing Sensitivity to Create New Opportunities for Clinical Research and Patient Care. *Journal of Nuclear Medicine*. 2018;59(1):3-12. doi:10.2967/jnumed.116.184028

51. Moses WW. Fundamental Limits of Spatial Resolution in PET. *Nucl Instrum Methods Phys Res A*. 2011;648 Supplement 1:S236-S240. doi:10.1016/j.nima.2010.11.092

52. Zhang J, Maniawski P, Knopp MV. Performance evaluation of the next generation solid-state digital photon counting PET/CT system. *EJNMMI Research*. 2018;8(1):97. doi:10.1186/s13550-018-0448-7

53. Conti M, Bendriem B. The new opportunities for high time resolution clinical TOF PET. *Clin Transl Imaging*. 2019;7(2):139-147. doi:10.1007/s40336-019-00316-5

54. Liu G, Cao T, Hu L, et al. Validation of MR-Based Attenuation Correction of a Newly Released Whole-Body Simultaneous PET/MR System. *Biomed Res Int*. 2019;2019:8213215. doi:10.1155/2019/8213215

55. Rosar F, Buchholz HG, Michels S, et al. Image quality analysis of 44Sc on two preclinical PET scanners: a comparison to 68Ga. *EJNMMI Physics*. 2020;7(1):16. doi:10.1186/s40658-020-0286-3

56. Shannon RD. Revised effective ionic radii and systematic studies of interatomic distances in halides and chalcogenides. *Acta Crystallographica Section A*. 1976;32(5):751-767. doi:10.1107/S0567739476001551

57. Deal KA, Davis IA, Mirzadeh S, Kennel SJ, Brechbiel MW. Improved in vivo stability of actinium-225 macrocyclic complexes. *J Med Chem*. 1999;42(15):2988-2992. doi:10.1021/jm990141f

58. Durbin PW. Actinides in Animals and Man. In: Morss LR, Edelstein NM, Fuger J, eds. *The Chemistry of the Actinide and Transactinide Elements*. Springer Netherlands; 2006:3339-3440. doi:10.1007/1-4020-3598-5_31

59. Seidl C. Radioimmunotherapy with α-particle-emitting radionuclides. *Immunotherapy*. 2014;6(4):431-458. doi:10.2217/imt.14.16

60. Chappell LL, Deal KA, Dadachova E, Brechbiel MW. Synthesis, Conjugation, and Radiolabeling of a Novel Bifunctional Chelating Agent for 225Ac Radioimmunotherapy Applications. *Bioconjugate Chem*. 2000;11(4):510-519. doi:10.1021/bc990153f

61. Maguire WF, McDevitt MR, Smith-Jones PM, Scheinberg DA. Efficient 1-Step Radiolabeling of Monoclonal Antibodies to High Specific Activity with 225Ac for α-Particle Radioimmunotherapy of Cancer. *Journal of Nuclear Medicine*. 2014;55(9):1492-1498. doi:10.2967/jnumed.114.138347

62. Thiele NA, Brown V, Kelly JM, et al. An Eighteen-Membered Macrocyclic Ligand for Actinium-225 Targeted Alpha Therapy. *Angew Chem Int Ed Engl*. 2017;56(46):14712-14717. doi:10.1002/anie.201709532

63. Li L, Rousseau J, Jaraquemada-Peláez M de G, et al. 225Ac-H4py4pa for Targeted Alpha Therapy. *Bioconjug Chem*. 2021;32(7):1348-1363. doi:10.1021/acs.bioconjchem.0c00171

64. Comba P, Jermilova U, Orvig C, et al. Octadentate Picolinic Acid-Based Bispidine Ligand for Radiometal Ions. *Chemistry – A European Journal*. 2017;23(63):15945-15956. doi:10.1002/chem.201702284

65. Ramogida CF, Robertson AKH, Jermilova U, et al. Evaluation of polydentate picolinic acid chelating ligands and an α-melanocyte-stimulating hormone derivative for targeted alpha therapy using ISOL-produced 225Ac. *EJNMMI Radiopharmacy and Chemistry*. 2019;4(1):21. doi:10.1186/s41181-019-0072-5

66. Wharton L, Kurakina E, Radchenko V, Schaffer P, Orvig C. Chemical Promiscuity of Non-Macrocyclic Multidentate Chelating Ligands for Radiometal Ions: H4neunpa-NH2 vs H4noneunpa. *Inorg Chem*. 2021;60(6):4076-4092. doi:10.1021/acs.inorgchem.1c00152

67. Cilibrizzi A, Abbate V, Chen YL, Ma Y, Zhou T, Hider RC. Hydroxypyridinone Journey into Metal Chelation. *Chem Rev*. 2018;118(16):7657-7701. doi:10.1021/acs.chemrev.8b00254

68. Deblonde GJP, Lohrey TD, Booth CH, et al. Solution Thermodynamics and Kinetics of Metal Complexation with a Hydroxypyridinone Chelator Designed for Thorium-227 Targeted Alpha Therapy. *Inorg Chem*. 2018;57(22):14337-14346. doi:10.1021/acs.inorgchem.8b02430

69. Robertson AKH, Ramogida CF, Schaffer P, Radchenko V. Development of 225Ac Radiopharmaceuticals: TRIUMF Perspectives and Experiences. *Curr Radiopharm*. 2018;11(3):156-172. doi:10.2174/1874471011666180416161908

70. Griswold JR, Medvedev DG, Engle JW, et al. Large scale accelerator production of 225Ac: Effective cross sections for 78–192MeV protons incident on 232Th targets. *Applied Radiation and Isotopes*. 2016;118:366-374. doi:10.1016/j.apradiso.2016.09.026

71. Abergel R, An D, Lakes A, Rees J, Gauny S. Actinium Biokinetics and Dosimetry: What is the Impact of Ac-227 in Accelerator-Produced Ac-225? *Journal of Medical Imaging and Radiation Sciences*. 2019;50(1):S23. doi:10.1016/j.jmir.2019.03.073

72. Kamaleshwaran KK, Suneelkumar M, Madhusairam R, Radhakrishnan EK, Arunpandiyan S, Arnold VJ. Whole-body and Single-Photon Emission Computed Tomography/Computed Tomography Postpeptide Receptor Alpha Radionuclide Therapy Images of Actinium 225-Tetraazacyclododecanetetraacetic Acid-Octreotide as a Primary Modality of Treatment in a Patient with Advanced Rectal Neuroendocrine Tumor with Metastases. *Indian J Nucl Med*. 2020;35(3):226-228. doi:10.4103/ijnm.IJNM_58_20

73. Ocak M, Toklu T, Demirci E, Selçuk N, Kabasakal L. Post-therapy imaging of 225Ac-DOTATATE treatment in a patient with recurrent neuroendocrine tumor. *Eur J Nucl Med Mol Imaging*. 2020;47(11):2711-2712. doi:10.1007/s00259-020-04725-x

74. Cheal SM, McDevitt MR, Santich BH, et al. Alpha radioimmunotherapy using 225Ac-proteus-DOTA for solid tumors - safety at curative doses. *Theranostics*. 2020;10(25):11359-11375. doi:10.7150/thno.48810

75. Kelly VJ, Wu ST, Gottumukkala V, et al. Preclinical evaluation of an 111In/225Ac theranostic targeting transformed MUC1 for triple negative breast cancer. *Theranostics*. 2020;10(15):6946-6958. doi:10.7150/thno.38236

76. Qin Y, Imobersteg S, Blanc A, et al. Evaluation of Actinium-225 Labeled Minigastrin Analogue [225Ac]Ac-DOTA-PP-F11N for Targeted Alpha Particle Therapy. *Pharmaceutics*. 2020;12(11):E1088. doi:10.3390/pharmaceutics12111088

77. Solomon VR, Alizadeh E, Bernhard W, et al. 111In- and 225Ac-Labeled Cixutumumab for Imaging and α-Particle Radiotherapy of IGF-1R Positive Triple-Negative Breast Cancer. *Mol Pharm*. 2019;16(12):4807-4816. doi:10.1021/acs.molpharmaceut.9b00542

78. Aluicio-Sarduy E, Barnhart TE, Weichert J, Hernandez R, Engle JW. Cyclotron-Produced 132La as a PET Imaging Surrogate for Therapeutic 225Ac. *Journal of Nuclear Medicine*. 2021;62(7):1012-1015. doi:10.2967/jnumed.120.255794

79. Kostelnik TI, Orvig C. Radioactive Main Group and Rare Earth Metals for Imaging and Therapy. *Chem Rev*. 2019;119(2):902-956. doi:10.1021/acs.chemrev.8b00294

80. Prata MIM, André JP, Kovács Z, et al. Gallium(III) chelates of mixed phosphonate-carboxylate triazamacrocyclic ligands relevant to nuclear medicine: Structural, stability and in vivo studies. *J Inorg Biochem*. 2017;177:8-16. doi:10.1016/j.jinorgbio.2017.08.015

81. Li D, Minnix M, Allen R, et al. Preclinical PET Imaging of NTSR-1-Positive Tumors with 64Cu- and 68Ga-DOTA-Neurotensin Analogs and Therapy with an 225Ac-DOTA-Neurotensin Analog. *Cancer Biotherapy and Radiopharmaceuticals*. 2021;36(8):651-661. doi:10.1089/cbr.2020.3926

82. Tsionou MI, Knapp CE, Foley CA, et al. Comparison of macrocyclic and acyclic chelators for gallium-68 radiolabelling. *RSC Adv*. 2017;7(78):49586-49599. doi:10.1039/C7RA09076E

83. Aluicio-Sarduy E, Thiele NA, Martin KE, et al. Establishing Radiolanthanum Chemistry for Targeted Nuclear Medicine Applications. *Chemistry – A European Journal*. 2020;26(6):1238-1242. doi:10.1002/chem.201905202

84. Nelson B, Ferguson S, Wuest M, et al. First in vivo and phantom imaging of cyclotron produced 133La as a theranostic radionuclide for 225Ac and 135La. *Journal of Nuclear Medicine*. Published online August 1, 2021. doi:10.2967/jnumed.121.262459

85. Bailey TA, Mocko V, Shield KM, et al. Developing the 134Ce and 134La pair as companion positron emission tomography diagnostic isotopes for 225Ac and 227Th radiotherapeutics. *Nat Chem*. 2021;13(3):284-289. doi:10.1038/s41557-020-00598-7

86. Velikyan I. Prospective of ^{68} Ga-Radiopharmaceutical Development. *Theranostics*. 2014;4(1):47-80. doi:10.7150/thno.7447

87. Petrik M, Vlckova A, Novy Z, Urbanek L, Haas H, Decristoforo C. Selected 68Ga-siderophores versus 68Ga-colloid and 68Ga-citrate: biodistribution and small animal imaging in mice. *Biomed Pap Med Fac Univ Palacky Olomouc Czech Repub*. 2015;159(1):60-66. doi:10.5507/bp.2014.052

88. Prata MI, Santos AC, Geraldes CF, de Lima JJ. Characterisation of 67Ga3+ complexes of triaza macrocyclic ligands: biodistribution and clearance studies. *Nucl Med Biol*. 1999;26(6):707-710. doi:10.1016/s0969-8051(99)00041-4

89. Harris WR, Chen Y, Wein K. Equilibrium Constants for the Binding of Indium(III) to Human Serum Transferrin. *Inorg Chem*. 1994;33(22):4991-4998. doi:10.1021/ic00100a024

90. Aluicio-Sarduy E, Hernandez R, Olson AP, et al. Production and in vivo PET/CT imaging of the theranostic pair 132/135La. *Sci Rep*. 2019;9(1):10658. doi:10.1038/s41598-019-47137-0

91. Nelson BJB, Wilson J, Andersson JD, Wuest F. High yield cyclotron production of a novel 133/135La theranostic pair for nuclear medicine. *Sci Rep*. 2020;10:22203. doi:10.1038/s41598-020-79198-x

92. Opacic T, Paefgen V, Lammers T, Kiessling F. Status and trends in the development of clinical diagnostic agents. *Wiley Interdiscip Rev Nanomed Nanobiotechnol*. 2017;9(4). doi:10.1002/wnan.1441

93. Thakur ML. Gallium-67 and indium-111 radiopharmaceuticals. *Int J Appl Radiat Isot*. 1977;28(1-2):183-201. doi:10.1016/0020-708x(77)90172-7

94. Lubberink M, Lundqvist H, Tolmachev V. Production, PET performance and dosimetric considerations of134Ce/134La, an Auger electron and positron-emitting generator for radionuclide therapy. *Phys Med Biol*. 2002;47(4):615-629. doi:10.1088/0031-9155/47/4/305

95. Abou DS, Ulmert D, Doucet M, Hobbs RF, Riddle RC, Thorek DLJ. Whole-Body and Microenvironmental Localization of Radium-223 in Naïve and Mouse Models of Prostate Cancer Metastasis. *J Natl Cancer Inst*. 2015;108(5):djv380. doi:10.1093/jnci/djv380

96. Carrasquillo JA, O'Donoghue JA, Pandit-Taskar N, et al. Phase I pharmacokinetic and biodistribution study with escalating doses of ^{223}Ra-dichloride in men with castration-resistant metastatic prostate cancer. *Eur J Nucl Med Mol Imaging*. 2013;40(9):1384-1393. doi:10.1007/s00259-013-2427-6

97. Suominen MI, Fagerlund KM, Rissanen JP, et al. Radium-223 Inhibits Osseous Prostate Cancer Growth by Dual Targeting of Cancer Cells and Bone Microenvironment in Mouse Models. *Clin Cancer Res*. 2017;23(15):4335-4346. doi:10.1158/1078-0432.CCR-16-2955

98. Le Du A, Sabatié-Gogova A, Morgenstern A, Montavon G. Is DTPA a good competing chelating agent for Th(IV) in human serum and suitable in targeted alpha therapy? *J Inorg Biochem*. 2012;109:82-89. doi:10.1016/j.jinorgbio.2011.12.011

99. Larsen RH, Borrebaek J, Dahle J, et al. Preparation of TH227-labeled radioimmunoconjugates, assessment of serum stability and antigen binding ability. *Cancer Biother Radiopharm*. 2007;22(3):431-437. doi:10.1089/cbr.2006.321

100. Heyerdahl H, Abbas N, Brevik EM, Mollatt C, Dahle J. Fractionated therapy of HER2-expressing breast and ovarian cancer xenografts in mice with targeted alpha emitting 227Th-DOTA-p-benzyl-trastuzumab. *PLoS One*. 2012;7(8):e42345. doi:10.1371/journal.pone.0042345

101. Ramdahl T, Bonge-Hansen HT, Ryan OB, et al. An efficient chelator for complexation of thorium-227. *Bioorg Med Chem Lett*. 2016;26(17):4318-4321. doi:10.1016/j.bmcl.2016.07.034

102. Abbas N, Heyerdahl H, Bruland ØS, Borrebæk J, Nesland J, Dahle J. Experimental α-particle radioimmunotherapy of breast cancer using 227Th-labeled p-benzyl-DOTA-trastuzumab. *EJNMMI Res*. 2011;1:18. doi:10.1186/2191-219X-1-18

103. Murray I, Rojas B, Gear J, Callister R, Cleton A, Flux GD. Quantitative Dual-Isotope Planar Imaging of Thorium-227 and Radium-223 Using Defined Energy Windows. *Cancer Biother Radiopharm*. 2020;35(7):530-539. doi:10.1089/cbr.2019.3554

104. Benjamin RO, Cuthbertson A, Karlsson J, et al. In-vivo Comparison of Thorium-227 and Zirconium-89 Labeled 3,2-HOPO Mesothelin Antibody-chelator Conjugate. *Journal of Medical Imaging and Radiation Sciences*. 2019;50(1):S26. doi:10.1016/j.jmir.2019.03.081

105. Deri MA, Zeglis BM, Francesconi LC, Lewis JS. PET Imaging with 89Zr: From Radiochemistry to the Clinic. *Nucl Med Biol*. 2013;40(1):3-14. doi:10.1016/j.nucmedbio.2012.08.004

106. Deri MA, Ponnala S, Zeglis BM, et al. Alternative Chelator for 89Zr Radiopharmaceuticals: Radiolabeling and Evaluation of 3,4,3-(LI-1,2-HOPO). *J Med Chem*. 2014;57(11):4849-4860. doi:10.1021/jm500389b

107. Abou DS, Ku T, Smith-Jones PM. In vivo biodistribution and accumulation of 89Zr in mice. *Nucl Med Biol*. 2011;38(5):675-681. doi:10.1016/j.nucmedbio.2010.12.011

108. Beyer GJ, Bergmann R, Kampf G, Mäding P, Rösch F. Simultaneous study of the biodistribution of radio-yttrium complexed with EDTMP and citrate ligands in tumour-bearing rats. *International Journal of Radiation Applications and Instrumentation Part B Nuclear Medicine and Biology*. 1992;19(2):201-203. doi:10.1016/0883-2897(92)90008-M

109. Witzig TE. Yttrium-90-ibritumomab tiuxetan radioimmunotherapy: a new treatment approach for B-cell non-Hodgkin's lymphoma. *Drugs Today (Barc)*. 2004;40(2):111-119. doi:10.1358/dot.2004.40.2.799423

110. Kylstra JW, Witzig TE, Huang M, Emmanouilides CE, Hagenbeek A, Tidmarsh GF. Discriminatory power of the 111-indium scan (111-In) in the prediction of altered biodistribution of radio-immunoconjugate in the 90-yttrium ibritumomab tiuxetan therapeutic regimen: Meta-analysis of five clinical trials and 9 years of post-approval

safety data. *JCO*. 2011;29(15_suppl):8048-8048. doi:10.1200/jco.2011.29.15_suppl.8048

111. Breeman WAP, De Jong M, Visser TJ, Erion JL, Krenning EP. Optimising conditions for radiolabelling of DOTA-peptides with 90Y, 111In and 177Lu at high specific activities. *Eur J Nucl Med Mol Imaging*. 2003;30(6):917-920. doi:10.1007/s00259-003-1142-0

112. Chakravarty R, Chakraborty S, Dash A. A systematic comparative evaluation of 90Y-labeled bifunctional chelators for their use in targeted therapy. *J Labelled Comp Radiopharm*. 2014;57(2):65-74. doi:10.1002/jlcr.3140

113. Palm S, Enmon RM, Matei C, et al. Pharmacokinetics and Biodistribution of 86Y-Trastuzumab for 90Y Dosimetry in an Ovarian Carcinoma Model: Correlative MicroPET and MRI. *Journal of Nuclear Medicine*. 2003;44(7):1148-1155.

114. Ehlerding E, Ferreira C, Aluicio-Sarduy E, Jiang D, Engle J, Cai W. 86/90Y-based theranostics of breast cancer in a preclinical model. *Journal of Nuclear Medicine*. 2018;59(supplement 1):539-539.

115. Ehlerding EB, Ferreira CA, Aluicio-Sarduy E, et al. 86/90Y-Based Theranostics Targeting Angiogenesis in a Murine Breast Cancer Model. *Mol Pharm*. 2018;15(7):2606-2613. doi:10.1021/acs.molpharmaceut.8b00133

116. Ferreira C, Goel S, Jiang D, et al. 86/90Y-Labeled Ultrasmall Mesoporous Silica Nanoparticles for Cancer Theranostics. *Journal of Nuclear Medicine*. 2018;59(supplement 1):468-468.

117. Ferreira CA, Ehlerding EB, Rosenkrans ZT, et al. 86/90Y-Labeled Monoclonal Antibody Targeting Tissue Factor for Pancreatic Cancer Theranostics. *Mol Pharmaceutics*. 2020;17(5):1697-1705. doi:10.1021/acs.molpharmaceut.0c00127

118. Price EW, Cawthray JF, Adam MJ, Orvig C. Modular syntheses of H4octapa and H2dedpa, and yttrium coordination chemistry relevant to 86Y/90Y radiopharmaceuticals. *Dalton Trans*. 2014;43(19):7176-7190. doi:10.1039/C4DT00239C

119. Price EW, Edwards KJ, Carnazza KE, et al. A comparative evaluation of the chelators H4octapa and CHX-A″-DTPA with the therapeutic radiometal (90)Y. *Nucl Med Biol*. 2016;43(9):566-576. doi:10.1016/j.nucmedbio.2016.06.004

120. Carter KP, Deblonde GJP, Lohrey TD, et al. Developing scandium and yttrium coordination chemistry to advance theranostic radiopharmaceuticals. *Commun Chem*. 2020;3(1):1-7. doi:10.1038/s42004-020-0307-0

121. Walrand S, Flux GD, Konijnenberg MW, et al. Dosimetry of yttrium-labelled radiopharmaceuticals for internal therapy: 86Y or 90Y imaging? *Eur J Nucl Med Mol Imaging*. 2011;38 Suppl 1:S57-68. doi:10.1007/s00259-011-1771-7

122. Banerjee SR, Minn I, Kumar V, et al. Preclinical Evaluation of 203/212Pb-Labeled Low-Molecular-Weight Compounds for Targeted Radiopharmaceutical Therapy of Prostate Cancer. *J Nucl Med*. 2020;61(1):80-88. doi:10.2967/jnumed.119.229393

123. Chappell LL, Dadachova E, Milenic DE, Garmestani K, Wu C, Brechbiel MW. Synthesis, characterization, and evaluation of a novel bifunctional chelating agent for the lead isotopes 203Pb and 212Pb. *Nuclear Medicine and Biology*. 2000;27(1):93-100. doi:10.1016/S0969-8051(99)00086-4

124. Li M, Zhang X, Quinn TP, et al. Automated cassette-based production of high specific activity [203/212Pb]peptide-based theranostic radiopharmaceuticals for image-guided radionuclide therapy for cancer. *Appl Radiat Isot*. 2017;127:52-60. doi:10.1016/j.apradiso.2017.05.006

125. McNeil BL, Robertson AKH, Fu W, et al. Production, purification, and radiolabeling of the 203Pb/212Pb theranostic pair. *EJNMMI Radiopharmacy and Chemistry*. 2021;6(1):6. doi:10.1186/s41181-021-00121-4

126. Su FM, Beaumier P, Axworthy D, Atcher R, Fritzberg A. Pretargeted radioimmunotherapy in tumored mice using an in vivo 212Pb/212Bi generator. *Nuclear Medicine and Biology*. 2005;32(7):741-747. doi:10.1016/j.nucmedbio.2005.06.009

127. Yang J, Xu J, Hu L, Miao Y. A Novel Pb-203-Labeled DOTA-Conjugated Lactam Bridge-Cyclized Alpha-MSH Peptide for Melanoma Imaging. *Journal of Nuclear Medicine*. 2017;58(supplement 1):897-897.

128. Baidoo KE, Milenic DE, Brechbiel MW. Methodology for labeling proteins and peptides with lead-212 (212Pb). *Nucl Med Biol*. 2013;40(5):592-599. doi:10.1016/j.nucmedbio.2013.01.010

129. Dos Santos JC, Schäfer M, Bauder-Wüst U, et al. Development and dosimetry of 203Pb/212Pb-labelled PSMA ligands: bringing “the lead” into PSMA-targeted alpha therapy? *Eur J Nucl Med Mol Imaging*. 2019;46(5):1081-1091. doi:10.1007/s00259-018-4220-z

130. Kratochwil C, Santos J dos, Lehnert W, et al. Development and dosimetry of Pb-203/Pb-212 labeled PSMA ligands – Bringing “the Lead” into PSMA-Targeting Alpha Therapy? In: *Nuklearmedizin - NuclearMedicine*. Vol 58. Georg Thieme Verlag KG; 2019:V100. doi:10.1055/s-0039-1683594

131. Keller CA, Doherty RA. Distribution and excretion of lead in young and adult female mice. *Environ Res*. 1980;21(1):217-228. doi:10.1016/0013-9351(80)90024-9

132. He B, Frey E, Sgouros G, Ghaly M, Tworowska I, Delpassand E. Development and Validation of Methods for Quantitative In Vivo SPECT of Pb-212 ☆ ☆☆. *Journal of Medical Imaging and Radiation Sciences*. 2019;50(4):S104. doi:10.1016/j.jmir.2019.11.105

133. Atcher RW, Friedman AM, Hines JJ. An improved generator for the production of 212Pb and 212Bi from 224Ra. *Int J Rad Appl Instrum A*. 1988;39(4):283-286. doi:10.1016/0883-2889(88)90016-0

134. Tan Z, Chen P, Schneider N, et al. Significant systemic therapeutic effects of high-LET immunoradiation by 212Pb-trastuzumab against prostatic tumors of androgen-independent human prostate cancer in mice. *International Journal of Oncology*. 2012;40(6):1881-1888. doi:10.3892/ijo.2012.1357

135. Meredith RF, Torgue JJ, Rozgaja TA, et al. Safety and Outcome Measures of First-in-Human Intraperitoneal α Radioimmunotherapy With 212Pb-TCMC-Trastuzumab. *Am J Clin Oncol*. 2018;41(7):716-721. doi:10.1097/COC.0000000000000353

136. Deblonde GJP, Zavarin M, Kersting AB. The coordination properties and ionic radius of actinium: A 120-year-old enigma. *Coordination Chemistry Reviews*. 2021;446:214130. doi:10.1016/j.ccr.2021.214130

137. Medicine NRC (US) and I of M (US) C on S of the S of N. *Targeted Radionuclide Therapy*. National Academies Press (US); 2007. Accessed February 22, 2022. https://www.ncbi.nlm.nih.gov/books/NBK11464/

138. Yong K, Brechbiel MW. Towards translation of 212Pb as a clinical therapeutic; getting the lead in! *Dalton Trans*. 2011;40(23):6068-6076. doi:10.1039/C0DT01387K

139. Sturzbecher-Hoehne M, Leung CNP, D'Aléo A, et al. 3,4,3-LI(1,2-HOPO): In vitro formation of highly stable lanthanide complexes translates into efficacious in vivoeuropium decorporation. *Dalton Trans*. 2011;40(33):8340-8346. doi:10.1039/C1DT10840A

140. Sturzbecher-Hoehne M, Choi TA, Abergel RJ. Hydroxypyridinonate Complex Stability of Group (IV) Metals and Tetravalent f-Block Elements: The Key to the Next Generation of Chelating Agents for Radiopharmaceuticals. *Inorg Chem*. 2015;54(7):3462-3468. doi:10.1021/acs.inorgchem.5b00033

141. Kelley MP, Deblonde GJP, Su J, et al. Bond Covalency and Oxidation State of Actinide Ions Complexed with Therapeutic Chelating Agent 3,4,3-LI(1,2-HOPO). *Inorg Chem*. 2018;57(9):5352-5363. doi:10.1021/acs.inorgchem.8b00345

142. Deblonde GJP, Sturzbecher-Hoehne M, Rupert PB, et al. Chelation and stabilization of berkelium in oxidation state +IV. *Nature Chem*. 2017;9(9):843-849. doi:10.1038/nchem.2759

143. Loening AM, Gambhir SS. AMIDE: a free software tool for multimodality medical image analysis. *Mol Imaging*. 2003;2(3):131-137. doi:10.1162/153535003322556877

144. Richmond CR, London JE. Long-term in vivo Retention of Cerium-144 by Beagles. *Nature*. 1966;211(5054):1179-1179. doi:10.1038/2111179a0

145. Leggett R, Ansoborlo E, Bailey M, Gregoratto D, Paquet F, Taylor D. Biokinetic data and models for occupational intake of lanthanoids. *Int J Radiat Biol*. 2014;90(11):996-1010. doi:10.3109/09553002.2014.887868

146. Ewaldsson B, Magnusson G. DISTRIBUTION OF RADIOCERIUM AND RADIOPROMETHIUM IN MICE. AN AUTORADIOGRAPHIC STUDY. *Acta Radiol Ther Phys Biol*. 1964;2:65-72. doi:10.3109/02841866409134131

147. Covey TR, Lee ED, Bruins AP, Henion JD. Liquid chromatography/mass spectrometry. ACS Publications. doi:10.1021/ac00127a001

148. Bandaranayake AD, Correnti C, Ryu BY, Brault M, Strong RK, Rawlings DJ. Daedalus: a robust, turnkey platform for rapid production of decigram quantities of active recombinant proteins in human cell lines using novel lentiviral vectors. *Nucleic Acids Res*. 2011;39(21):e143. doi:10.1093/nar/gkr706

149. Finton KAK, Larimore K, Larman HB, et al. Autoreactivity and Exceptional CDR Plasticity (but Not Unusual Polyspecificity) Hinder Elicitation of the Anti-HIV Antibody 4E10. *PLOS Pathogens*. 2013;9(9):e1003639. doi:10.1371/journal.ppat.1003639

150. Kim YS, Brechbiel MW. An overview of targeted alpha therapy. *Tumour Biol*. 2012;33(3):573-590. doi:10.1007/s13277-011-0286-y

151. Hammer S, Hagemann UB, Zitzmann-Kolbe S, et al. Preclinical Efficacy of a PSMA-Targeted Thorium-227 Conjugate (PSMA-TTC), a Targeted Alpha Therapy for Prostate Cancer. *Clin Cancer Res*. 2020;26(8):1985-1996. doi:10.1158/1078-0432.CCR-19-2268

152. Hagemann UB, Wickstroem K, Wang E, et al. In Vitro and In Vivo Efficacy of a Novel CD33-Targeted Thorium-227 Conjugate for the Treatment of Acute Myeloid Leukemia. *Mol Cancer Ther*. 2016;15(10):2422-2431. doi:10.1158/1535-7163.MCT-16-0251

153. Hagemann UB, Ellingsen C, Schuhmacher J, et al. Mesothelin-Targeted Thorium-227 Conjugate (MSLN-TTC): Preclinical Evaluation of a New Targeted Alpha Therapy for Mesothelin-Positive Cancers. *Clin Cancer Res*. 2019;25(15):4723-4734. doi:10.1158/1078-0432.CCR-18-3476

154. Roy J, Jagoda EM, Basuli F, et al. In Vitro and In Vivo Comparison of 3,2-HOPO Versus Deferoxamine-Based Chelation of Zirconium-89 to the Antimesothelin Antibody Anetumab. *Cancer Biotherapy and Radiopharmaceuticals*. 2021;36(4):316-325. doi:10.1089/cbr.2020.4492

155. Thakral P, Singla S, Yadav MP, et al. An approach for conjugation of 177Lu-DOTA-SCN- Rituximab (BioSim) & its evaluation for radioimmunotherapy of relapsed & refractory B-cell non Hodgkins lymphoma patients. *Indian J Med Res*. 2014;139(4):544-554.

156. Pichler BJ, Judenhofer MS, Wehrl HF. PET/MRI hybrid imaging: devices and initial results. *Eur Radiol*. 2008;18(6):1077-1086. doi:10.1007/s00330-008-0857-5

157. Severin GW, Kristensen LK, Nielsen CH, et al. Neodymium-140 DOTA-LM3: Evaluation of an In Vivo Generator for PET with a Non-Internalizing Vector. *Frontiers in Medicine*. 2017;4. Accessed January 13, 2022. https://www.frontiersin.org/article/10.3389/fmed.2017.00098

158. P. Baum R, Singh A, Benešová M, et al. Clinical evaluation of the radiolanthanide terbium-152: first-in-human PET/CT with 152 Tb-DOTATOC. *Dalton Transactions*. 2017;46(42):14638-14646. doi:10.1039/C7DT01936J

159. Hofman MS, Emmett L, Violet J, et al. TheraP: a randomized phase 2 trial of Lu-177-PSMA-617 theranostic treatment vs cabazitaxel in progressive metastatic castration-resistant prostate cancer (Clinical Trial Protocol ANZUP 1603). Published online October 22, 2019. doi:10.1111/bju.14876

160. Naskar N, Lahiri S. Theranostic Terbium Radioisotopes: Challenges in Production for Clinical Application. *Front Med (Lausanne)*. 2021;8:675014. doi:10.3389/fmed.2021.675014

161. Captain I, Deblonde GJP, Rupert PB, et al. Engineered Recognition of Tetravalent Zirconium and Thorium by Chelator-Protein Systems: Toward Flexible Radiotherapy and Imaging Platforms. *Inorg Chem*. 2016;55(22):11930-11936. doi:10.1021/acs.inorgchem.6b02041

162. Satpati D. Recent Breakthrough in 68Ga-Radiopharmaceuticals Cold Kits for Convenient PET Radiopharmacy. *Bioconjugate Chem*. 2021;32(3):430-447. doi:10.1021/acs.bioconjchem.1c00010

163. Zeglis BM, Lewis JS. The Bioconjugation and Radiosynthesis of 89Zr-DFO-labeled Antibodies. *JoVE (Journal of Visualized Experiments)*. 2015;(96):e52521. doi:10.3791/52521

164. Tang Y, Scollard D, Chen P, Wang J, Holloway C, Reilly RM. Imaging of HER2/neu expression in BT-474 human breast cancer xenografts in athymic mice using [99mTc]-HYNIC-trastuzumab (Herceptin) Fab fragments. *Nuclear Medicine Communications*. 2005;26(5):427-432.

165. Rathore Y, Shukla J, Laroiya I, et al. Development 68Ga trastuzumab Fab and bioevaluation by PET imaging in HER2/neu expressing breast cancer patients. *Nucl Med Commun*. Published online February 1, 2022. doi:10.1097/mnm.0000000000001521

166. Biedermann KA, Sun JR, Giaccia AJ, Tosto LM, Brown JM. scid mutation in mice confers hypersensitivity to ionizing radiation and a deficiency in DNA double-strand break repair. *Proc Natl Acad Sci U S A*. 1991;88(4):1394-1397. doi:10.1073/pnas.88.4.1394

167. Knoess C, Siegel S, Smith A, et al. Performance evaluation of the microPET R4 PET scanner for rodents. *Eur J Nucl Med Mol Imaging*. 2003;30(5):737-747. doi:10.1007/s00259-002-1052-6

168. Coenen HH, Gee AD, Adam M, et al. Open letter to journal editors on: International Consensus Radiochemistry Nomenclature Guidelines. *Ann Nucl Med*. 2018;32(3):236-238. doi:10.1007/s12149-018-1238-z

169. Maioli C, Lucignani G, Strinchini A, Tagliabue L, Del Sole A. Quality control on radiochemical purity in Technetium-99m radiopharmaceuticals labelling: three years of experience on 2280 procedures. *Acta Biomed*. 2017;88(1):49-56. doi:10.23750/abm.v88i1.5285

APPENDIX A: Concorde MicroPET R4 spatial resolution

The microPET scanner that was used for the preclinical studies in this dissertation was the Concorde MicroPET R4 (Fig. A.1), nicknamed *Sarah*, has previously been specified to support a transaxial spatial resolution of 1.66 mm full width half maximum (FWHM) for Flourine-18[167]. This measurement was verified by a Derenzo phantom designed for microPET scanners (Fig. A.2). The diameters of the holes in the Derenzo Phantom are grouped by size. From largest to smallest the hole diameters are 4.8 mm, 4.0 mm, 3.2 mm, 2.4 mm, 1.6 mm, and 1.2 mm. Based on a coronal maximum intensity projection image of the phantom, the smallest resolvable holes on the Derenzo phantom are the 1.6 mm holes which corroborates with the beforementioned transaxial spatial resolution measurement (Fig. A.3).

Figure A.1: *Sarah,* the Concorde MicroPET R4 used for the preclinical studies in this dissertation.

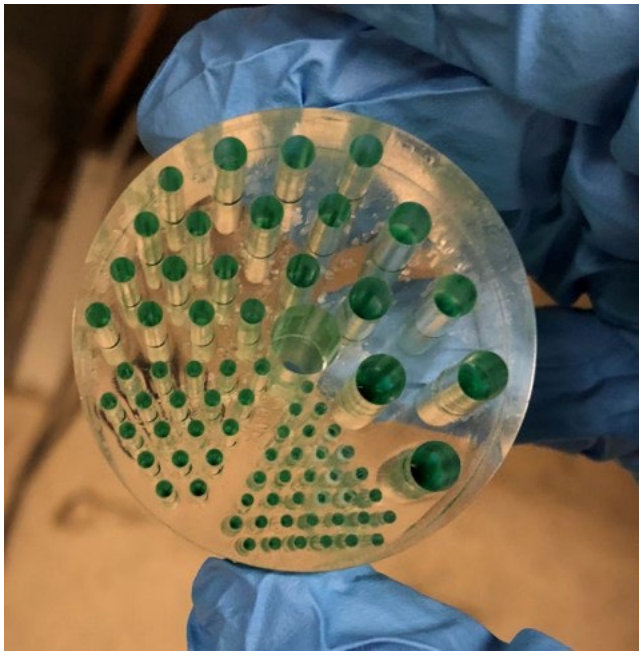

Figure A.2: The Derenzo phantom filled with ^{18}F. The green color is from food dye. From largest (4 o'clock position) to smallest (6 o'clock position), the hole diameter sizes are 4.8 mm, 4.0 mm, 3.2 mm, 2.4 mm, 1.6 mm, and 1.2 mm.

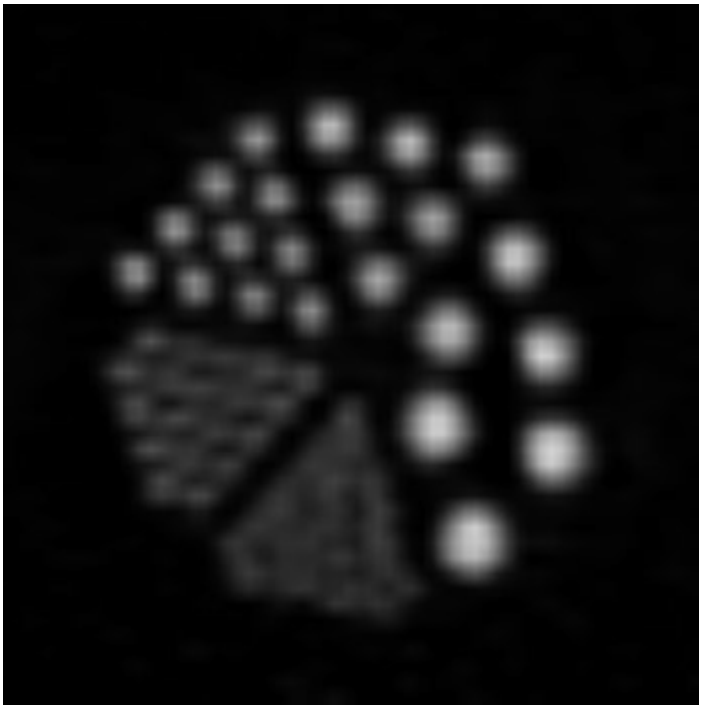

Figure A.3: A coronal maximum intensity projection image of the Derenzo phantom filled with ^{18}F. The smallest resolvable holes are the 1.6 mm holes (8 o'clock).

The total spatial resolution of *Sarah* is based on several factors including individual detector size, positron range, the acolinearity effect, decoding (when there are more scintillation crystals than photodetectors), the penetration of the 511 keV photons between interaction in the crystals, and sampling error[51]. These effects all add in quadrature with the exception of the sampling error which acts as a multiplicative factor that degrades all the other components. In terms of investigating different positron-emitters, the only variable that changes when swapping the positron emitter is the positron range term. The formula for the total spatial resolution with all components except the positron range is aggregated into a single term, is given by:

$$\Gamma = 1.25\sqrt{s^2 + \Delta} \tag{A.1}$$

where the factor of 1.25 is the multiplicative factor from the sampling error, s is the positron range, and Δ is the aggregation of the other components. This allows for an estimation of the total system resolution for any positron emitter if the component for the positron range is known. The positron ranges for the positron emitters discussed in this dissertation are shown in Table A.1 in units of mm FWHM where these values were linearly interpolated from Table 1 in Moses[51]. Figure A.4 shows a plot of the total system resolution for *Sarah* versus the mean positron energy.

Table A.1: Mean positron energy and positron range for positron emitters discussed in this dissertation.

Isotope	Mean Positron Energy (keV)	Positron Range (mm FWHM)
^{18}F[a]	250	0.54
^{11}C[a]	386	0.92
^{89}Zr	396	0.98
^{133}La	460	1.32
^{13}N[a]	492	1.49
^{44}Sc	632	2.06
^{86}Y	660	2.17
^{149}Tb	730	2.46
^{15}O[a]	735	2.48
^{68}Ga[a]	830	2.83
^{152}Tb	1140	4.41
^{134}La	1217	4.80
^{132}La	1290	5.17
^{82}Rb[a]	1481	6.14

[a]The positron ranges for these isotopes were taken from Moses[51].

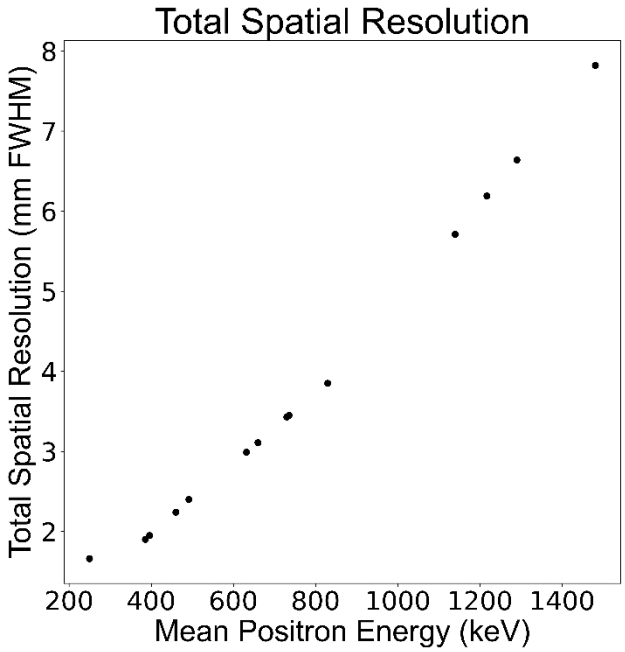

Figure A.4: Total spatial resolution versus mean positron energy for *Sarah.*

APPENDIX B: Radiochemical Yield and Radiochemical Purity

Two metrics that pertain to radiolabeling molecules that are discussed frequently in this dissertation are radiochemical yield and radiochemical purity. The definitions and distinctions are discussed here.

Radiochemical yield is the proportion of activity in the product after going through a process where activity may have been loss[168]. As an example, in this dissertation radiochemical yield is often talked about in reference to purifying antibody drug conjugates using 0.5 mL 30 kDa Amicon Ultra centrifugal filter units. The activity in the product is the activity that stays in the filter (or the retentate) and the activity that is lost is the activity that goes through the filter (or the filtrate).

Radiochemical purity is the proportion of activity in the sample that is in the desired radiolabeled species[169]. As an example, if discussing a radiolabeled antibody, this is the proportion of activity that is labeled to the antibody. This value can be measured by radio-Instant Thin Layer Chromatography. For the conditions used in this dissertation, an activity that is labeled to the antibody stays at the origin while free radioactivity follows the solvent front. An example of a TLC trace of ^{212}Pb-TCMC-Trastuzumab is shown in Figure B.1.

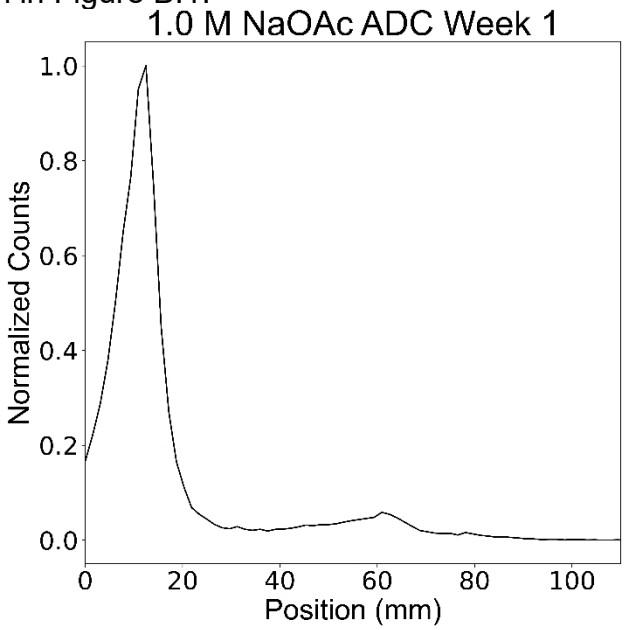

Figure B.1: TLC trace of ^{212}Pb-TCMC-Trastuzumab. Activity that is labeled to the antibody stays at the origin while free activity follows the solvent front.

While for antibody labeling the radiochemical purity is distinct from the radiochemical yield, for small molecule studies (such as the metal-chelator complexes) the distinction between the two metrics overlaps. For complexes, by definition the radiochemical purity is the proportion of activity actually labeled to the molecule (as measured by TLC in this dissertation). However, in previous studies this metric (measured by radio-ITLC) has been reported as the radiochemical yield[63]. In order to keep the notation consistent with the literature, complex measurements done by radio-ITLC will be reported as radiochemical yield. An example of a TLC trace of ^{134}Ce-DOTA is shown in Figure B.2.

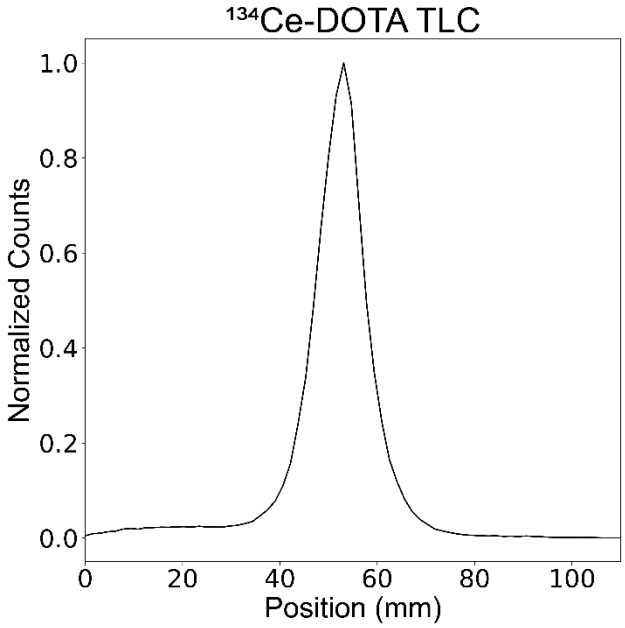

Figure B.2: TLC trace of ^{134}Ce-DOTA. Activity that is labeled to the chelator is located at the prominent gaussian peak while free activity lies outside the prominent gaussian peak.